# Nonperiodic silicon photonic devices for nonlinear photon generation and multimode design for optical computing

*Zhetao Jia*

Electrical Engineering and Computer Sciences
University of California, Berkeley

Technical Report No. UCB/EECS-2024-200
http://www2.eecs.berkeley.edu/Pubs/TechRpts/2024/EECS-2024-200.html

December 1, 2024

# Nonperiodic silicon photonic devices for nonlinear photon generation and multimode design for optical computing

by

Zhetao Jia

A dissertation submitted in partial satisfaction of the

requirements for the degree of

Doctor of Philosophy

in

Engineering — Electrical Engineering and Computer Sciences

in the

Graduate Division

of the

University of California, Berkeley

Committee in charge:

Professor Boubacar Kanté, Chair
Professor Joel Moore
Professor Ming-Chiang Wu

Fall 2023

Nonperiodic silicon photonic devices for nonlinear photon generation and multimode design for optical computing

Abstract

Nonperiodic silicon photonic devices for nonlinear photon generation and multimode design for optical computing

by

Zhetao Jia

Doctor of Philosophy in Engineering — Electrical Engineering and Computer Sciences

University of California, Berkeley

Professor Boubacar Kanté, Chair

Integrated photonics has experienced significant growth in both academic research and industry startups. Chip-scale photonic devices are transforming key areas including communication, computing, sensing, navigation, and augmented/virtual reality (AR/VR). However, challenges in current platforms hinder the practical application of these technologies. Specifically, weak materials nonlinearities have limited direct on-chip photon generation for both classical and quantum light sources, and also existing photonic devices' bandwidth for communication/computing is not meeting current demands.

The goal of this thesis is to provide possible solutions to the two issues in silicon photonics. First, I will discuss using topological structures to enhance the transport and nonlinear frequency generation in silicon photonics. We propose a non-periodic photonic system with a structural disorder that confines light near the system boundary, enhancing the nonlinear photon generation rate compared to periodic systems. Next, I will introduce a systematic inverse-design method, aiming to boost the efficiency of on-chip nonlinear photon generation, along with a physical interpretation of these results. Specifically, I will present our experimental demonstration of a compact, robust, and efficient entangled photon pair source based on spontaneous four-wave mixing, achieving a generation rate of 1.1MHz and a coincidence to accidental ratio of 162. This method can also be generalized for other nonlinear optical processes. In the second part of the thesis, I will show the possibility of expanding the optical computing bandwidth with a mode-division multiplexing (MDM) strategy, offering a new degree of freedom in optical computing with the micro-ring resonator platform. I will outline an MDM strategy suitable for small-scale neural networks and a multi-dimensional architectural approach for large-scale optical computing applications. I will present the experimental results of our device for matrix multiplication fabricated at foundry.

To my parents and my fiancée

# Contents

# List of Figures

# Acknowledgments

The past five years of my doctoral study have been an amazing journey of growth. I have had the fortune to meet and work with amazing people, attend talks and conferences about world-leading technologies and ideas, have the opportunities to think deeply and consistently about photonics and reflect on my career and personal goals.

First, I would like to thank my advisor, Prof. Boubacar Kanté, for the chance to explore optics and photonics, with my previous background in acoustics before joining the group. His broad research interests, commitment to excellence and innovation, and direct way of communication profoundly influenced my PhD work. I am particularly thankful for his support in my venture into silicon photonics, a new direction for our group. He provided his best support and always pushed the limit of our work, which turned out to be fruitful. I owe a debt of gratitude to Prof. Eli Yablonovitch for his insightful guidance and visionary views. His intuitive approach to research taught me to look critically at concepts and terminologies that are presented with over-complexity. Our weekly joint group meetings that explored the history of semiconductors, optics, and beyond had been immensely educational and transformative. I would like to acknowledge Prof. Joel Moore for his valuable advice through our collaboration and Prof. Ming Wu for his excellent lectures and kind support with lab equipment. My appreciation also goes to Prof. Stefan Preble, of Rochester Institute of Technology, for introducing me to foundry-level fabrication and testing, which significantly broadened my understanding of silicon photonics.

I am also grateful for my friends and colleagues, who have made my PhD journey not only educational but also enjoyable and memorable. I am very fortunate to start and finish my PhD alongside Rushin and Mutasem. Rushin is extremely patient and approaches life with grace and composure. I could always count on him when I needed someone to bounce ideas off of, and he always shared his knowledge with such clarity. Mutasem was the one who introduced me to silicon photonics and had been a constant companion during the time we spent in the cleanroom and discussed physics concepts. His perspectives greatly broadened my views on academia and industry and had always been inspiring.

I'm deeply thankful to Matteo and Jagang for their patient mentorship. Matteo's elegant writing style and serious attitude toward the fundamentals significantly improved my own research and writing skills. His support during challenging times was indispensable. Jagang's keen understanding of our subject matter and deep insights into physics have been a source of constant learning for me. I want to thank my collaborator Wayesh for his patience in the discussion and consistent support in fabrication.

I would also like to thank Junhee, Wanwoo, and Whimin for their guidance during the early years of my PhD. Their advice on how to lead a meaningful doctoral career is invaluable. In addition, Keke's curiosity and profound grasp of the fundamental concepts had been inspiring, and our lunchtime discussions had always been both enjoyable and enlightening. A special thanks go to Sean Hooten for training me in inverse design and providing valuable project advice. I would like to thank Alex and Elizabeth for their teachings in topology. I am also grateful to Hector and Lilian for showing me how to use experimental setups effectively.

To the rest of my colleagues–Walid, Liyi, Kevin, Zhanni, Yertay, Emma, Lanyi, and Difan, working alongside with you had made daily life in the office much more pleasant. Your camaraderie and collaboration have been a constant source of joy and learning.

My PhD career would not be this happy without the support from my fiancée Meilin. Your patience and joy made the past five years shine in my life, saving me from being jaded by the day-to-day office work routine. I can't wait to start the next journey with you with our wedding next year.

Last but most importantly, I would like to thank my parents for their unconditional support and love. You show me how to be a nice person. And you encouraged me and allowed me to have the opportunity to study the subject that I have a passion for.

# Chapter 1

# Introduction

## 1.1 Motivation

The reduction in the size of integrated circuits has significantly advanced everyday electronic devices. Over the past five decades, Moore's law has been a general guidance to scale down the transistors, driving innovations to double the number of transistors every two years. Beyond size reduction, smaller devices achieve higher operating frequencies and lower power consumption per operation, as per "Dennard Scaling". The downsizing makes the integration of more complicated systems possible, which enables more functionalities. In the meantime, the smaller footprint of each component also reduces the cost of the device, thanks to batch fabrication techniques. Driven by all the benefits, the semiconductor foundry has overcome various challenges to make smaller and smaller transistors.

The idea of building integrated photonics with the existing platform of integrated circuits greatly speeds up the development of the on-chip system with light. The benefits of scaling can hopefully also be applied to optical devices, without an additional fifty years' effort and billions of dollars to improve the fabrication workflow. Since the concept of integrated photonics was proposed, there has been a lot of effort spent both in academia and industry towards the goal of making useful integrated photonics devices. Despite many applications of integrated photonics are still in the early stage, it has great potential to revolutionize the existing platforms or products (Fig. 1.1). The optical transceiver, for example, has been widely used in data communication platforms to improve the communication bandwidth. There has also been many companies and startups actively working on Light Detecting and Ranging (LiDAR) system and optical gyroscope for navigation purposes. The integrated photonics navigation devices can be a critical component for autonomous driving vehicles. The integrated photonics technologies can also be used for health monitoring by, for example, measuring the reflection spectrum. In addition, motivated by the large energy consumption in machine learning related computation, researchers envision that the integrated photonics technologies can improve the performance of existing computing platforms, in classical or quantum computing regimes. More applications of compact integrated photonic devices

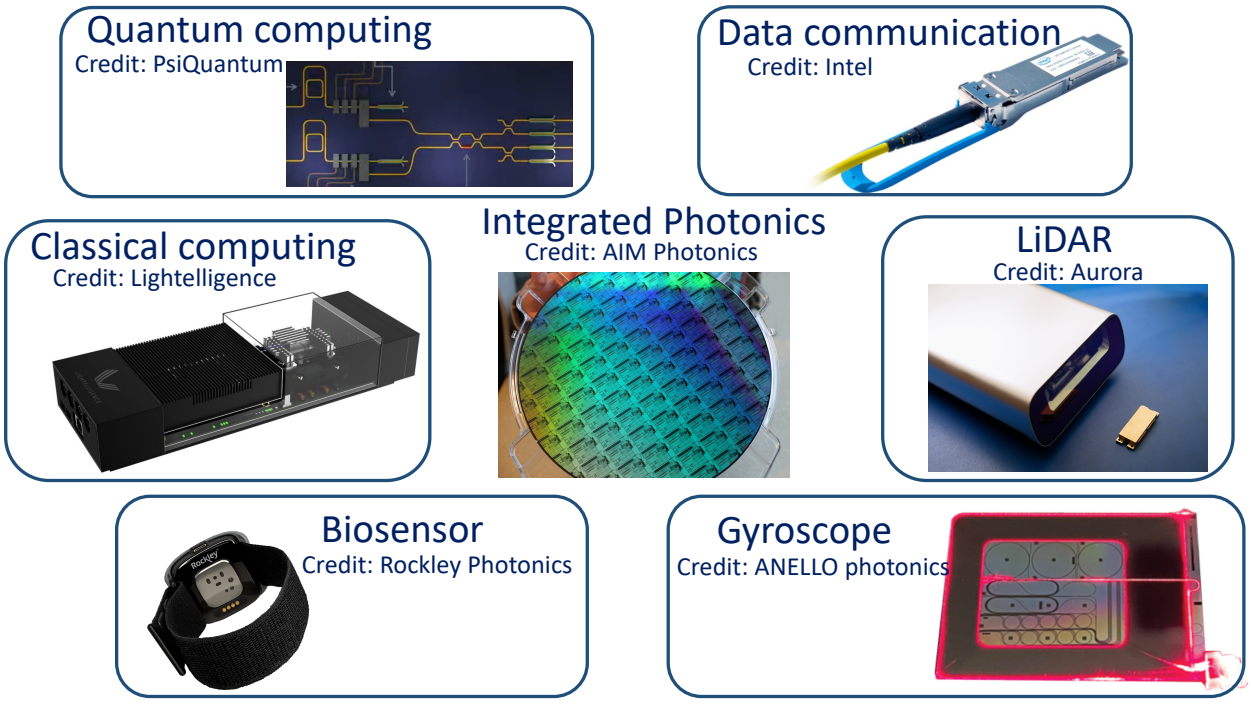


Figure 1.1: **Existing and emerging applications of silicon photonics.**

across diverse fields remain a dynamic research area with promising potential.

## 1.2 Constraints of silicon photonics technologies

### Micro-ring resonator

A useful component in the integrated photonics platform is micro-ring resonators[1], which is a closed loop (e.g. circle or racetrack shape) formed by the waveguide. The simple geometry leads to convenient implementation in fabrication. With the coupling waveguide, the micro-ring structure can be used as a filter as shown in Fig. 1.2. In Fig. 1.2(a), a micro-ring resonator is coupled to a single bus waveguide, which is connected to two grating couplers for coupling the light between free space and the chip. The transmission spectrum is measured and normalized, shown in Fig. 1.2(b). At resonance wavelengths, the incident photons are extracted to the micro-ring resonator and absorbed. Therefore, this configuration makes a simple and efficient filtering device. With thermal tuning or plasma dispersion effect, the resonance frequencies can be tuned and the intensity at the output port can be modulated. In practice, the micro-ring can also be applied in increasing the bandwidth of data communication. By using micro-ring resonators of slightly different sizes along with

active tuning mechanisms, the light modulated at different frequencies can be transmitted through the same waveguide, hence increasing the communication bandwidth. This method for increasing the bandwidth is called "Wavelength-Division Multiplexing"(WDM).

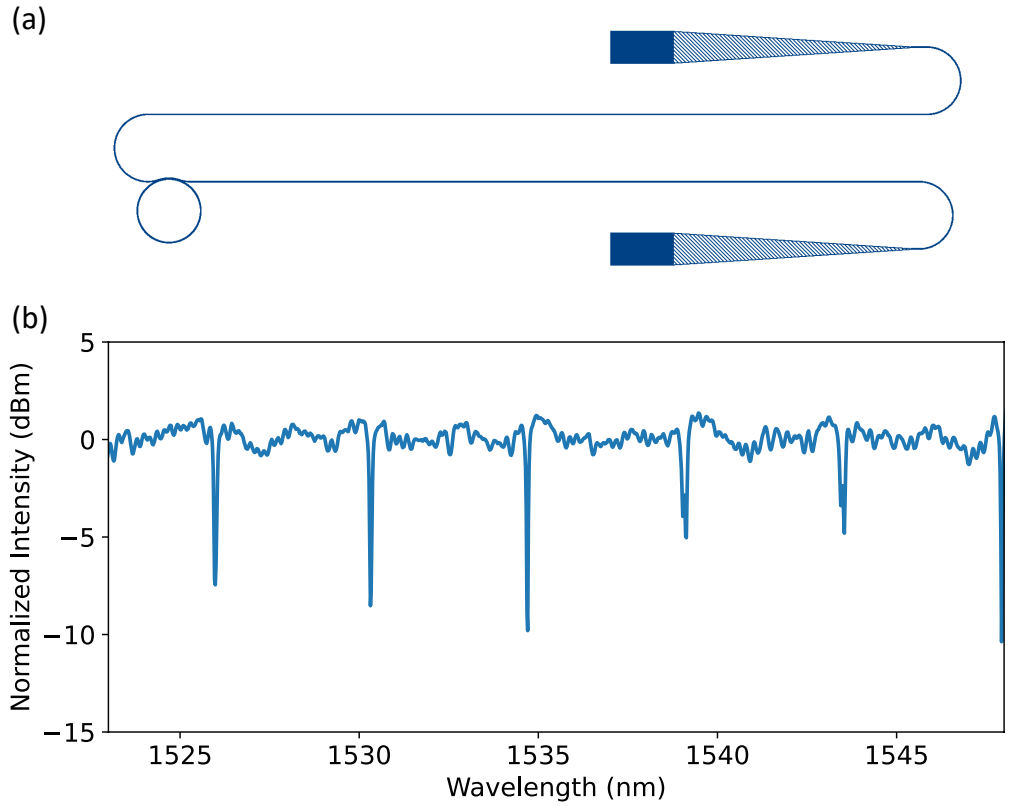


Figure 1.2: **Transmission spectrum of a single micro-ring resonator.** (a) Layout of the device. Two grating couplers are used for input (output). (b) Measured transmission spectrum of the micro-ring resonator.

In addition, the micro-ring resonator is a good candidate for nonlinear processes, especially four-wave mixing. In Fig. 1.3, the inset shows the energy diagram for a four-wave mixing process. In the degenerated stimulated four-wave mixing process, two pump photons and a signal photon produce an idler photon, where the energy is conserved. In the micro-ring structure, the pump, signal and idler frequencies can be chosen at the resonances. In this way, the resonances enhance the intensity of the inputs, which increases the generation efficiency of idler photons. In Fig. 1.3, the output spectrum is measured with two continuous-wave lasers as inputs at pump and signal frequencies. As shown in the spectrum, the idler photons are generated due to the nonlinearity.

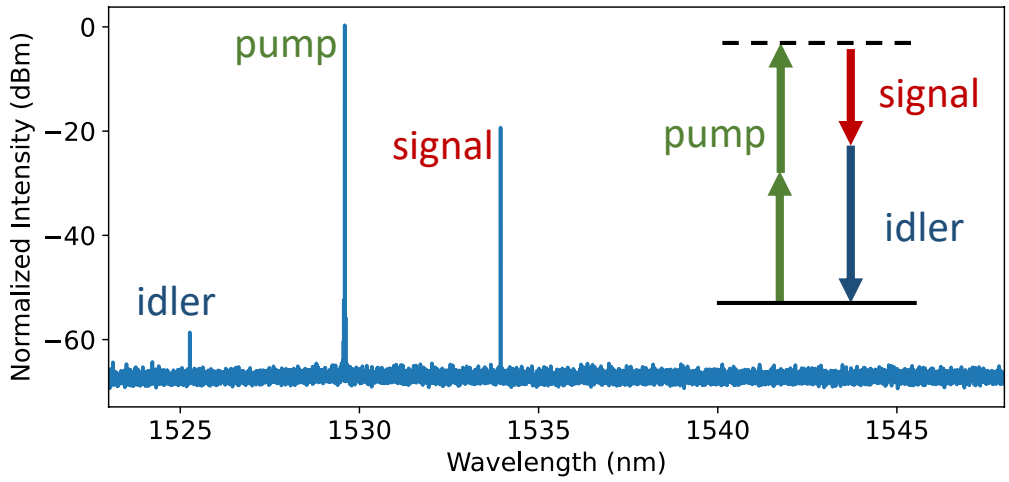


Figure 1.3: **Stimulated four-wave mixing in a micro-ring resonator.** The measured output spectrum illustrates the generation of the idler photons. Inset: schematic of energy diagram for the four-wave mixing process.

## Constraints of micro-ring resonator

While micro-ring resonators are useful, their applications face limitations due to constraints in fabrication variation, device footprint, nonlinear conversion efficiency, and modulation bandwidth.

**Fabrication:** For commonly used micro-ring resonators, the light is confined inside the waveguide, which leads to its sensitivity to fabrication. An example is shown in Fig. 1.4, where nine identical micro-rings are coupled to the same bus waveguide. Ideally, nine micro-ring resonators should have the same resonant frequencies, therefore deep, isolated dips are expected in the spectrum. In practice, however, due to fabrication imperfection, multiple dips are shown, corresponding to different micro-rings, and active tuning methods have to be used for calibration.

**Footprint:** The footprint of micro-ring resonator is limited by the scattering loss. As the bending radius goes below $5um$ in a silicon micro-ring, the scattering loss increases significantly, preventing the total footprint from going below $100\mu m^2$.

**Nonlinear efficiency:** The nonlinear efficiency is low and is sensitive to the thermal effect in practice. As an example, in Fig. 1.3, the conversion ratio from signal frequency to idler frequency is less than -30dB, which needs to be improved.

**Bandwidth:** The multiple resonances in the micro-ring resonator prevent the use of the full spectrum in WDM. The resonances of multiple ring resonators need to fit within a free spectral range to avoid crosstalk. Ideally, each device should modulate a single wavelength, and the entire spectrum can be utilized. With the increase in the need for communication bandwidth, new approaches are needed to enable a larger bandwidth in WDM-related

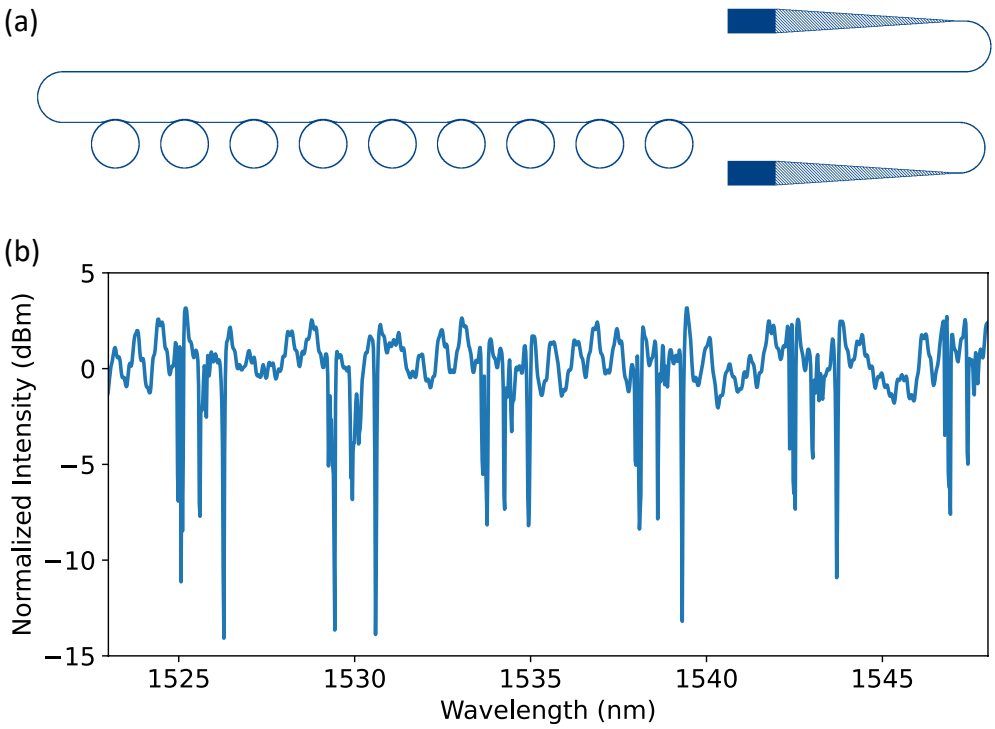


Figure 1.4: **Transmission spectrum of nine identical micro-ring resonators coupled to the same bus waveguide.** (a) Layout of the device. (b) The measured transmission spectrum shows the fabrication variation of the micro-rings.

applications.

## 1.3 Periodic and nonperiodic structures

In this thesis, I will first discuss the possible approaches to enhance nonlinearity with nonperiodic structures. The first question to ask is what is the difference between periodic and nonperiodic systems, in terms of bandgap and mode distribution? Here, we draw ideas from nonperiodic materials and introduce different types of disorders for nonperiodic photonic systems.

### Periodic and amorphous materials

Electronic bandgap exists in crystalline materials due to the energy difference between the valence band and the conduction band. In amorphous silicon, despite its nonperiodic structure, it has been observed that a bandgap also exists (1.5(a)). Historically, there had been a lot

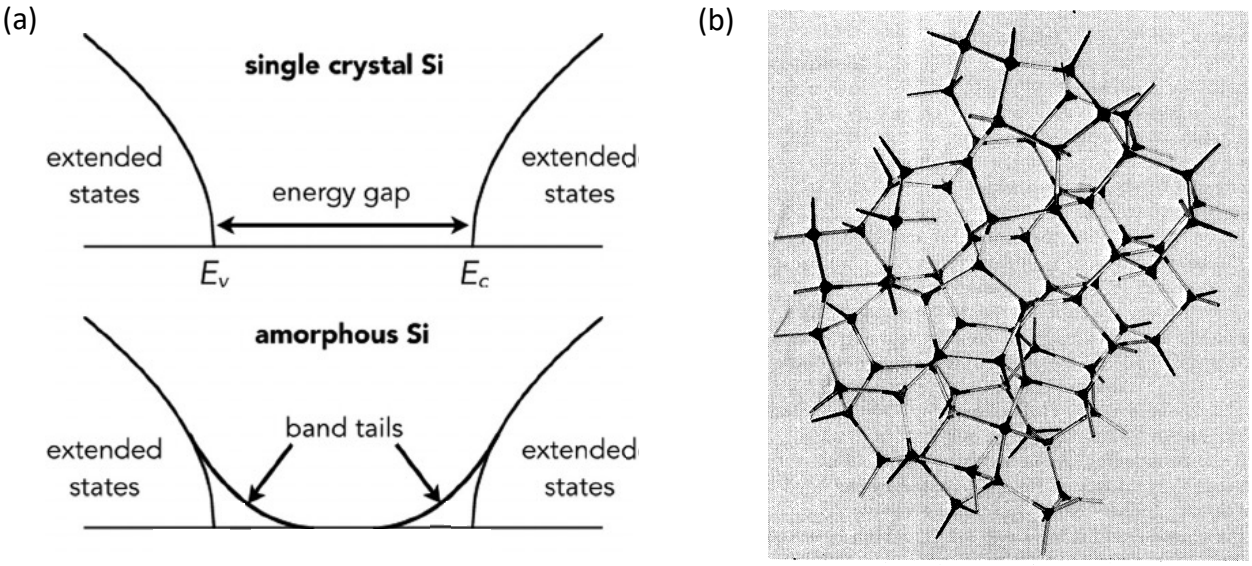


Figure 1.5: **Bandgap in both crystalline and amorphous silicon.** (a) Energy gap in both single crystal and amorphous silicon (germanium) [2]. (b) A schematic figure for the structure of amorphous silicon with a fixed coordination number [3].

of research interest in understanding the phenomena, which was then successfully explained by Weaire and Thrope in the 1970s. The amorphous structure in silicon or germanium has a fixed coordination number, i.e., each atom shares the same number of bonds (four in this case) with its neighbors as illustrated in Fig. 1.5. In Ref. [3], Weaire and Thrope adopt a tight-binding model to show that bandgap exists. Their findings not only shed light on the properties of amorphous silicon but also provided insights into, for example, the transparency of glass, which is composed of amorphous silicon dioxide.

## Types of Disorder

The way that amorphous silicon/germanium breaks the periodicity can be identified as a special type of disorder called structural disorder. Structure disorder maintains a fixed coordination number while breaking the periodicity, which can be easier to visualize in the 2D case. The structural disorder is different from other types of disorder, for example, potential disorder, where each atom/resonator in the system can be slightly different from one another; or positional disorder, where the position(s) of one or more atoms are shifted, introducing additional coupling beyond the original nearest neighbors. We will use structural disorder and potential disorder in the following sections to enhance the nonlinearity.

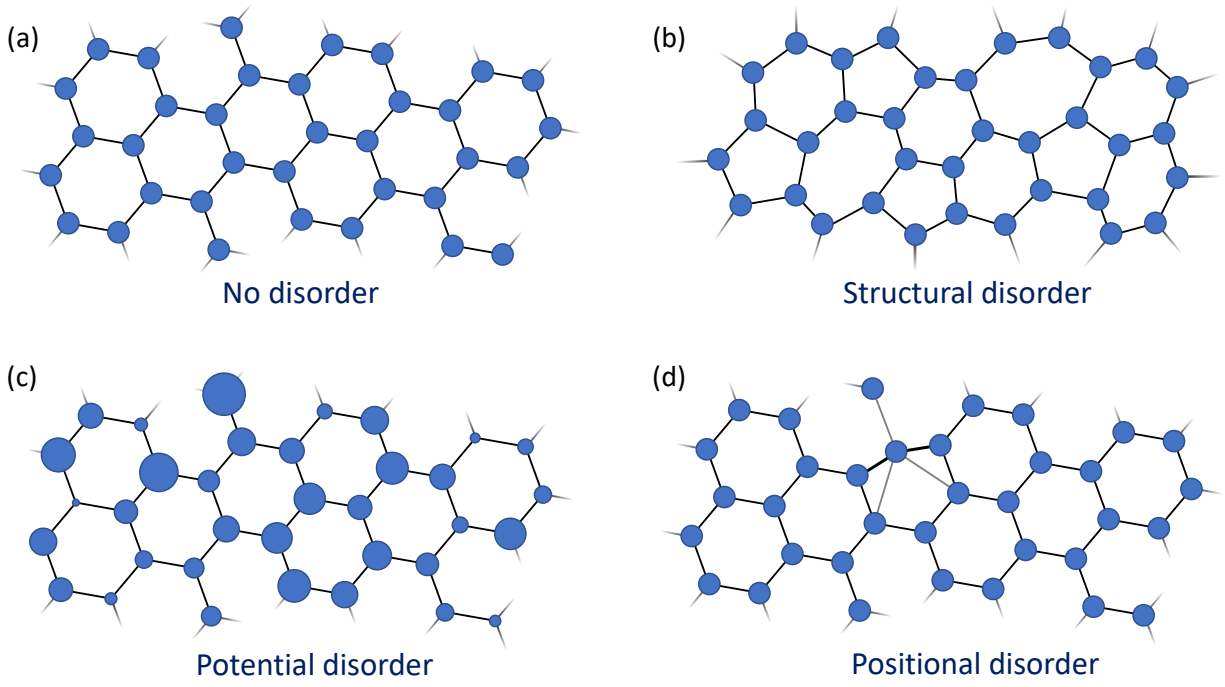


Figure 1.6: **Different types of disorder.**

## 1.4 Outline of the thesis

This thesis targets performance enhancements in the current silicon photonics platform, focusing on nonlinear photon generation and optical bandwidth for computing. In Chap. 2, I will first introduce the basics of topological insulators and topological photonics. I will discuss the use of topological structures to enhance transport based on arrays of micro-ring resonators and propose a novel nonperiodic photonic topological system with structural disorder to confine light effectively near the system boundary. The platform maintains edge propagation even in the presence of Kerr nonlinearity, which enhances the nonlinear photon generation rate compared to conventional periodic systems. In Chap. 3, I will discuss the generalized phase matching conditions for nonlinear light generation in a non-conventional cavity. I will then introduce a systematic inverse-design method for nonlinear optical systems. I will present our experimental demonstration of a compact, robust, and efficient entangled photon pair source and provide a physical interpretation based on potential disorder for the inverse-designed device. In Chap. 4, I will introduce the idea of optical neural networks and I will show the concept of mode-division multiplexing that can be combined with wavelength-division multiplexing. As a demonstration, I will show the experimental results of components and the system for mode-division multiplexing in combination with wavelength-division multiplexing. In Chap. 5, I will conclude the thesis and propose poten-

tial future directions.

# Chapter 2

# Enhancing nonlinearity with structural disorder: amorphous topological systems

## 2.1 Introduction

Disorder in two-dimensional electronic systems leads to a wide range of topological phenomena, including integer and fractional quantum Hall effects, in which impurities resulting from the sample fabrication process break the degeneracies of Landau levels and localize the wavefunctions at almost all energies [4, 5, 6, 7]. Such localization is the direct cause of quantized plateaus in the Hall conductance, as the localized states do not contribute to the particle transport and the quantization plateaus would cease to exist in an ideal clean sample [4, 8, 9].

The hallmark of topological phenomena in two-dimensional finite-size systems is the appearance of a transport channel that is robust to disorder [10]. The robustness to disorder has been investigated and exploited in many wave-based phenomena including photonics, microwaves, acoustic, and plasmonics, to conceive devices potentially more robust to manufacturing imperfections that usually degrade the performance of classical systems and cause decoherence in quantum systems [6]. Topological transport, occurring along boundaries, can be unidirectional and immune to back-scattering, provided that the disorder is not strong enough to close the mobility gap. The unique robustness of topological transport has led to advanced device concepts, including topological delay lines, topological lasers, topological frequency combs, and topological quantum light sources [11, 12, 13, 14, 15, 16, 17, 18, 19]. However, most attention has focused on the treatment of *potential disorder*, i.e., on spatially local random potentials. A different type of disorder, known as *structural disorder*, has long existed in nature, for example in amorphous silicon. In this non-crystalline form of silicon, the local connectivity is preserved, since each silicon atom is bonded to four adjacent neighbors, but long-range structural order is lost. Nevertheless, a mobility gap in amorphous

matter has been observed [3, 20]. More recently, topological phenomena have been observed in non-periodic systems [21, 22, 23, 24, 25, 26]. These findings lead to a natural question to ask: beyond preserving topological properties, can disordered topological systems outperform their periodic counterpart? We propose a structurally disordered system that exhibits a nontrivial topological phase, characterized by a non-uniform synthetic magnetic flux. We show that, in the presence of nonlinearities, the structurally disordered system prevents the ultrafast leakage of energy from topological modes to bulk modes, enhancing nonlinear phenomena. As an example, we demonstrate that the longer confinement of light can lead to an order of magnitude increase in the generation rate of correlated photon pairs compared to periodic topological platforms.

## 2.2 Theory

### Basic idea of topological insulator

The Quantum Hall effect, a pivotal discovery in condensed matter physics, demonstrates quantized conductance in "dirty" samples. Despite the impurities creating potential disorder in the sample, the possible values of conductance are still proportional to integer values and remain the same even when the external magnetic field is perturbed. Such robustness is also highly desired in practical applications, which can lead to efficient transport of electrons or photons along the boundary of the system. The robustness can be quantified by the topological index. A simple example is that for a closed system, we can define the topological index as the number of eigenmodes below a certain energy threshold. The topological index remains invariant provided perturbations do not lead to eigenmode transitions across the critical energy threshold. The advantage of defining the topological index is that such an index can be used to label different systems so that systems with different labels cannot be adiabatically changed from one to another without topological transition. A key concept is bulk-edge correspondence, which predicts edge modes at the boundary between systems with different topological indices.

The topological insulators can be classified based on the dimension and symmetry of the system [27]. Here, we focus on the 2D case where time-reversal symmetry, particle-hole symmetry, and chiral symmetry are all broken. Next, we briefly describe how the topological index can be calculated. The discussion begins with the Berry phase concept, the geometric phase acquired by an eigenstate following an adiabatic path around a closed loop in parameter space. The Berry phase $\gamma$ can be represented as the line integral of Berry connection $\mathbf{A}(\mathbf{R})$ as

$$\gamma = \oint_C \mathbf{A}(\mathbf{R}) \cdot d\mathbf{R} \tag{2.1}$$

where $\mathbf{R}$ is the parameters. The Berry connection serves as a local gauge of eigenstate variation. The Berry curvature and Berry connection are related by Stokes' theorem:

$$\oint_C \mathbf{A} \cdot d\mathbf{r} = \int_S \mathbf{\Omega} \cdot d\mathbf{S}, \mathbf{\Omega} = \nabla \times \mathbf{A} \tag{2.2}$$

The Chern number is derived from integrating the Berry curvature over the entire Brillouin zone.

$$C = \frac{1}{2\pi} \int_{\mathrm{BZ}} \mathbf{\Omega}(\mathbf{k}) \cdot d\mathbf{S} \tag{2.3}$$

Or equivalently, the parameter is the momentum, therefore

$$C = \frac{1}{2\pi} \int_{\mathrm{BZ}} d^2k \, \mathbf{\Omega}(\mathbf{k}) \tag{2.4}$$

## Chern number calculation in the periodic system

A tight-binding model illustrating non-trivial topological features is examined in a kagome lattice. In Fig. 2.1, a finite-size periodic kagome lattice is shown. Its unit cell is highlighted within the red hexagon, with arrows indicating a directional hopping phase $e^{-i\phi}$. The system's Hamiltonian, representative of the kagome lattice, is expressed as

$$\hat{H}_0 = \sum_i \omega_0 \hat{a}_i^\dagger \hat{a}_i - \kappa \sum_{\langle i,j \rangle} \left( e^{-i\phi} \hat{a}_i^\dagger \hat{a}_j + e^{i\phi} \hat{a}_j^\dagger \hat{a}_i \right), \tag{2.5}$$

where $\hat{a}_i^\dagger$ ($\hat{a}_i$) creates (annihilates) a particle on the $i$-th site, $\omega_0$ is the natural on-site frequency, and $\langle i, j \rangle$ restricts the summation to pairs of nearest-neighbors. In the periodic system, the hopping phase $\phi$ determines the band structure and opens a topological gap when the hopping phase is tuned from $\phi = 0$ to $\phi = \pi/2$. The nontrivial topological properties can be illustrated by the Chern number and the calculated topological indices of three bands are labeled in Fig. 2.1(c), with $-1, 0, 1$ from lower to higher bands, respectively.

## Generation of the topological graph with structural disorder

To generate a topological graph with structural disorder, a method involving tessellation and local triangularization of randomly sampled two-dimensional points is employed [25]. The initial random points can be generated, for example, with disk sampling (Fig. 2.2(a)) in a domain with area $L^2$ and periodic boundary conditions. The filling ratio $\eta$, defined as the ratio of area covered by disks over the area of the sampling domain, is the parameter used to control the strength of structural disorder. The Voronoi diagram is used to partition space and create a graph with a fixed coordination number $N = 3$ (Fig. 2.2(b)). The amorphous graph is created by a kagomization process, in which the centers of the edges sharing the same vertices are connected. The resulting graph has a local coordination number ($N = 4$) in Fig. 2.2(c). Because of the coordination number $N = 3$ for the Voronoi diagram, the generated amorphous graph consists of local triangles around the vertices of the Voronoi

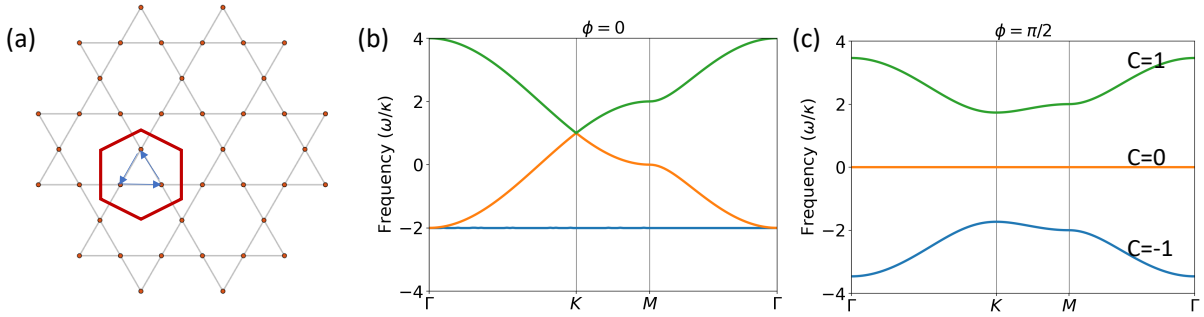


Figure 2.1: **Topological kagome lattice.** (a) Structure of a finite-size kagome lattice with a directional hopping phase. The unit-cell, containing three sites, is highlighted by the red hexagon. (b) Band diagram of a kagome lattice with a null directional hopping phase ($\phi = 0$), where the coupling between sites is real. (c) Band diagram of a topological kagome lattice with $\phi = \pi/2$, which corresponds to a complex hopping $e^{-i\phi} = -i$. Topological bands with nonzero Chern numbers appear.

diagram, but the tessellated regions consist of polygons with different numbers of sides. The periodic lattice in Fig. 2.1(a) can also be generated by the same procedure, with the difference that, instead of starting from a random point set, we use a triangular lattice. The triangular lattice arrangement, indeed, is the most compact configuration achievable via disk sampling, characterized by a maximum filling ratio $\eta_{max} = 0.9069$. The amorphous graphs are generated with a fixed filling ratio $\eta = 0.45$ for the disk sampling process.

## Chern number calculation in the amorphous system

The topology of the amorphous graph is probed by the Kitaev sum, a topological index defined as [28, 25]

$$\nu(P) = 12\pi \sum_{i\in A}\sum_{j\in B}\sum_{k\in C}\left(P_{ij}P_{jk}P_{ki} - P_{ik}P_{kj}P_{ji}\right), \tag{2.6}$$

where $P$ is the projection operator onto the eigenmodes below the cut-off energy, $A$, $B$, $C$ are three spatial regions shown in Fig. 2.3 and $i$, $j$, $k$ are sites within corresponding regions.

The summation region is fixed to span half of the side length of the lattice, as shown by the square in Fig. 2.3, and it is divided into three regions $A, B$, and $C$ represented by different colors. To study the phase transition under different hopping phases $e^{-i\phi}$, the cut-off frequency is swept, and the topological index is averaged over 20 random realizations of the amorphous graph. As an example, the standard deviation of the Kitaev sum with phase $\phi = \pi/2$ is shown in Fig. 2.3(b), revealing that the Kitaev sum remains $-1$ within the

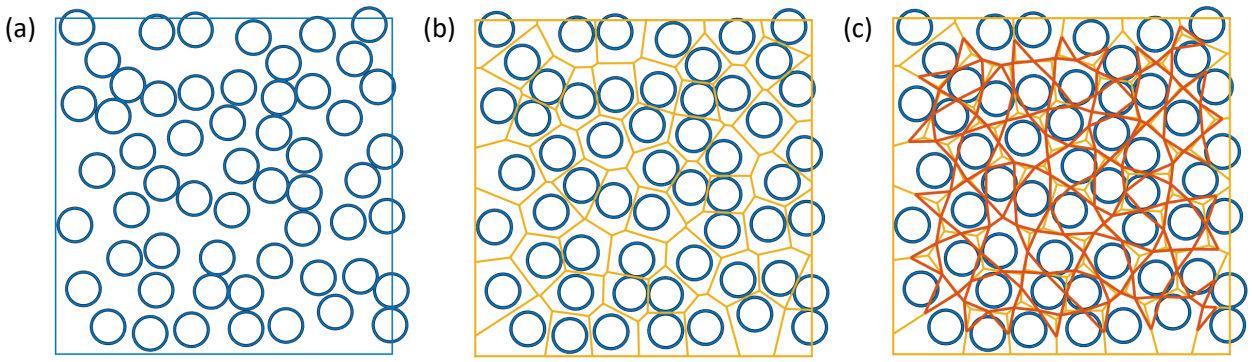


Figure 2.2: **Amorphous graph generation procedure.** (a) Disks are randomly sampled within the domain with periodic boundary conditions. Each disk has a fixed radius and does not overlap with its neighbors. (b) Voronoi diagram is generated based on the disk centers. (c) The centers of edges sharing to the same vertices are connected to generate a kagome-like graph.

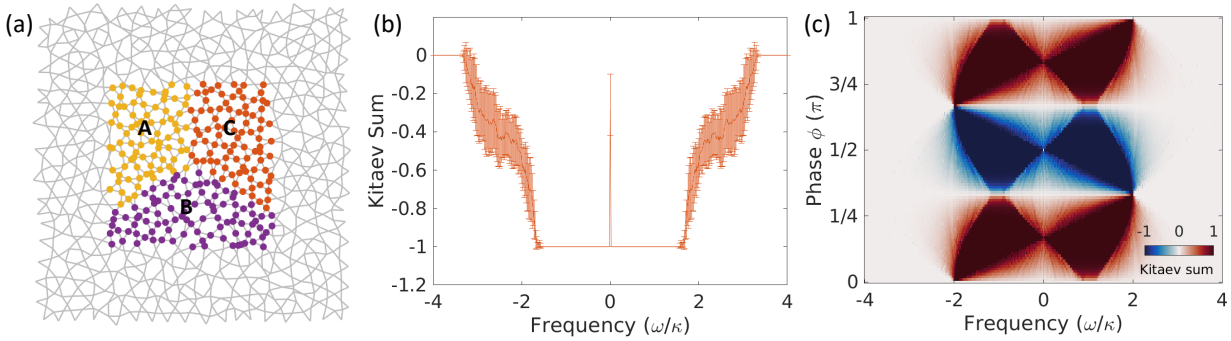


Figure 2.3: **Kitaev sum calculation.** (a) Calculation of the Kitaev sum in the amorphous structure. To calculate the local topological index, the integration region is subdivided into three sections, marked here with different colors. (b) Kitaev sum averaged over 20 random realizations of a graph with a hopping phase $\phi = \pi/2$. (c) Kitaev sum calculated on a finite-size periodic lattice.

topological bandgap with negligible variance across realizations of structural disorder. As a comparison, the Kitaev sum of a similar periodic system is show in Fig. 2.3(c). The periodic phase diagram has sharp boundaries due to lack of the localized bulk modes near the band edges. The bandgap closes for phase values of $\phi = 0, 1/3\pi, 2/3\pi$ and $\pi$, in agreement with Fig. 2.1(b).

## 2.3 Simulation results

### Periodic and amorphous system in linear regime

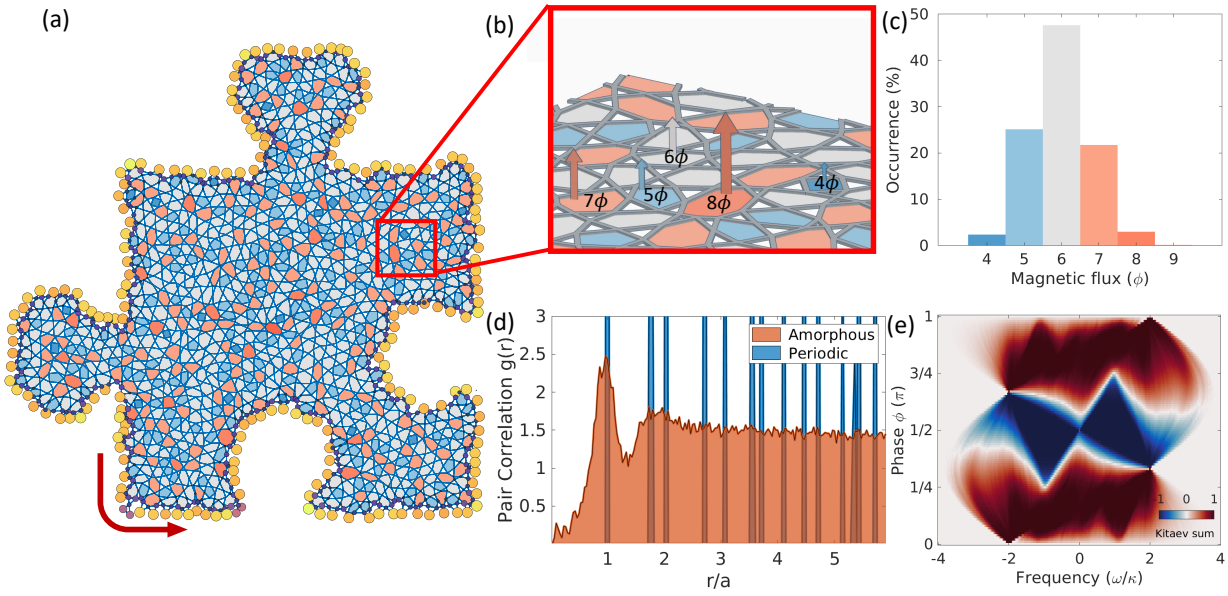


Figure 2.4: **Principle and design of amorphous topological graphs.** (a) Sketch of an amorphous topological graph. The local coordination number $z$ is preserved ($z = 4$), while the graph connectivity is different from the periodic counterpart. Different colors indicate polygonal plaquettes with different number of sides. (b) Zoomed-in view of (a), showing the presence of a non-uniform magnetic field flux. The labels quantify the magnetic flux across each polygonal plaquette, which is equal to the overall hopping phase acquired by a photon through a round-trip around the plaquette. (c) Distribution of polygonal plaquettes with $N \geq 4$ sides for the graph in (a). The periodic lattices only have hexagons with $N = 6$. (d) Pair correlation function $g(r)$ of the amorphous structure in (a), compared to the periodic lattice. The amorphous structure lacks long-range order, as evidenced by the flattened pair correlation function at longer distances $r/a$. (e) Topological phase diagram for the amorphous structure. The color represents the Kitaev sum calculated over all the modes below different values of the cutoff frequency $\omega/\kappa$, for different hopping phases $\phi$ between adjacent vertices. The result is averaged over 20 realizations of disorder.

The proposed nonlinear amorphous graph, presented in Fig. 2.4, is constructed by kagomizing a Voronoi diagram obtained from a disk-sampled set of points as described in the previous section [25]. The result is a collage of polygonal plaquettes, each possessing three to nine sides, as sketched in Fig. 2.4(a). Adjacent vertices are then coupled by a directional hopping

with uniform magnitude $\kappa$ and phase factor $e^{i\phi}$, shown as the graph edges in the sketch in Fig. 2.4(a). The linear tight-binding Hamiltonian can be written in the same form as Equation (2.5). The additional hopping phase $\phi$, which can be tuned in a silicon photonics implementation, can be interpreted as the Peierls phase resulting from the presence of a synthetic magnetic field. In the model considered here, the synthetic magnetic flux across a polygonal plaquette of the graph depends on the number of edges of the plaquette. Specifically, within each triangular plaquette (white in Fig. 2.4(a)), a constant synthetic magnetic field flux of $-3\phi$ is accumulated. In contrast, as sketched in Fig. 2.4(b), the synthetic magnetic field threading each polygonal plaquette with at least four sides is different, and it can vary from $4\phi$ to $9\phi$, proportionally to the number of sides of the polygonal plaquette. Therefore, unlike the anomalous quantum Hall systems which feature a uniform magnetic flux inside hexagonal plaquettes [29, 30], the proposed amorphous system has a non-uniform magnetic flux across different plaquettes based on the real-space connectivity and topology. The statistical distribution of the magnetic flux per plaquette is shown in Fig. 2.4(c), and it can be controlled by changing the filling ratio in the original random disk sampling process. By preserving the local connectivity, the generated structure inherently possesses short-range order but lacks long-range order. This can be inferred from Fig. 2.4(d), where a flattened pair correlation function between vertices is observed, unlike periodic structures that exhibit characteristic sharp peaks. Despite the structural disorder, the system shows the hallmarks of nontrivial topology. By controlling the hopping phase, the system undergoes a topological phase transition which opens a nontrivial mobility gap. The topological nature of such a gap can be verified by calculating its Chern number via a topological marker as "Kitaev sum", shown in Fig. 2.4(e)[25, 28], whose value at some frequency $\omega$ expresses the accumulated Chern number from all the bands below the chosen frequency. The complex hopping term $e^{-i\phi}$ allows for a selective tuning of the quantized Kitaev sum across a phase boundary between $-1$ and $+1$, when $\phi$ is set to a value between 0 and $\pi$.

A non-zero topological marker in the gap implies that a finite-size system will exhibit chiral topological edge states, unidirectionally guided along the physical edge. These states, marked by a low density of states in the topological gap (Fig. 2.5(a)), emerge in both periodic and amorphous systems, and are robust to on-site potential disorder as long as the disorder strength is not comparable to the bandgap. However, while a strong enough on-site potential disorder will eventually overcome the topological protection of the edge states, an increasing degree of structural disorder will not affect the topological properties of the system, i.e. the edge states are topologically protected irrespective of the degree of structural disorder [26]. The regions with a higher density of states in Fig. 2.5(a) correspond to bulk bands, including a flat band at zero frequency. We classified the eigenstates $\psi$ by calculating their inverse participation ratio (IPR), defined as $\mathrm{IPR}\,(\psi) = \frac{\sum_i |\psi_i|^4}{\left|\sum_i |\psi_i|^2\right|^2}$, whose scaling law with respect to the lattice size is a measure of the localization of the eigenstates within finite-size systems. The IPR presented in Fig. 2.5(b) shows that our amorphous structure features three types of eigenmodes, that are: chiral edge (CE) modes, localized bulk (LB) modes, and extended bulk (EB) modes. The localization and the scaling properties of the modes with the size of

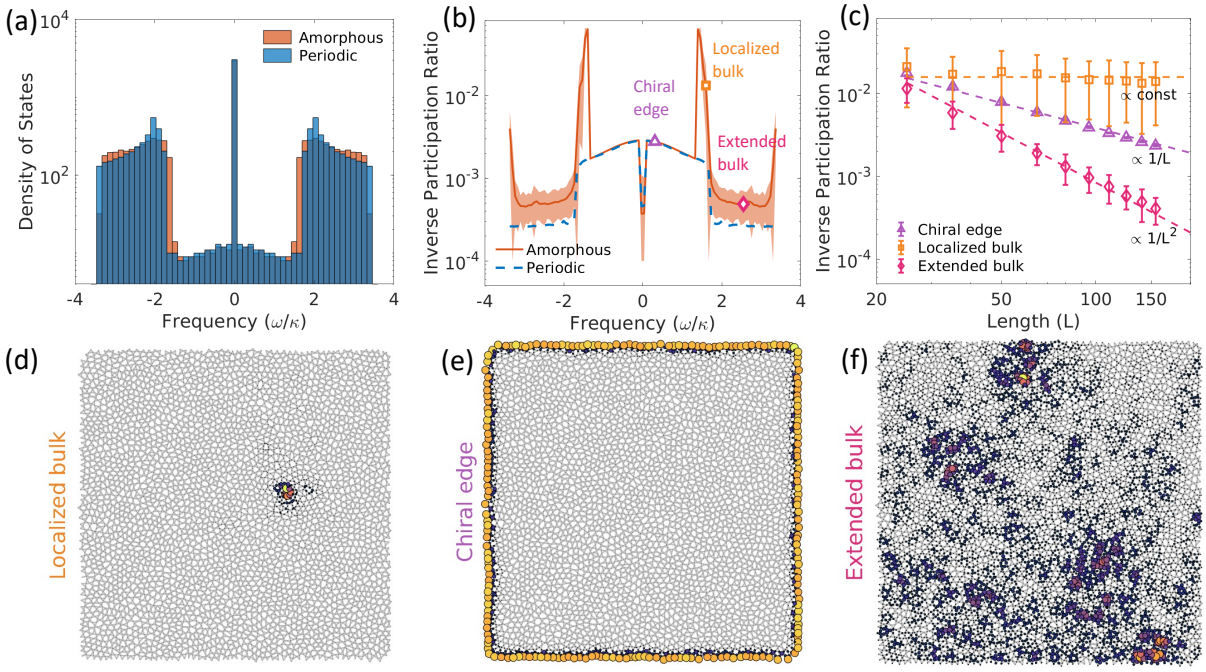


Figure 2.5: **Scaling of modes in periodic and amorphous topological graphs.** (a) Density of states for the amorphous and periodic topological graphs, for a hopping phase $\phi = \pi/2$. (b) Inverse participation ratio for the eigenmodes of the periodic and amorphous graphs. Three types of modes (chiral edge [CE], localized bulk [LB], and extended bulk [EB]) are observed with distinct inverse participation ratios (IPRs). The shaded area represents the standard deviation for 20 realizations of structural disorder. (c)Scaling of the IPR with the graph size $L$, for different modes. The results obtained by diagonalizing the linear Hamiltonian in Eq. (2.5) agree well with the theory, and the IPR of modes scales as a constant, $1/L$, and $1/L^2$ for LB, CE, and EB modes respectively. The error bars are obtained by averaging over 20 realizations. (d-f), Intensity profiles of three representative modes, classified as LB ((d)), CE (e), and EB (f), showing different localization features. The local light intensity is proportional to the size of the circles at each site, and it is visualized by thermal-like fill color.

amorphous graphs are summarized in Fig. 2.5(c). For a two-dimensional graph with disk sampling domain area $L^2$, the IPR scales as a constant for LB modes, as $1/L$ for CE modes, and as $1/L^2$ for EB modes. Intensity profiles of three representative modes are shown in Fig. 2.5(d-f). The IPRs of the CE modes scale like their periodic counterparts, indicating the existence of topological edge transport channels, while the LB modes, which are a unique feature of the amorphous system, originate from the presence of structural disorder. The LB modes stand out as characteristic peaks in the IPR of Fig. 2.5(b), occurring in the vicinity of the band edges, and they are responsible for the mismatch between the density of states of periodic and amorphous systems (Fig. 2.5(a)). The EB modes, that are spatially delocalized, feature low IPRs. The introduction of structural disorder has therefore dramatically changed the localization nature of the bulk modes, introducing the LB modes near the band edges. In addition, the remaining bulk modes are more localized, while the topological nature of the system is preserved.

## Periodic and amorphous system with Kerr nonlinearity

We now consider the nonlinear dynamics of the amorphous topological graph by including multi-particle interactions. As a prototypical example relevant for a wide class of systems, we will focus here on local two-particle interactions, such as the ones that occur between photons in a Kerr medium. The full Hamiltonian $\hat{H}$ describing the nonlinear graph is written by adding a term $\hat{V}$ to the linear Hamiltonian $\hat{H}_0$:

$$\hat{H} = \hat{H}_0 + \hat{V}, \tag{2.7}$$

where

$$\hat{V} = U_0 \sum_i \hat{n}_i^2, \qquad \hat{n}_i = \hat{a}_i^\dagger \hat{a}_i \,. \tag{2.8}$$

In Eq. (2.8), $U_0$ is a material-dependent strength of the nonlinearity and $\hat{n}_i$ is the particle number operator at site $i$. The time dynamics of the nonlinear system is obtained by explicitly integrating the time-evolution equations. The periodic and the amorphous topological systems are both driven with the same amplitude, which is spectrally peaked within the topological bandgap. Snapshots of the intensity distribution at different times $t$ are shown for the periodic (Fig. 2.6(a)) and amorphous (Fig. 2.6(d)) graphs. The energy of the propagating excitation is confined near the boundary at early time stages in both cases ($t_0 < 3T$), where $T = 1000\kappa^{-1}$ is approximately the time the signal takes to travel from the input to the output port. In the periodic case (Fig. 2.6(a)), the excited CE modes couple to other CE modes, and then leak towards the bulk as the EB modes are fed ($t = 5T$). This contrasts with the amorphous case, where energy is confined within the CE modes at $t = 5T$, as shown in Fig. 2.6(d). The difference in energy transport in the presence of nonlinearity is quantified by probing the transmission at the output port for different injected power levels, as shown in Fig. 2.6(b,e). For a relatively weak pumping power $P_0$, the transmission spectrum is similar in the periodic and amorphous systems. As the pumping power increases, the edge transport

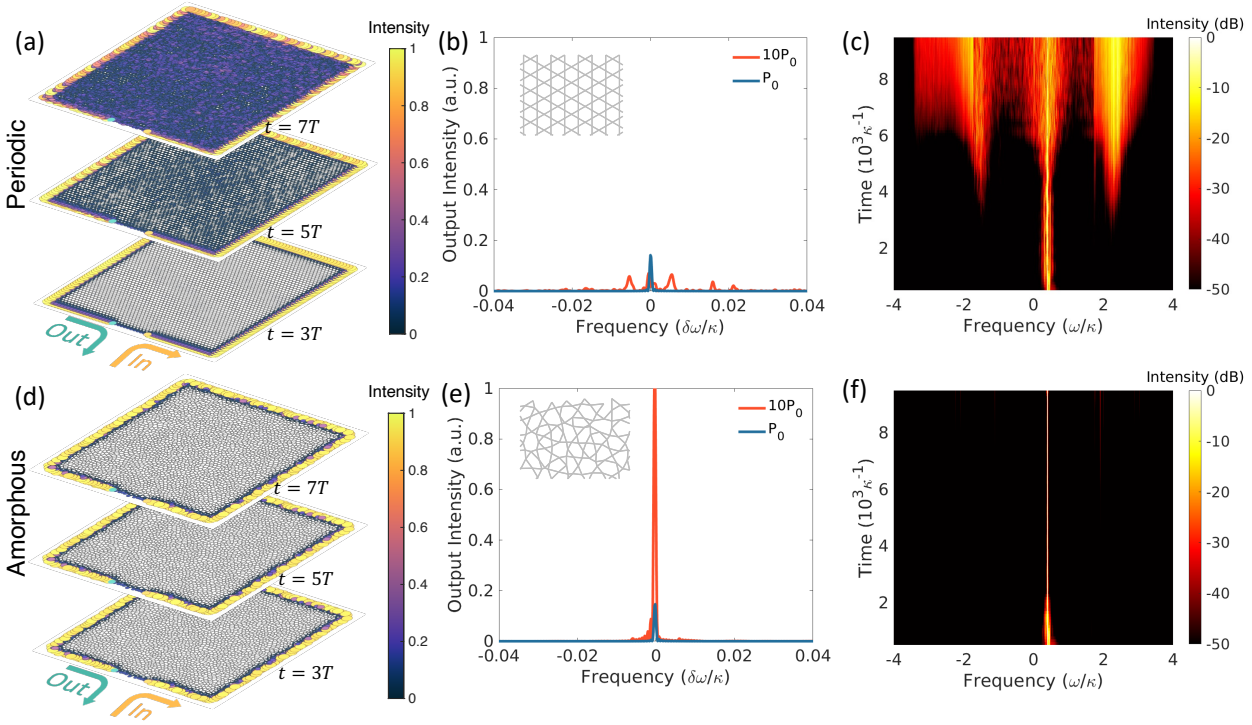


Figure 2.6: **Enhanced nonlinear topological transport in amorphous graphs.** (a,d), Snapshots of the real-space intensity distribution in periodic (a) and amorphous (d) structures, following an initial pulse excitation injected from the input channel, taken at times $3T$, $5T$, $7T$, where $T = 1000\kappa^{-1}$ is approximately the time it takes for the signal to travel from the input to the output port. Energy leaks from the edge to the bulk modes in the periodic graph, while it remains confined along the edge in the amorphous graph for longer times. (b,e), Power spectrum at the output channel for two different input powers $P_0$ and $10P_0$, for the periodic (b) and amorphous (e) graphs. The additional peaks in the periodic graph spectrum at $10P_0$ pumping correspond to the coupling between adjacent CE modes. The insets show a zoomed-in view of periodic (b) and amorphous (e) graphs. (c,f), Time-evolution of the power spectrum after injecting an initial signal at an edge mode frequency, obtained via a short-time Fourier transform. In the amorphous case (f), the energy couples to other edge modes or bulk modes at a slower rate compared to the periodic case (c).

channel breaks down in the periodic system due to the nonlinearity-induced coupling, while the transmission in the amorphous system maintains chiral edge propagation, leading to an almost tenfold increase in the peak power difference at the output. The stronger coupling between adjacent CE modes in the periodic case is confirmed by the presence of additional side peaks in the transmission spectrum. The evolution of the two systems in the time-frequency domain, obtained via a short-time Fourier transform, is presented in Fig. 2.6(c,f). In the periodic system, at early times, the initialized CE mode couples to the spectrally closest CE modes, resulting in frequency broadening. As time evolves, the coupling between the excited CE modes and EB modes, induced by the presence of the nonlinearity, ignites bulk modes, which in turn excite other EB and CE modes. The result, at long times, is a dramatically broadened spectrum. The amorphous system in Fig. 2.6(f), however, shows a strikingly different behavior, displaying both reduced oscillations between adjacent CE modes as well as a notably suppressed appearance of additional modes in the spectrum, achieving an almost unperturbed propagation for much longer times.

The increased isolation that the injected CE mode experiences in the amorphous system can be understood as an interplay of different mechanisms. First, the broken periodicity resulting from the introduction of structural disorder precludes us from identifying a well-defined momentum for the EB modes, hampering the fulfilment of phase-matching conditions for the nonlinearity-induced coupling, and suppressing the initial oscillations between CE modes. Second, according to Fermi's golden rule, the initially excited bulk modes will be located around the peak of density of states in Fig. 2.5(a), close to the band edges. These modes have an EB nature in the periodic system, but, with the introduction of structural disorder, some of them become LB modes in the amorphous system [31]. The localization of LB modes, then, delays the nonlinearity-induced propagation from CE to EB modes, with the latter being excited at much later times. The eventual propagation of the signal to the EB modes is in fact delayed by the introduction of structural disorder, but not completely suppressed, as an inevitable consequence of the presence of the nonlinearity.

## Four-wave mixing simulation

In this section, we consider the photon pair generation process in periodic and amorphous systems. In the spontaneous four-wave mixing process, we assume signal and idler photon pairs are generated and transported along the chiral edge states. In practice, e.g. in a microrings platform, the generated photon pairs can be hosted at different resonance frequencies of the ring resonators [32]. In this case, the frequencies of the generated light differ from the pump frequency by a free spectral range, so that the pump light can be filtered out. The Hamiltonian of signal and idler frequencies in the linear regime is assumed to be the same as the pump, which have chiral transport channels along the edge. The four-wave mixing Hamiltonian can be represented as [33]

$$H_{SI} = \begin{bmatrix} H_S & C \\ C^\dagger & H_I^\dagger \end{bmatrix}, \tag{2.9}$$

where $H_S = H_I = H_0$ and $C_{ij} = \chi_i(t)\delta_{ij}$. Here, the four-photon interaction strength at site $i$, represented as $\chi_i(t)$, is time dependent, and proportional to the intensity of the pump at site $i$. The linear dynamics of signal and idler frequencies are governed by the diagonal part of the Hamiltonian, while the pump-induced photon pair generation is represented as the off-diagonal component. The four-wave mixing process is simulated in the time domain under the undepleted pump assumption, as the pump experiences self-modulation, but it is not affected by signal or idler photons due to their relatively low intensity. To quantify the photon pair generation efficiency, a small signal at idler frequency is injected into the system, and the signal at the output port is recorded and Fourier-transformed to obtain the spectral information. The evolution of the generated signal photon spectrum over time is calculated by a short-time Fourier transform of the output signal. A snapshot of the field distribution in the amorphous system is shown in Fig. 2.7, where the pump, idler and signal field profiles are plotted in panels (a), (b), (c), respectively. In the photon pair generation process, the momentum and energy conservation has to be satisfied. In the amorphous system, the effective momenta of the excited edge modes can be estimated by calculating the phase differences between adjacent sites along the edge, which are visualized as zoomed-in views in Fig. 2.7(d–f). The accumulated phase differences are plotted against the site index in Fig. 2.7(g), from which we can extract the average phase shift per site as $\Delta\phi_p = -0.293, \Delta\phi_i = -0.583, \Delta\phi_s = -0.012$. The momentum conservation can then be verified in terms of the phase differences as $2\Delta\phi_p = \Delta\phi_s + \Delta\phi_i$, which is a natural consequence of the four-wave mixing simulation.

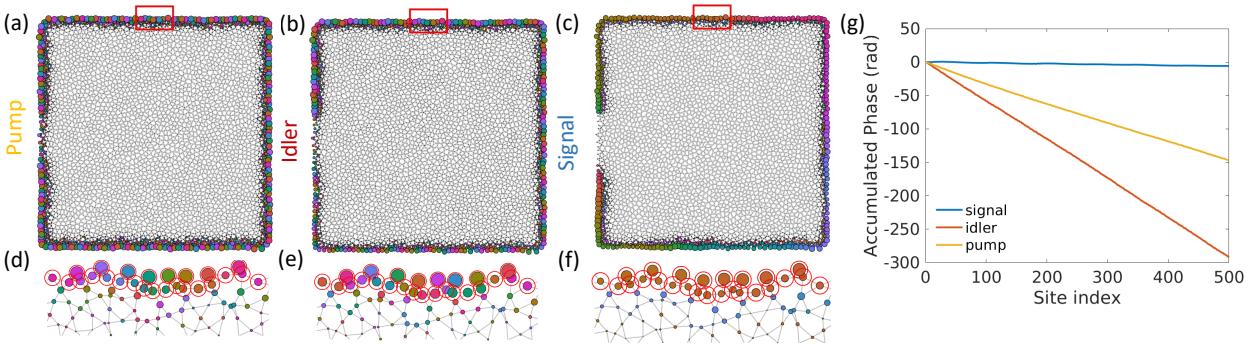


Figure 2.7: **Four-wave mixing field profiles.** The light is injected into the input port and coupled out at the output port, similar to Fig. 3 of the main text. (a–c), Field profiles for pump (a), idler (b), and signal (c), where the color (size) represents the phase (amplituede) at each site. (d–f), Zoomed-in view of the field distribution at sites along the edge. Red circles indicate the sites used for the phase calculation in (g). (g), Accumulated phases over 500 edge sites for pump, idler and signal fields.

## Photon pair generation in periodic and amorphous systems

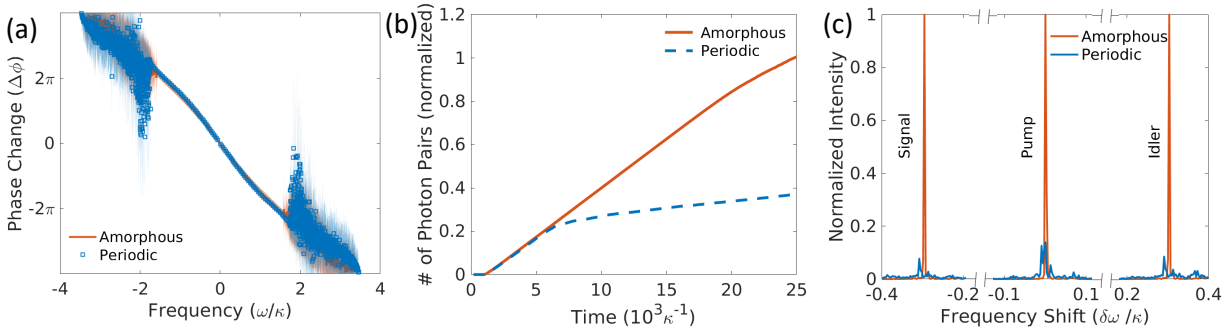


Figure 2.8: **Disorder-enhanced topological light generation.** (a) Effective dispersion relation of amorphous and periodic edge states, obtained by plotting the average phase change between consecutive triangular plaquettes along the edge against the frequency of each eigenmode. For the amorphous system, dispersion broadening is observed due to the aperiodic variation of the phase at different positions along the edge state. Note that, for bulk modes, the quasi-linear phase change breaks down due to the lack of well-defined transport channels. (b) Time evolution of the total number of generated photon pairs. The photon pair generation rate (slope of the curve) decreases in the periodic system as the signal/idler modes couple to the EB modes, while the generation rate remains high for longer time in the amorphous system. (c)Example of the normalized spectra of photon pairs generated via a pump at frequency $\omega_p = 0.4\kappa$. The spectra are centered at the pump frequency.

The spatial and spectral energy confinement in the presence of nonlinearity can be used, for example, to enhance the efficiency of quantum topological photon-pair generation via spontaneous four-wave mixing in optical systems [32, 34]. In this non-linear four-photon process, a pump signal is injected into the system via an input port, and the correlated photon pairs generated within the topological bandgap are guided towards the output port along the boundaries. The positions of input and output ports are chosen as shown in Fig. 2.6(a,d) to increase the distance travelled by the pump signal, thereby maximizing the photon pair generation efficiency. The system is described by the following Hamiltonian [32, 33, 35],

$$H_{SI} = H_0^{(S)} + H_0^{(I)} + \sum_i \chi_i \hat{a}_i^{(S)\dagger} \hat{a}_i^{(I)\dagger} \tag{2.10}$$

where the last term creates correlated pairs of photons, called signal (S) and idler (I), at a site-dependent rate $\chi_i = \chi_0 \hat{a}_i^{(P)} \hat{a}_i^{(P)}$ which depends both on the pump (P) strength and on the optical nonlinearity $\chi_0$. The terms $H_0^{(S/I)}$ are the bare Hamiltonians of the signal and idler photons, respectively. The effectiveness of this process typically relies on working with a quasi-linear dispersion to satisfy both energy and momentum conservation. As shown in

Fig. 2.8(a), the topological dispersion in our system fulfills this requirement. The photon pair generation efficiency is presented in Fig. 2.8(b). Both the periodic and the amorphous system generate a similar number of photon pairs at early times. At later times, however, the efficiency of the periodic system drops due to the increased coupling between CE and EB modes, while the amorphous system remains efficient. The enhanced spectra of signal, pump and idler are presented in Fig. 2.8(c). In the periodic case, the self-modulation of the pump leads to a reduced lifetime of the edge modes at the excitation frequencies, hence the photon pair generation rate is also reduced, while in the amorphous case, the pumped edge states can generate more photon pairs.

## 2.4 Experimental results

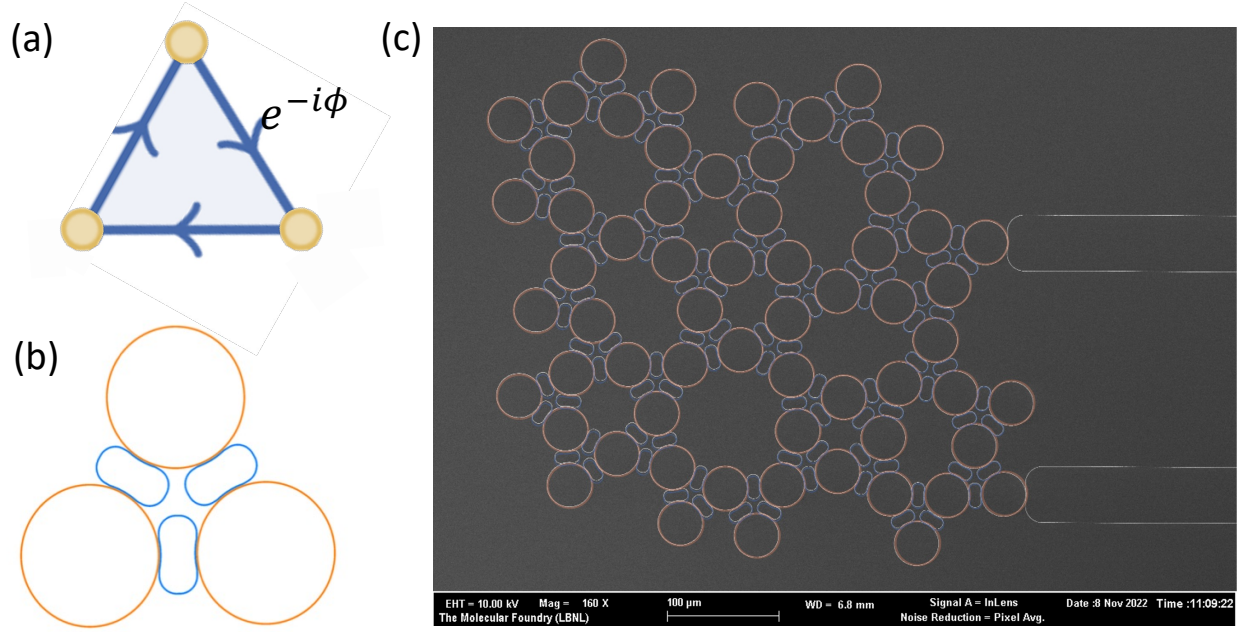


Figure 2.9: **Experimental implementation of the amorphous topological graph with micro-ring resonator array.** (a) Unit cell in tight-binding model and (b) its implementation with micro-ring resonators. (c) The SEM image of the amorphous topological system with micro-ring resonators.

The proposed amorphous topological system similar to Fig. 2.4 can be implemented with a 2D micro-ring resonator array. The system consists of a triangular unit with a phase-delayed hopping between adjacent sites as shown in Fig. 2.9(a), which is implemented as coupled micro-ring resonators in Fig. 2.9(b). The yellow micro-ring resonators are on resonance at the working frequency, while the blue resonators are non-resonant and provide the delayed

phase by a transverse shift of their centers. A more detailed description of the configuration can be found in [36]. The amorphous graph is constructed and the SEM image is shown in Fig. 2.9(c), where two bus waveguides are used for input and output.

As a preliminary result, we observe the topological edge propagation along the boundary of the systemFig. 2.10 by monitoring the scattered light using an infrared camera on top of the device. The direction of propagation is determined by the sign of the topological index calculated at the excitation frequency.

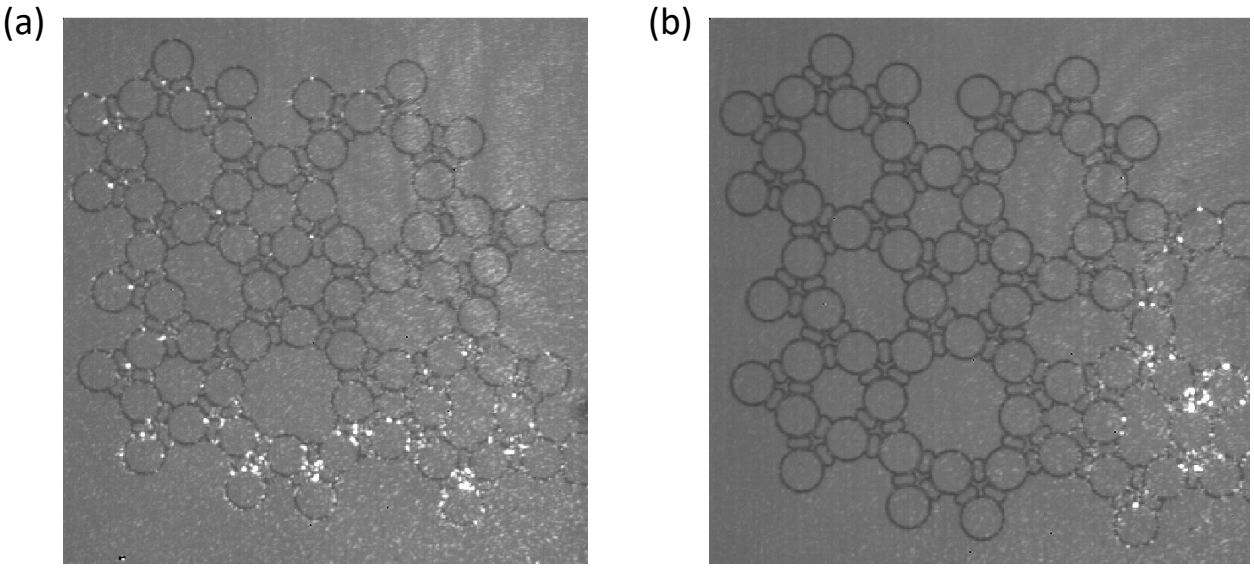


Figure 2.10: **Experimental observation of edge transport in amorphous topological micro-ring resonator array.** The edge transports are excited at the topological gap frequencies with different Chern numbers: (a) +1 and (b) -1.

## 2.5 Discussion

### Robustness to on-site disorder

Despite the structural disorder, the amorphous system is robust to on-site (potential) disorder, up to a certain strength. In actual physical systems, such disorder may stem from fabrication imperfections that e.g. shift the natural frequency of the resonators employed as lattice sites. The on-site disorder is assumed here to follow a Gaussian distribution, characterized by the standard deviation $\sigma$ which we sweep for the numerical simulations. The existence of a transport channel along the topological edge state is probed at the output site, with a single frequency excitation on the input port. The transport can be visualized by the intensity distribution at the steady state, shown in Fig. 2.11(a-c). As the strength

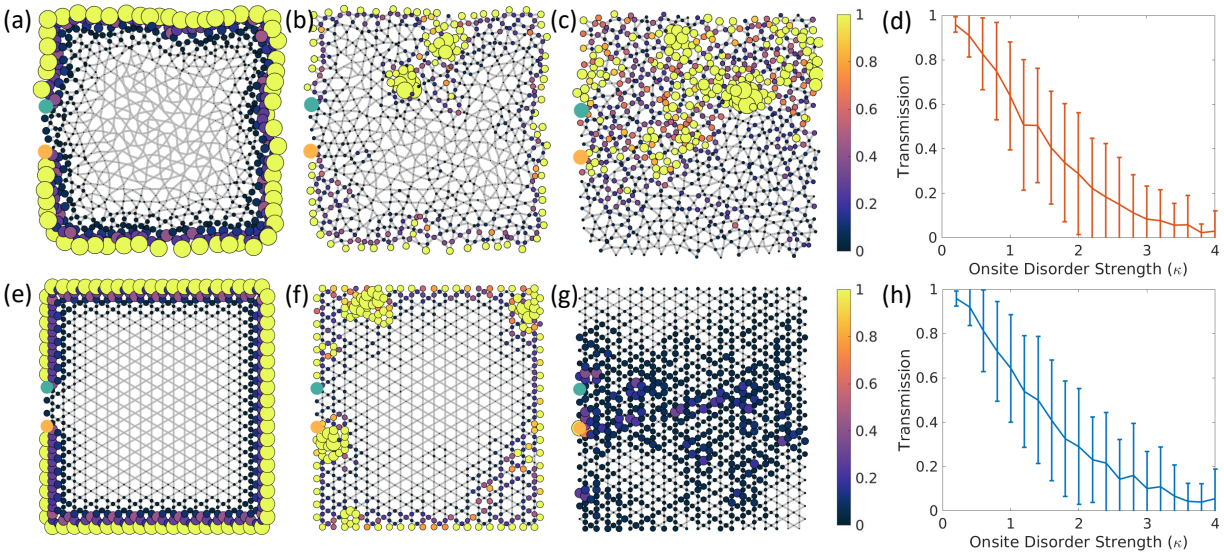


Figure 2.11: **Robustness to on-site disorder.** (a–c), Topological transport on an amorphous graph with different on-site potential disorder. The disorder strength is characterized by the standard deviation of a Gaussian distribution with $\sigma/\kappa = 0$ (a), 0.4 (b), 1.6 (c). The transmission with increasing on-site potential is summarized in (d) by averaging over 100 realizations of disorder. (e–h), Topological transport on a periodic graph with potential disorder, similar to (a–c).

of on-site disorder increases, the edge state couples to localized modes near the boundary and the transport efficiency is reduced to half when the standard deviation of the on-site disorder is equal to the coupling strength between sites, $\kappa$. As shown in Fig. 2.11(d, h), the transmission is further reduced to less than 5% as the disorder strength reaches $3\kappa$.

## Different amorphous realizations and truncations

We show the generated amorphous topological graph, following the generation procedure described in Section 2.2 with a square boundary shape. Next, we show that the enhanced transport in amorphous system is independent of the specific realization of structural disorder, and is not limited to a square boundary truncation. As an example, we implement different realizations of the amorphous graphs, and compare them with the periodic systems truncated at different orientations. For each system, the same signal is injected into the structure and the short-time Fourier transform is computed, in order to capture the frequency information of the lattice intensity over time. For the amorphous graph, the short-time Fourier transform is similar to the square cut in Fig. 2.6, as different truncations of the graphs have negligible effect on the amorphous system. The periodic system,

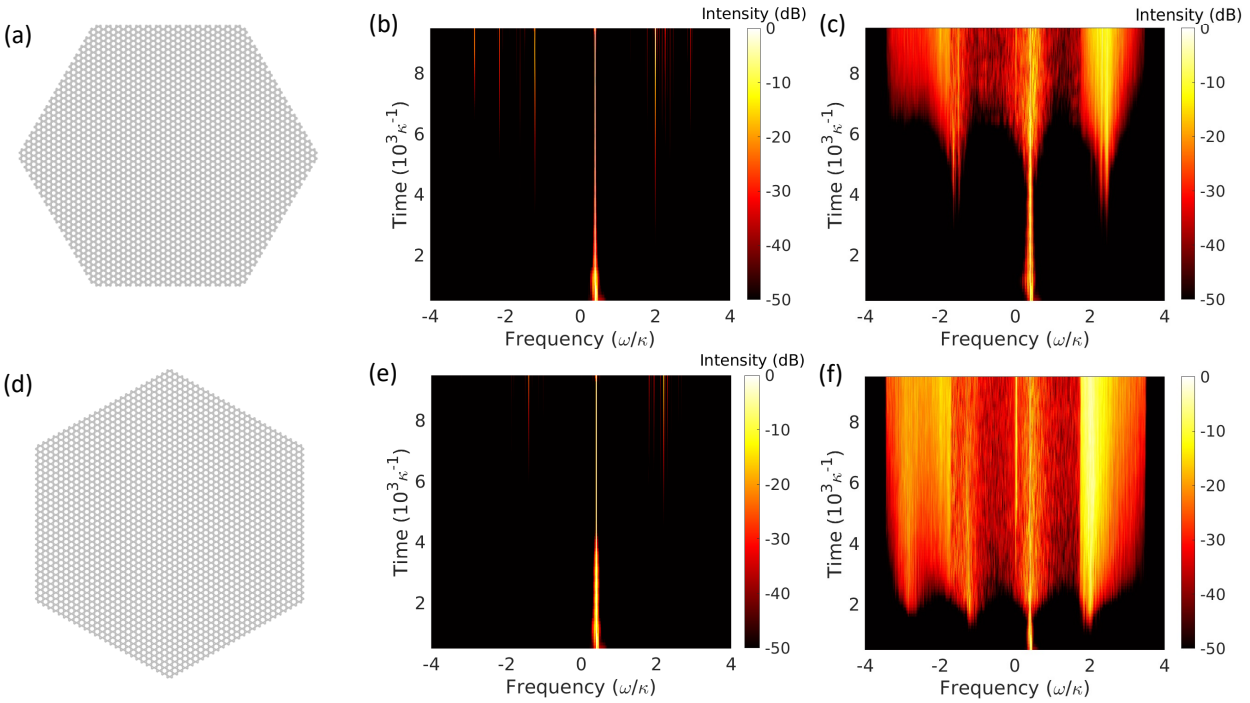


Figure 2.12: **Different realizations and truncations.** The periodic system is truncated along different lattice orientation directions, and the short-time Fourier transform of the signal is compared to the amorphous system. (a) Armchair-like truncation of the periodic lattice. (b) Short-time Fourier transform of energy transported in an amorphous system with nonlinearity. (c)Short-time Fourier transform for transport in the periodic system. (d–f), Same as (a–c), but with a zig-zag-like truncation.

however, shows different response under different truncation orientations. Nevertheless, the energy confined in the edge state of the amorphous system decays at a much slower rate compared to the periodic system, independently of the truncation choice.

## 2.6 Conclusion

We proposed and demonstrated an amorphous topological platform (graph) to enhance non-linear phenomena. The disordered topological graphs are based on the control of a synthetic magnetic field threading through different polygonal plaquettes and leading to a non-uniform flux that gives rise to the non-trivial topology of the graph. The non-linear responses of such amorphous topological graphs outperform their periodic counterparts owing to the emergence of localized bulk modes and to a reduced phase matching, enabling the ultrafast guiding of energy, protected against leakage. The accumulation of energy in the topologically protected

channel enhances the generation of photon pairs. The proposed scheme for enhancing nonlinear responses via the introduction of structural disorder in topological systems will have a broad range of applications, including novel devices for robust light-based information processing and computing.

# Chapter 3

# Enhancing nonlinearity with potential disorder: inverse-designed cavities

## 3.1 Introduction

Over the last decades, various nanophotonic platforms have been proposed to implement and enhance nonlinear photon generation processes, including wire waveguides [37, 38], nanobeam cavities [39], metamaterials [40], micro-ring resonators[41, 42, 43, 35, 44, 45, 46, 32, 47, 48, 49, 50], periodically poled waveguides/cavities[51, 52], and photonic crystal cavities[53]. It is well-known that high-quality factor cavities designed at target frequencies can bolster the nonlinear process by enhancing the field with confinement. Yet, the effective phase matching conditions are typically challenging to satisfy in non-conventional cavity structures. Without effective phase-matching, the generated photons from different positions in nonlinear materials can destructively interfere, reducing the total generation efficiency. Such issues can be addressed by computational inverse design [54, 55, 56, 57, 58, 59, 60, 61].

Recently, the adjoint method has been generalized to optimize nonlinear photonic processes, such as second harmonic generation or optical switches based on the Kerr effect [62, 63, 64, 65]. However, existing inverse-design methods for nonlinear frequency generation [66] face difficulties in generalization to multi-photon generation processes. Moreover, coupling efficiencies for both input and output channels are often overlooked due to the optimization complexity. In addition, an intuitive understanding of the inverse-designed structure is unclear. The optimized structure often lacks interpretability, making it challenging to gain insights into how and why the inverse design method works.

To address these challenges, we put forth an inverse design approach to amplify the efficiency of on-chip photon pair generation. We implement this strategy using the open-source package `EmOpt` [67]. Our method employs a multi-frequency co-optimization strategy and calculates gradients with respect to the design parameters via the adjoint method. The resulting efficiency enhancement stems not only from the increased field intensity due to the confinement of light in high quality factor cavity resonances but also from the improvement

of phase-matching conditions. We demonstrate the capability of the proposed method by fabricating and characterizing an optimized device that enables the efficient generation of photon pairs. Interestingly, the shape of the proposed design can also be explained by an effective potential method, and the approximate solution aligns well with the finite-difference frequency domain (FDFD) simulation results. The proposed optimization strategy can be generalized to other nonlinear processes for compact frequency-mixing devices on-chip, and the performance can be further improved using global optimization methods [68, 69].

## 3.2 Theory

### Inverse Design Principles

Conventional design methods often depend on an extensive physical understanding of systems, leading to time-consuming processes and demanding expertise. There has been a lot of research effort seeking to simplify this process, by employing advanced optimization techniques with computing resources. The inverse design method, i.e., direct target for a given desired function and computationally find the optimized design structure, has enabled the development of devices with both compact footprints and novel functionalities in a variety of fields in engineering, including acoustics, optics, mechanics, etc.

In photonics inverse design, the governing framework is provided by Maxwell's equations. A typical inverse-design problem in the frequency domain can be expressed as follows:

$$\min_{\vec{p}} f(x) \tag{3.1}$$

where $x$ represents the field distribution constrained by Maxwell's equations $Ax = b$. Here, $b$ is the source distribution and $A$ denotes the frequency-domain Maxwell operator, which depends implicitly on the input parameters as [67]

$$A = \begin{bmatrix} j\omega\epsilon & \nabla\times \\ \nabla\times & -j\omega\mu \end{bmatrix} \Rightarrow \begin{bmatrix} j\omega\epsilon(\vec{p}) & \nabla\times \\ \nabla\times & -j\omega\mu(\vec{p}) \end{bmatrix} \tag{3.2}$$

Thus, the design challenge is to identify the optimal parameter combination $\vec{p}$ that minimizes (or maximizes) a target function $f(x)$ of the field distribution $x$, with a predefined source distribution $b$. These optimization problems are computationally expensive, due to the target function's implicit dependence on input parameters and its non-convex nature. To optimize the target function, gradient-based methods have several advantages over the non-gradient-based methods in terms of convergence rate, precision, and scalability. Nevertheless, to calculate the gradients of the figure of merit, it may require a large number of times to solve Maxwell's equations with different structure configurations. To reduce the number of calculations in the optimization process, the adjoint method can be helpful, especially in the case where the number of parameters is large. Using the chain rule, the derivatives of the figure of merit with respect to each input parameter can be represented as

$$\frac{df}{dp_i} = -2\Re\left(y^T \frac{dA}{dp_i} x\right) \tag{3.3}$$

where $x(y)$ is the field distribution of the forward (adjoint) simulation, and $dA/dp_i$ are computationally easy-to-calculate shape derivatives. Here, the adjoint field $y$ is the solution of equation $A^T y = df/dx$, with a different source configuration $df/dx$ depending on the figure of merit instead of the original source configuration $b$. Therefore, the gradients with respect to parameters $df/dp_i$ can be calculated with two Maxwell simulations for the field distributions $x$ and $y$, in addition to the shape gradients $dA/dp_i$. The total number of Maxwell simulations required for each iteration is two and is independent of the number of parameters.

The requisite gradient calculations in this context bear a striking resemblance to those in neural network training, where back-propagation is employed. A detailed comparison is included in Chap.A. It has also been shown that the derivative calculations can be automatically taken care of with the software package. The recent development of automatic differentiation methods, for example, Jax package [70], enables automatic differentiation of arbitrary complex functions defined based on Python or Numpy functions. This also allows simpler calculation of gradients by writing the Maxwell solver using such auto-diff package [71]. Compared to the adjoint method, which still requires a physical understanding of the adjoint system (e.g. how to set up the adjoint source), this novel computational method greatly simplifies the process and allows efficient gradient calculations for an arbitrary figure of merit. The potential drawback is that such a method may need more computational resources for a time-domain Maxwell solver compared to the adjoint method. It would be interesting to compare the two methods in more detail as future research directions.

## Phase Matching in Nonlinear Optics

In this work, we are interested in extending the inverse design method to nonlinear photon generation. Here, we first briefly review the basics of the frequency generation process in nonlinear optics. In the microscopic picture, the origin of nonlinear frequency generation lies in the atom-light interaction. The impulse-response function, representing the atom's induced polarization, includes nonlinear terms, which can be represented in the time domain as an expansion of the electric field [72]:

$$P(t) = \varepsilon_0 \left[\chi^{(1)} E(t) + \chi^{(2)} E^2(t) + \chi^{(3)} E^3(t) + \ldots\right] \equiv P^{(1)}(t) + P^{(2)}(t) + P^{(3)}(t) + \ldots \tag{3.4}$$

where $P(t)$ is the induced polarization field, $E(t)$ is the driving electric field, and $\chi^{(i)}$ is the $i$th-order of susceptibility. In contrast to the linear regime, where only the first-order dependence $\chi^{(1)}$ is non-zero, the high-order terms are no longer negligible in the nonlinear case. Greater insight is obtained by rearranging the nonlinear equation, positioning linear terms on the left and high-order polarization field responses on the right [72]:

$$\nabla^2 E - \frac{n^2}{c^2}\frac{\partial^2 E}{\partial t^2} = \frac{1}{\varepsilon_0 c^2}\frac{\partial^2 P^{NL}}{\partial t^2} \tag{3.5}$$

where $P^{NL} = P^{(2)}(t) + P^{(3)}(t) + \ldots$ The above equation can be understood as the nonlinear polarization becomes the source for the frequency generation.

In nonlinear processes, efficient energy transfer hinges on the phase-matching condition, the synchronization of interacting wave phases while propagating through the nonlinear medium. Mathematically, in a homogeneous medium, the phase matching can be represented in terms of momentum conservation as $\Delta k = k_{new} - \sum k_{original} = 0$. In the above time domain equation, it incdicates that the nonlinear polarization field ($\sum k_{original}$) determines the momentum of the generated field ($k_{new}$). In a second-order nonlinear process, for example, dipoles are generated at a frequency of $2\omega$. In a homogeneous medium, the phase-matching condition is equivalent to momentum conservation as $2k(\omega) = k(2\omega)$. In inhomogeneous media, supported modes diverge from plane waves, resulting in undefined mode momenta. In this case, the effective phase matching can be considered constructive interference for dipoles generated at different locations inside the nonlinear material, which will be discussed in more details in the next section.

## Generalized Phase Matching in Cavity

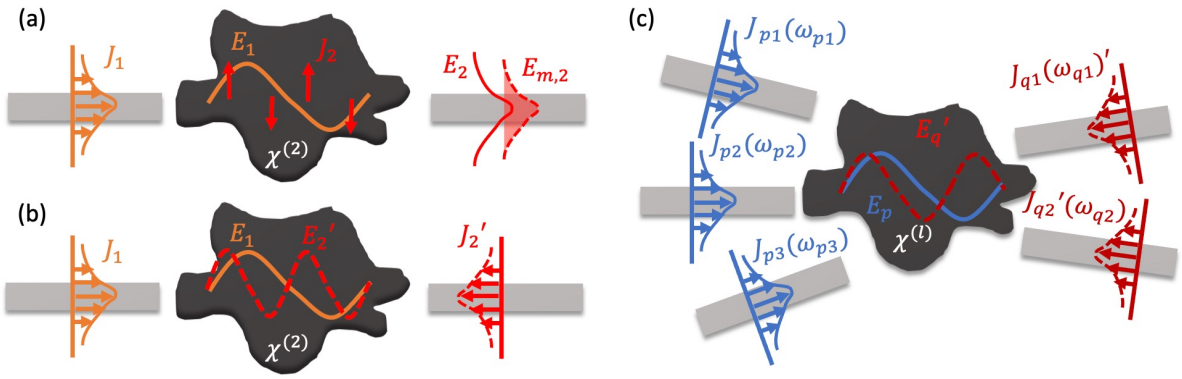


Figure 3.1: **Schematics for second harmonic generation and generalization to multi-photon nonlinear process in a cavity of arbitrary shape.** (a) Forward process and (b) adjoint process for second harmonic generation in the cavity. The gray rectangles represent the coupled waveguides. (c) Generalization to multi-photon nonlinear process.

We first discuss the phase matching condition in a cavity in the example of the on-chip second harmonic generation. A guided mode at frequency $\omega_1$ is injected into the cavity, exciting the field $E_1$ inside the cavity. Due to the material nonlinearity $\chi^{(2)}$, the field distribution at fundamental frequency creates the second harmonic polarization field $P_2 = \epsilon_0 \chi_1^{(2)} E_1^2$ at

$\omega_2 = 2\omega_1$, which becomes the sources $J_2$ for exciting the field distributions at second harmonic. The subscript $1, 2$ represent the frequency $\omega_1$, $\omega_2$, respectively. The process is shown in Fig. 3.1(a), where the sources $J_2$ are represented as the red arrows. These nonlinear dipole sources generate the field distribution $E_2$ at $\omega_2$. The on-chip generation efficiency, $\eta$, is defined as the mode-matching integral. Here, we adopt a naive version of expression as the overlap between the second-harmonic field $E_2$ and the target waveguide mode $E_{m,2}$ of the output channel:

$$\eta = \int_{wg} E_2(r) \cdot E^*_{\mathrm{m},2}(r) dr \,. \tag{3.6}$$

Given such figure of merit, the optimization can be solved by the adjoint variable method. A similar method has been used in Ref. [62] for the second-harmonic optimization in free space. When generalizing this formalism to spontaneous photon creation processes, the main challenge is that the spontaneously generated photons cannot be easily represented as dipole sources. If random dipole sources are introduced in the cavity to create the polarization field, the configurations of dipoles may lead to nonphysical results [62].

To address this issue, we can rewrite the efficiency in (3.6) by exploiting Lorentz reciprocity. With the assumption of undepleted pump, the material properties satisfy $\epsilon = \epsilon^\intercal, \mu = \mu^\intercal$ and Lorentz reciprocity holds at $\omega_2$ [73]. The efficiency in (3.6) can then be rewritten as

$$\eta \propto \int_{wg} E_2(r) \cdot J_2'^*(r) dr = \int_{cav} J_2(r) \cdot E_2'^*(r) dr = \epsilon_0 \int_{cav} \chi^{(2)} E_2'^*(r) E_1^2(r) dr \,. \tag{3.7}$$

In the first step, the guided mode field distribution is related to the current sources as $J_2' = \epsilon_0 \chi_2^{(1)} E_{m,2}$. The second step is based on the Lorentz reciprocity, which is shown in Fig. 3.1(b). The guided modes to be matched at the output are injected backward into the nonlinear cavity, and the efficiency can be represented as the overlap integral of the forward field and adjoint fields. Here, $J_2'$ is the adjoint source in the reciprocal process and $E_2'$ is the generated field.

Next, we generalize this formalism to multi-photon generation process, for example, spontaneous four-wave mixing (sFWM). In the generalized multi-photon process, where multiple photons at different frequencies are involved, the figure of merit can then be represented as

$$\eta = \int_{cav} \chi^{(l)}(r) \prod_{p \in \omega_{fwd}, q \in \omega_{adj}} E_p(r) E_q^*(r) dr \,. \tag{3.8}$$

## Perturbation Theory for Non-periodic Photonic Crystal

A frequently posed question about inverse-designed structures concerns their physical interpretability. Specifically, can we learn more physical insights from the optimized structures and use such insights as guidance for future design challenges? For most inverse-designed devices, the response tends to be negative. The commonly used topological optimization

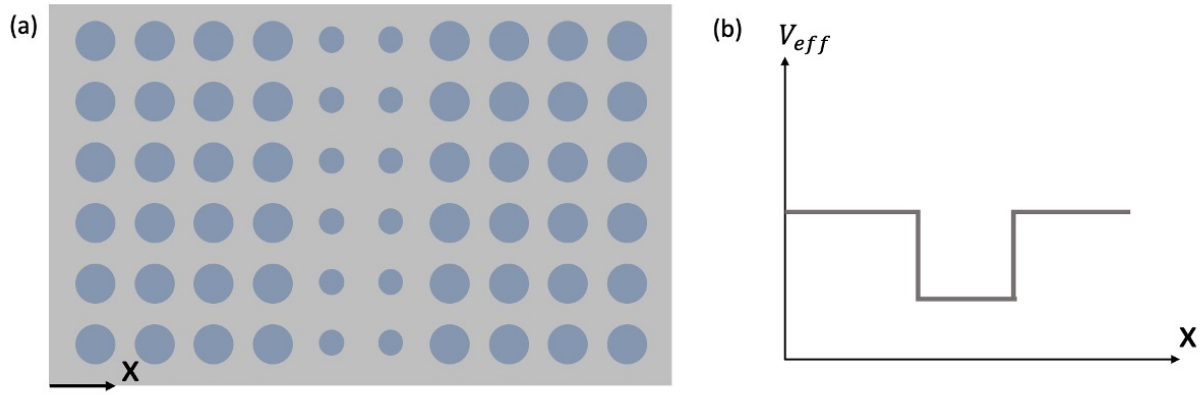


Figure 3.2: **Schematic figure of a perturbed photonic crystal and its effective potential.** (a) Top view of a perturbed 2D photonic crystal. (b) The effective potential of the perturbed photonic crystal system.

method relies on multi-reflection in the structure, and therefore it can be quite challenging to understand intuitively or physically how and why the optimized stricture would work. For a more physically intuitive understanding of the optimized device, we consider the simpler structure of a non-periodic photonic crystal. In this section, we develop a perturbation theory based on the existing effective potential method for the one-dimensional photonic crystal structure. The results will be used to provide a physical interpretation of the optimized cavity for spontaneous four-wave mixing.

As an example of a non-periodic photonic crystal device, Fig. 3.2(a) shows the top view of a 2D photonic crystal structure, with the middle region having a smaller radius. This photonic crystal heterostructure [74] can be approximated with a 1D effective potential (shown in Fig. 3.2(b)) using perturbation theory when differences between the photonic unit cells of each section are minimal. In the derivation of the effective potential, previous research [75] assumes the period of each unit cell remains the same. Our derivation extends these conclusions to scenarios where the periods of the unit cells undergo perturbations. We show that the effective potential method can still be applied, and the potential profile is obtained by simulating each unit cell with periodic boundary conditions for the band-edge frequency. Therefore, we can calculate the field distribution of the eigenmode in such a non-periodic photonic structure with a simplified 1D model, and provide an intuitive understanding of the structure.

In a periodic photonic crystal, optical waves propagate in the form of Bloch wave function;

$$H_{\mathbf{k}}(\mathbf{r}) = \frac{1}{L} h_{\mathbf{k}}(\mathbf{r}) e^{i\mathbf{k}\cdot\mathbf{r}} \tag{3.9}$$

When a slow and weak perturbation is introduced in the structure, different Bloch waves

within the neighborhood of the band extrema ($\mathbf{k}_0$) are coupled to form a localized mode.

$$H_d(\mathbf{r}) = \frac{1}{L}\sum_{\mathbf{k}\sim\mathbf{k}_0} \tilde{\Gamma}_0(\mathbf{k}-\mathbf{k}_0) h_{\mathbf{k}} e^{i\mathbf{k}\cdot\mathbf{r}} \tag{3.10}$$

where $\tilde{\Gamma}_0(\mathbf{k}-\mathbf{k}_0)$ is the Fourier space envelope function near $\mathbf{k}_0$. Assuming that the Bloch mode $h_{\mathbf{k}}$ does not significantly change within the neighborhood of $\mathbf{k}_0$, the mode solution can be approximately expressed as a product of the Bloch wavefunction at $\mathbf{k}_0$ and an envelope function $\Gamma_0(\mathbf{r})$ [75]:

$$H_d(\mathbf{r}) \approx \frac{1}{L} h_{\mathbf{k}_0} e^{i\mathbf{k}_0\cdot\mathbf{r}} \sum_{\mathbf{k}-\mathbf{k}_0} \tilde{\Gamma}_0(\mathbf{k}-\mathbf{k}_0) e^{i(\mathbf{k}-\mathbf{k}_0)\cdot\mathbf{r}} = \frac{1}{L} h_{\mathbf{k}_0} e^{i\mathbf{k}_0\cdot\mathbf{r}} \Gamma_0(\mathbf{r}) \tag{3.11}$$

The Wannier-like equation for the envelope function $\Gamma_0(\mathbf{r})$ is found to follow

$$\Big\{\Big[\lambda_d - \lambda_0(\mathbf{k})\Big] - \Delta\eta'(\mathbf{r})\Big\}\Gamma_0(\mathbf{r}) = 0 \tag{3.12}$$

where $\lambda_d \equiv (\omega_d/c)^2$ is the eigenvalue of the mode, $\lambda_0(\mathbf{k}) \equiv [\omega(\mathbf{k})/c]^2$ is the unperturbed band frequency squared evaluated at the momentum $\mathbf{k}$ in the neighborhood of $\mathbf{k}_0$, and $\Delta\eta'(\mathbf{r})$ is the effective potential perturbation at the position $\mathbf{r}$. As we consider quasi-1D structure in this work, we regard the momentum $\mathbf{k}$ and the position $\mathbf{r}$ as scalar variables $k$ and $x$, respectively, in the following derivation.

The unperturbed band term can be Taylor expanded near the band edge as

$$\lambda_0(k) = \lambda_0(k_0) + \left.\frac{\partial\lambda_0}{\partial k}\right|_{k_0}(k-k_0) + \frac{1}{2}\left.\frac{\partial^2\lambda_0}{\partial k^2}\right|_{k_0}(k-k_0)^2 + \cdots \tag{3.13}$$

$$\approx \lambda_0(k_0) + \frac{1}{2m}(k-k_0)^2 \tag{3.14}$$

$$= \lambda_0(k_0) - \frac{1}{2m}\frac{\partial^2}{\partial x^2} \tag{3.15}$$

Here we used the fact that the first derivative $\partial\lambda_0/\partial k$ is zero at the band edge $k = k_0$, and the effective mass is given by $1/m \equiv (\partial^2\lambda_0/\partial k^2)|_{k=k_0}$. We also replaced the momentum difference with the gradient operator by the definition of the real-space envelope function $\Gamma_0(x) = \sum_{k-k_0}\tilde{\Gamma}(k-k_0)e^{i(k-k_0)x}$ as $(\partial_x/i)^2\,\Gamma_0(x) = (k-k_0)^2\Gamma_0(x)$. Therefore, (3.12) can be rewritten as

$$\Big\{\lambda_d - \Big[\lambda_0(k_0) + \Delta\eta'(x)\Big] + \frac{1}{2m}\frac{\partial^2}{\partial x^2}\Big\}\Gamma_0(x) = 0 \tag{3.16}$$

The definition of the effective potential perturbation is given by

$$\Delta\eta'(x) = -\Delta\eta(x)\,\langle H_{k_0}|\nabla^2 H_{k_0}\rangle - \nabla[\Delta\eta(x)]\cdot\langle H_{k_0}|\nabla H_{k_0}\rangle \tag{3.17}$$

where $\Delta\eta(x \in X_n)$ is the perturbation in the $n$-th grating domain $X_n$, and $\langle a|b\rangle$ is the overlap integral over a unit cell, $\langle a|b\rangle \equiv \int_v dx\; a^* b$. In particular, the even/odd symmetry of

$H_{k_0}(x)$ at the Brillouin zone edge implies that $\langle H_{k_0}|\nabla H_{k_0}\rangle = 0$. This in turn implies that $\Delta\eta'(x_n)$ depends only on the first term of the right-hand side of (3.17), containing the local perturbation $\Delta\eta$, but not on its gradient $\nabla(\Delta\eta)$, which is related to the adjacent unit cell. Therefore, the potential perturbation $\Delta\eta'(x \in X_n)$ can be found by performing unit cell simulations for each grating with periodic boundary conditions. The periodic boundary condition can be considered as a homogeneous perturbation, which leads to a constant envelope function $\Gamma_0$. In this case, the term $(\partial_x^2/\partial x^2)\Gamma_0 = 0$, and the band edge of the $n$-th grating, $\lambda_{0,n}(k_0)$, will be

$$\lambda_{0,n}(k_0) = \lambda_0(k_0) + \Delta\eta'(x \in X_n) \tag{3.18}$$

By substituting (3.18) into (3.16), the Wannier-like equation for the envelope function can be rewritten in the form of an eigenvalue problem:

$$\left[-\frac{1}{2m}\frac{\partial^2}{\partial x^2} + \lambda_0(k_0, x)\right]\Gamma_0(x) = \lambda_d\Gamma_0(x) \tag{3.19}$$

where $\lambda_0(k_0, x \in X_n) = \lambda_{0,n}(k_0)$, which can be obtained from the unit cell simulation with periodic boundary conditions.

## 3.3 Simulation results

### Methods

The proposed multi-frequency co-optimization method exemplifies the spontaneous four-wave mixing process shown in Fig. 3.3(a), where a single port is used to couple the pump (generated) photons to (from) the cavity. In the forward process, the fundamental mode at frequency $\omega_p$ is injected from the waveguide into the cavity, exciting the electric field distribution noted as $E_p$ in Fig. 3.3(a). Owing to the presence of nonlinearity, vacuum fluctuations create dipole sources at other frequencies, specifically, signal and idler, shown as $J_s$ and $J_i$. The generated photons in the spontaneous four-wave mixing process are designed to be collected back to the same waveguide. The collection efficiency can be represented as a mode-matching integral between the collective radiation field generated by dipoles $E_s(E_i)$ and the waveguide mode at signal and idler frequencies $E_{m,s}(E_{m,i})$. Such nonlinear photon pair generation process can be approximated by the adjoint process shown in Fig. 3.3(b), where the adjoint sources $J_s', J_i'$, i.e., the fundamental mode of the waveguide at signal and idler frequencies $\omega_s$ and $\omega_i$, are reversely propagated back into the cavity. The figure of merit can be represented in terms of the effective phase-matching integral as:

$$FoM = \left|\int_{cav} \chi^{(3)}(r)\beta(r)dr\right|^2, \beta(r) = E_p^2(\omega_p, r)E_s'(\omega_s, r)E_i'(\omega_i, r) \tag{3.20}$$

where $\beta(r)$ is the effective phase-matching integrand, $\chi^{(3)}$ is the third-order susceptibility of the material, $E_p$ is the field distribution at pump frequency, while $E_s'$ and $E_i'$ are

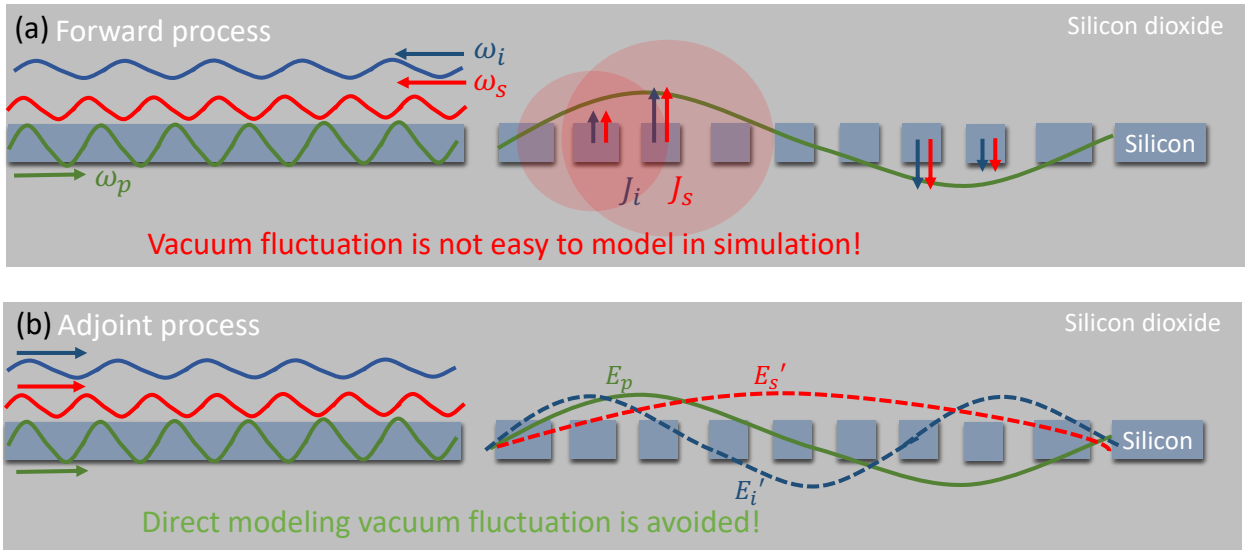


Figure 3.3: **Forward and adjoint process for the spontaneous four-wave mixing process.** (a) The pump is injected as the fundamental mode of the waveguide, exciting dipoles of signal and idler frequencies $(J_s, J_i)$ due to vacuum fluctuations. The radiation fields $(E_s, E_i)$ of the dipoles are collected back into the waveguide. (b) In the adjoint process, pump, signal, and idler modes are injected into the waveguide and the phase matching of fields $(E_p, E_s', E_i')$ inside the cavity is calculated and optimized. In this case, direct modeling of vacuum functions is avoided.

adjoint fields at signal and idler frequencies under continuous-wave (CW) excitation from the coupling waveguide. The integral is carried out over the cavity region.

The proposed figure of merit can be interpreted as follows. First, the pump, signal, and idler frequencies $(\omega_p, \omega_s, \omega_i)$ in Eq. (3.20) can be selected in the CW-simulation to satisfy the energy conservation $\omega_s + \omega_i = 2\omega_p$. Second, the figure of merit uses the non-normalized electric fields $(E_p, E_s, E_i)$, each obtained from a source excitation with fixed amplitude. The non-normalized field captures the cavity enhancement of the field intensities at the three frequencies, which also includes the coupling between the waveguide and the cavity for an efficient collection of the generated photons. In addition, with the overlap integral, the in-cavity phase-matching will be satisfied after the optimization to ensure the constructive interference of the generated photons. The proposed method provides a feasible way to optimize the photon-pair generation rate with linear solvers. The existing methods [66] may not be easily generalized to spontaneous photon pair generation due to the challenge of direct modeling of vacuum fluctuations in simulations. To address this issue, our approach uses a physics-informed source configuration based on the adjoint method, which eliminates the difficulty in modeling vacuum fluctuations and avoids arbitrariness in choosing excitation sources. In addition, the coupling from/to the waveguide is naturally included in simulations,

which is also critical for enhancing the total generation efficiency.

## Optimization Process and Results

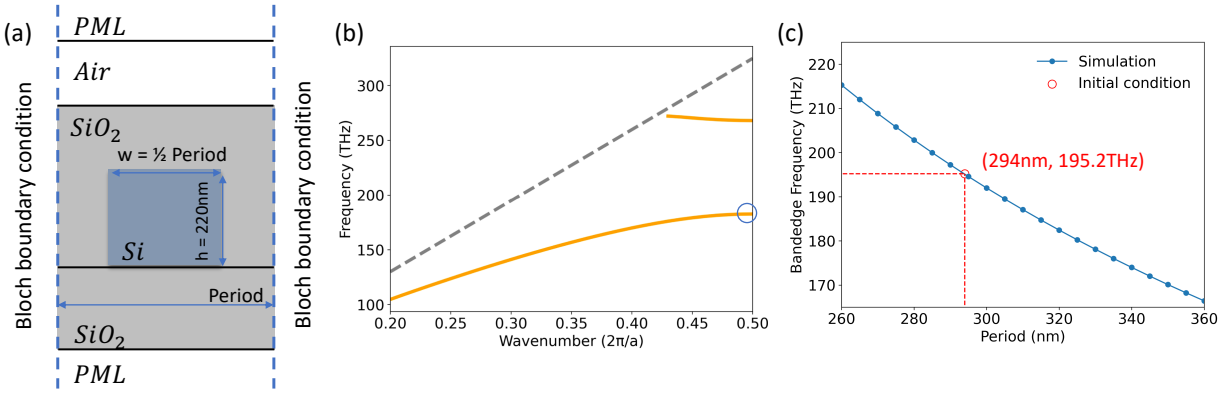


Figure 3.4: **Bandedge frequencies with different grating periods.** (a) The configuration used in the simulation of bandedge frequency. (b) An example of band diagram and the bandedge is marked by the circle. (c) Simulation results of bandedge frequencies at different periods of a grating structure with a fixed filling ratio of 0.5. The period of initial condition is selected based on the target working frequency.

We adopt the hierarchical inverse design strategy, a two-step approach that proposes an initial physics-based guess, followed by a shape optimization using the adjoint method [76]. Such a strategy minimizes the computational cost by avoiding a large number of random guesses for initial conditions, and the fabrication limits can be easily enforced by adding simple shape constraints.

As a first step, we introduce the procedure to choose the physics-based initial condition before optimization. To enhance the spontaneous four-wave mixing, it would be convenient to start with a periodic grating (1D photonic crystal) and use the resonances near the band edge. We consider a periodic system with the configuration shown in Fig. 3.4(a). For simplicity, we choose the filling ratio to be 0.5, i.e., the grating width is half of the period. The period of the initial grating is determined by a parametric sweep to search for a band edge frequency near the target frequency, as shown in Fig. 3.4(c). We choose the number of periods as N = 35, which depends on the footprint of the device and the frequency difference between the three modes. It is worth mentioning that the parameters (periods, filling ratio, number of gratings) don't have to be precisely engineered. The convergence to target frequencies with high-quality factor resonances is achieved over iterations. Compared with the large number of random trials for initial conditions, this process is deterministic and therefore minimizes the computational cost.

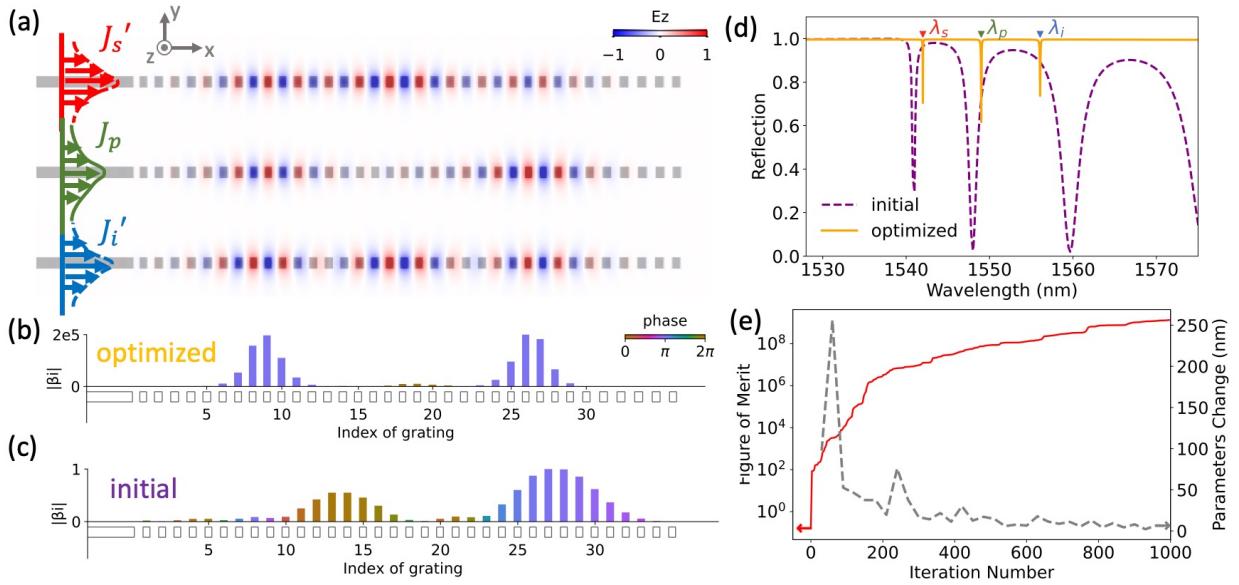


Figure 3.5: **Optimization for nonlinear photonic structure.** (a) Electric field profile ($E_z$) at the signal, pump, and idler frequencies for optimized structure, excited by fundamental modes ($J_s'$, $J_p$, $J_i'$) from the input waveguide. (b-c) Illustration of the phase-matching condition. The height of the bar plot corresponds to normalized intensity, while the color indicates the phase of the phase-matching integrand, summed over each grating. The color consistency exemplifies the enhancement of phase-matching. (b) Optimized and (c) initial (periodic) grating. (d) Reflection spectra for grating before and after optimization. High-Q resonances, in alignment with target frequencies, are prominently observed. (e) The evolution of the figure of merit and parameters changes over iterations during the optimization.

Next, we perform the optimization using the width and gap of each grating, and the initial design is a periodic grating structure with the number of gratings $N = 35$, width and gap as $w = g = 147$nm. The optimized grating structure is simulated to have three energy-matching resonant modes shown in Fig. 3.5(a). During the optimization, the fundamental TE mode is injected into the waveguide at the pump wavelength $\lambda_p = 1549$nm, and the field distribution $E_p$ is computed by the 2D FDFD solver of `EMopt`. The fundamental modes at signal and idler frequencies $(E_s', E_i')$ are excited by adjoint source $(J_s', J_i')$, also injected from the waveguide, at $\lambda_s = 1542$nm and $\lambda_i = 1556$nm, respectively. The cavity enhancement of the fields can be visualized from the contrast of the field inside the cavity compared to that in the incident waveguide. The phase-matching integrand $\beta(r)$ in Eq. (3.20) is visualized as the bar plot in Fig. 3.5 (b) and (c) for each grating. The heights of the bars stand for the amplitudes and the color for the phases. The field enhancement of five orders of magnitude is shown on the normalization of the y-axis after optimization. In the ideal case

where all grating pitches are excited and contribute constructively to the photon generation, the phase (i.e., color) should be identical. Compared with the phase-matching plot for the initial period grating in Fig. 3.5(c), the phase-matching condition is greatly enhanced as the phase difference is minimized. The resonant frequencies of the modes can be probed as minima in the reflection spectrum, shown in Fig. 3.5(d). Initially, the resonances are not equally spaced, the quality factors are not high enough, and the phase-matching condition is not satisfied. After optimization, the three resonances are equally spaced in frequency, with sharper peaks in reflection due to the improved quality factors. The optimization uses the limited-memory BFGS (L-BFGS) algorithm [77] with hard constraints on the minimum width and gap to be larger than 110nm. The convergence of parameters can be observed from Fig. 3.5(e), with negligible parameters' change after approximately 600 iterations, and the increment of the figure of merit is also shown.

In our implementation, we use the 2D FDFD solver in `EMopt`. The total simulation domain size is 15$\mu$m by 2$\mu$m with symmetric boundary conditions at the bottom and perfect matching layer on other sides. The simulation resolution is 20nm. The optimization takes approximately 5 hours for 1000 iterations on a desktop with two 24-core central processing units (AMD EPYC Rome 7352). We start with a periodic grating with 147nm for both width and gap. The optimized parameters after 720 iterations are converged to the following table, with a minimum width and gap size of 138.1nm and 119.9nm, respectively, which is suitable for both in-house and foundry fabrication. The optimized parameters are listed in Table 3.1.

Table 3.1: **Parameters for optimized devices**

| **Index** | **1** | **2** | **3** | **4** | **5** | **6** | **7** | **8** | **9** | **10** | **11** | **12** |
|---|---|---|---|---|---|---|---|---|---|---|---|---|
| **Gap (nm)** | 119.9 | 140.1 | 145.2 | 147.9 | 143.7 | 141.0 | 141.4 | 135.5 | 132.4 | 135.1 | 139.6 | 142.3 |
| **Width (nm)** | 147.9 | 166.0 | 169.0 | 170.4 | 168.4 | 160.3 | 151.5 | 145.6 | 145.0 | 148.6 | 154.5 | 159.0 |
| **Index** | **13** | **14** | **15** | **16** | **17** | **18** | **19** | **20** | **21** | **22** | **23** | **24** |
| **Gap (nm)** | 141.4 | 141.2 | 142.5 | 143.9 | 139.3 | 137.5 | 137.3 | 147.7 | 151.2 | 153.5 | 151.8 | 151.4 |
| **Width (nm)** | 159.8 | 157.3 | 152.1 | 147.8 | 144.5 | 145.4 | 147.1 | 150.6 | 154.1 | 157.0 | 155.8 | 150.8 |
| **Index** | **25** | **26** | **27** | **28** | **29** | **30** | **31** | **32** | **33** | **34** | **35** | |
| **Gap (nm)** | 148.5 | 144.4 | 143.0 | 146.5 | 148.7 | 155.7 | 163.3 | 166.4 | 168.7 | 165.4 | 159.7 | |
| **Width (nm)** | 145.8 | 138.8 | 138.1 | 143.5 | 151.8 | 163.5 | 171.4 | 175.3 | 177.5 | 171.9 | 160.1 | |

## 3.4 Experimental results

### Fabrication Details

The devices were fabricated using silicon-on-insulator (SOI) wafers. The SOI wafer stack comprises 220 nm crystalline silicon and a 3 µm buried thermal oxide layer on a thick (725

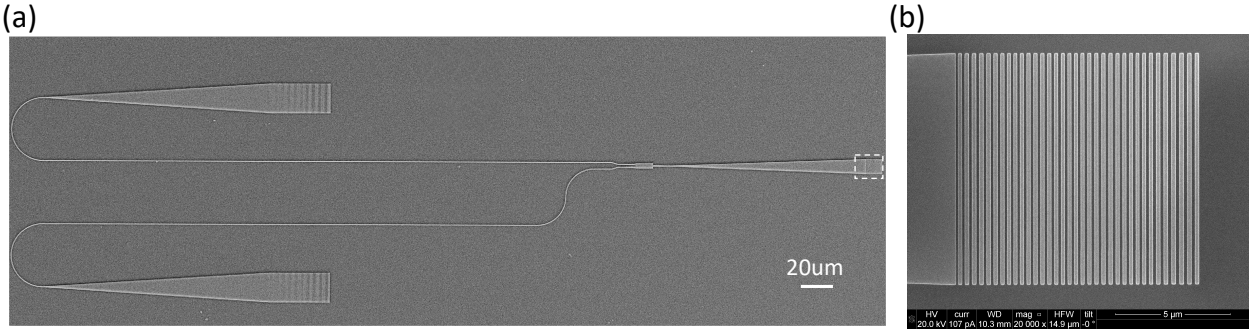


Figure 3.6: **SEM images of the fabricated device.** (a) Top view of the device. (b) Zoomed-in view of the inverse-designed cavity.

µm) silicon handle layer. The fabrication starts with spin-coating negative e-beam resist (HSQ) on an RCA-cleaned SOI chip, followed by electron beam lithography and development. Next, an inductively coupled plasma dry etching process was utilized to finish defining patterns on the chip. Finally, a one-micron thick $SiO_2$ cladding layer is deposited by the Plasma-enhanced chemical vapor deposition (PECVD) method.

The SEM images of the device before depositing the cladding layer are shown in Fig. 3.6. For simplicity in both simulation and fabrication, we choose the transverse length of 10 µm (y-direction in the SEM). Because the length is much longer than the wavelength, we can approximate the 3D structure with 2D cross-section simulation. In addition, the resonances would also be less affected by dimension offset caused by the fabrication imperfection in the transverse direction. As shown in Fig.3.6(a), the device consists of a pair of grating couplers (for input and output), waveguide, MMI-based beam splitter, taper, and the inverse-designed cavity from the left to the right. A zoomed-in view of the cavity is shown in Fig. 3.6(b).

## Experimental setup

The experiment setup is presented in Fig. 3.7. The inverse-designed devices were pumped by a high-power, continuously tunable laser (CTL) in C-band for nonlinear photon pair generation, or by the tunable laser from the optical spectrum analyzer (OSA) after amplification for linear reflection measurement. The light source is coupled to the chip through a four-channel fiber array with grating couplers and an integrated Y-splitter. The output light passed through a 50:50 broadband fiber beam splitter to the pump and idler channels or can be routed directly to the OSA for reflection spectrum characterization. To filter out the pump light, two (four in total) narrowband, tunable fiber filters (60dB High Isolation Manual Tunable Filter, Dicon Inc.) were cascaded, and centered at signal and idler wavelength in each channel. Each filter has an extinction ratio of around 60dB, which provides 120dB for each channel. The signal and idler photons were detected using fiber-coupled superconducting nanowire single-photon detectors (SNSPD), and coincidence histograms were measured

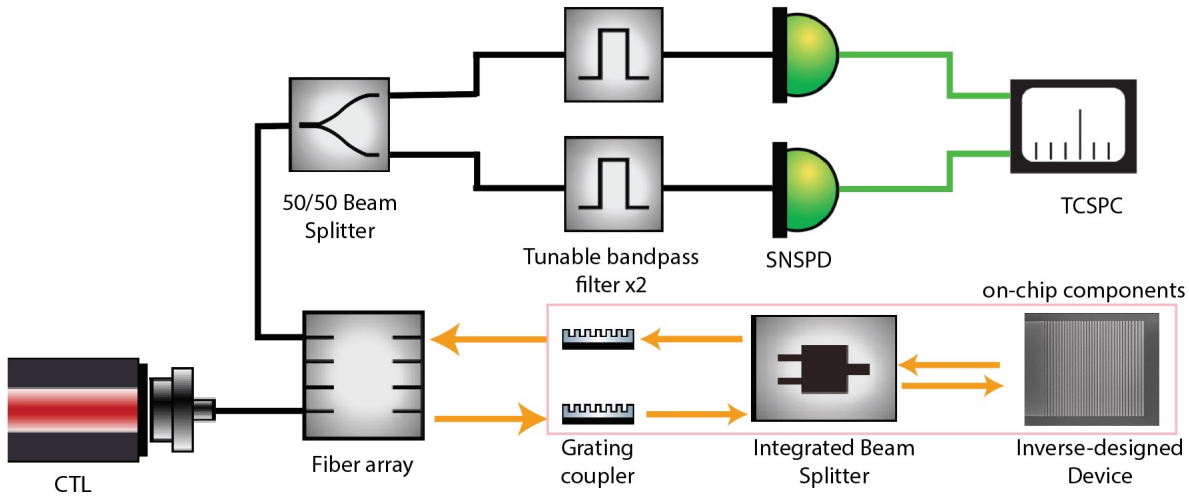


Figure 3.7: **Diagram of the measurement setup used in the photon pair generation experiment.** (CTL: continuously tunable laser, SNSPD: superconducting nanowire single photon detectors, TCSPC: time-correlated single-photon counting) Black line: fiber optical path. Orange line: free-space and on-chip optical path. Green line: electrical signal path. Dashed line: transmission-resolved path.

using a two-channel time-correlated single-photon counting (TCSPC). The camera image of the experimental setup is shown in Fig. 3.8. The SNSPD and TCSPC are not shown in the image.

## Experimental Results and Analysis

The reflection spectrum of the inverse-designed device is measured by an optical spectrum analyzer in the linear regime, and the minima in reflection are extracted and fitted to obtain the loaded quality factor of pump, signal, and idler frequencies [Fig. 3.9(a)]. The measured wavelengths of resonances are $\lambda_s = 1551.3nm$, $\lambda_p = 1558.1nm$, and $\lambda_i = 1564.8nm$, which are shifted by approximately $9nm$ compared to simulation results. The shift is mainly due to fabrication imperfections and can be calibrated by thermal tuning as experimentally shown in Section3.5. To confirm the field profile, the device is excited at resonance frequencies from a continuous wave laser source, and the scattered light is captured with an infrared camera as shown in Fig. 3.9(b). The obtained image is compared with the simulation, where the field is monitored $1\mu$m above the device plane with Fourier components collected within the numerical aperture of the objective lens ($NA = 0.26$). The agreement between simulation and experiment confirms that the field distributions are optimized for phase-matching. Next, the nonlinear experiment characterizes the paired photon generation efficiency. The CW-laser is tuned to the pump wavelength, and the output power at signal frequency is monitored at

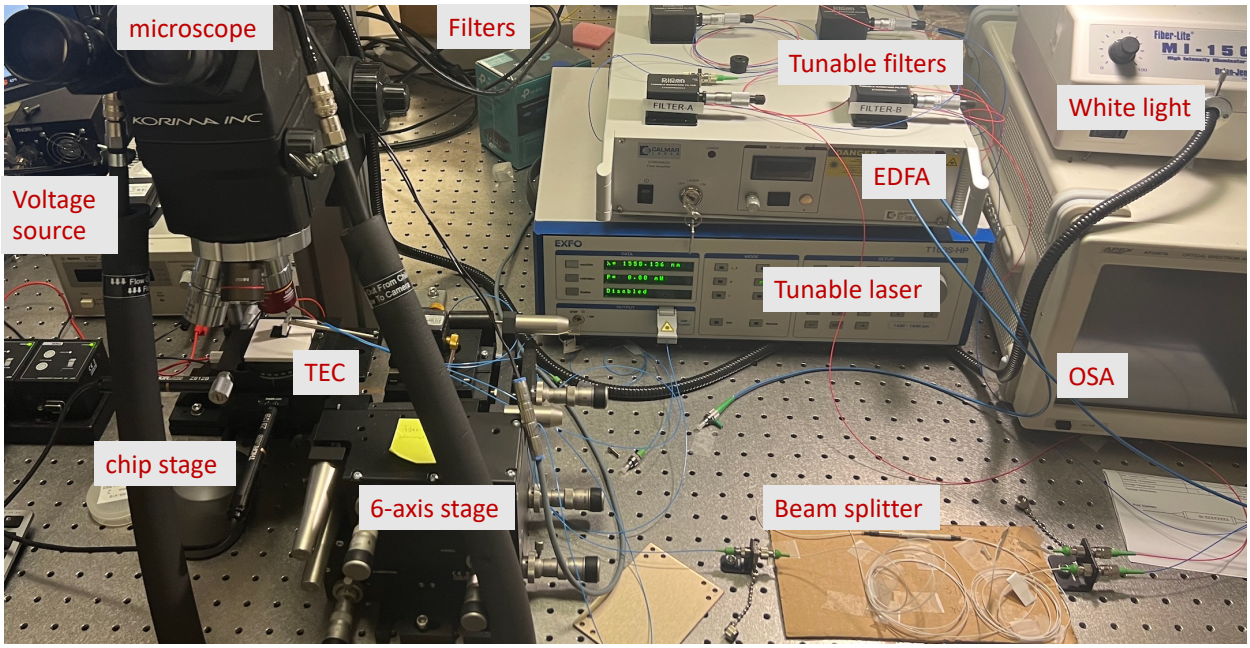


Figure 3.8: **Camera image of the experimental setup.**

different input power levels, shown in Fig. 3.9(c). The output power is proportional to the pump power squared, as expected for a degenerated spontaneous process before other nonlinear effects, such as free carrier or two-photon absorption, show up at around 15mW [78]. The quantum nature of photon-pair is confirmed by the intensity correlation measurement $g^{(2)}$ in Fig. 3.9(d), where the peak in the correlation indicates the photon pairs are generated simultaneously.

| Parameters | $\mu$(ns) | $\sigma$ (ns) | $c_0$ (counts) | $y_0$(counts) |
|---|---|---|---|---|
| Values | 1.382 | 0.02370 | 289.0 | 2.6 |

Table 3.2: **Fitting parameters in CAR measurements of Fig. 3.9(d).**

To quantify the generation rate and the coincidence-to-accidental ratio (i.e., the signal to noise ratio of the entangled photon source), the measured coincident count histogram is fitted with a Gaussian function as $y = c_0 \exp\left(\frac{-(x-\mu)^2}{2\sigma^2}\right) + y_0$ , where $\mu$ is the averaged delay time between signal and idler channel, $\sigma$ is the standard deviation, $c_0$ is the peak counts and $y_0$ is an estimation of averaged noise. The fitted parameters are shown in Table. 3.2. The coincidence to accidental ratio is obtained from the fitted Gaussian curve as 162 and a maximum on-chip generation rate is 1.1MHz at an on-chip pump power 0.78mW after compensating for the loss. In the experiment, the signal and idler photons are filtered out

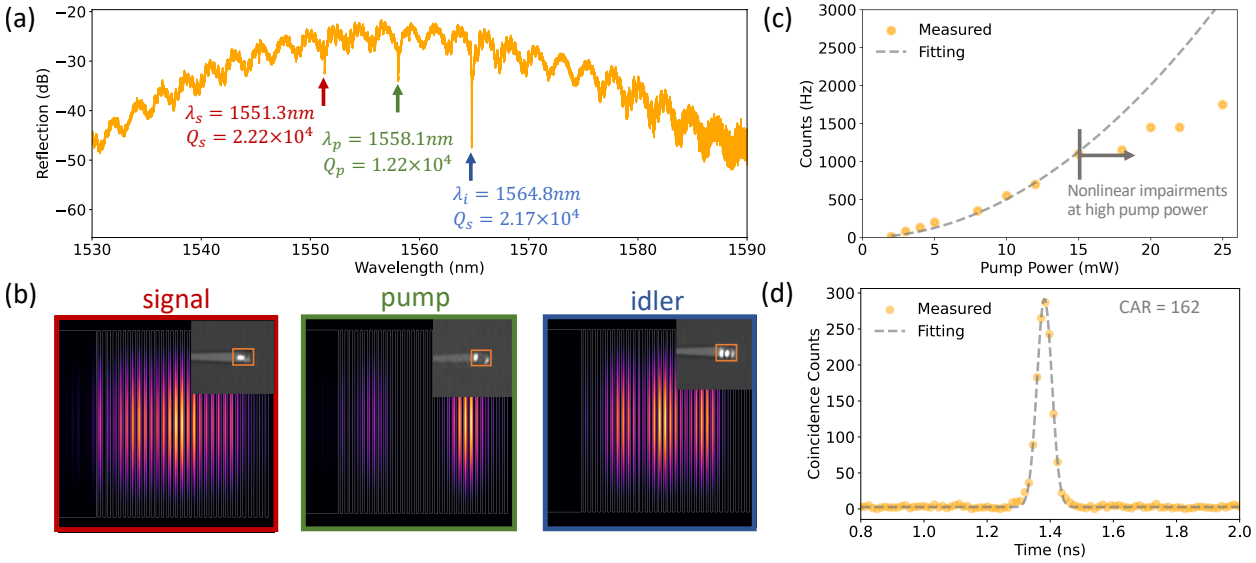


Figure 3.9: **Measurement results of the inverse-designed device.** (a) The reflection spectrum of the fabricated device clearly shows three distinct resonances for pump, signal, and idler frequencies, with their corresponding quality factors obtained by fitting. (b) Simulated scattered light captured by the objective lens monitored above the device and the observed camera images. (c) Light-light relationship for the spontaneous four-wave mixing process, with the collected data points aligning with the square-law fitting. The reduction of generation rate at high pump power is due to the appearance of other nonlinear effects. (d) Measured coincidence counts for signal and idler channels integrated over 10 minutes.

with cascaded narrowband tunable filters, with 120dB extinction ratio for each channel. The measured 3dB bandwidth for cascaded filters is $1.03nm$ centered at signal wavelength ($1551.3nm$) and $0.87nm$ centered at idler wavelength ($1564.8nm$), which is used for the recorded counts shown in Fig. 3.9 (c, d).

## 3.5 Discussion

### Interpretation of Optimized Structure

The proposed cavity device can be seen as a quasi-one-dimensional photonic crystal with small perturbations. In that sense, our inverse design strategy can be understood as optimizing the perturbation and consequent mode field profiles to achieve maximal overlap integral while keeping the resonant frequencies equally spaced. Each mode field profile can be written as a product of the band edge mode $u(x)$ and a slowly varying envelope function $F(x)$; $E(x) = u(x)F(x)$. The envelope of a resonance mode $F(x)$ in a perturbed photonic

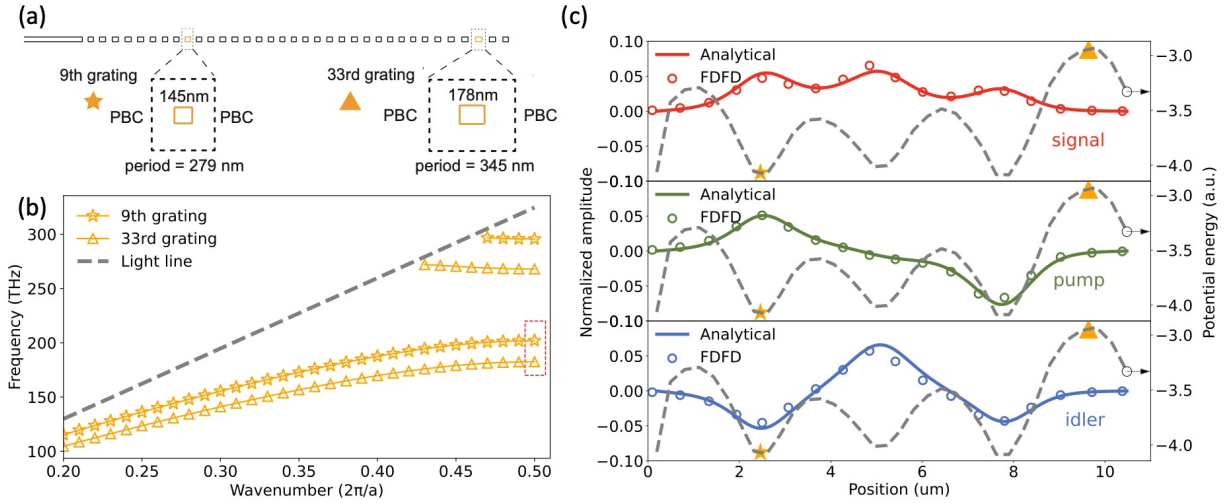


Figure 3.10: **Interpretation of inverse designed cavity in the envelope function picture.** (a) Cavity comprising perturbed gratings after optimization. Two example gratings with different periods are shown to calculate the band edge frequencies by applying periodic boundary conditions (PBCs) on left and right, and perfect matching layer (PML) at top and bottom. (b) Band diagram for the two selected gratings, where valence band edge frequencies are extracted. (c) The envelope functions (solid lines) of the three lowest modes in the effective potential landscape (dashed grey line) of the inverse-designed cavity. The amplitudes extracted from field profiles of FDFD simulation (circles) agree with the envelope function.

crystal approximately follows the Wannier-like equation[79, 75],

$$-\left[\frac{1}{2m}\frac{\partial^2}{\partial x^2}+V_{\text{eff}}(x)\right]F(x)=\omega^2 F(x) \tag{3.21}$$

where $m$, $V_{\text{eff}}$ and $\omega$ are the effective mass, effective potential, and the resonance frequency of the mode, respectively. The effective mass $m$ is defined by $m^{-1}\equiv\partial^2\omega_0/\partial k^2$ in analogy with that of electrons in solids, where $\omega_0$ is the photonic band frequency of the unperturbed photonic crystal. The effective local potential $V_{eff}$ can be extracted by simulating each grating with periodic boundary conditions (PBC). Two unit-cells with relatively small (star marker) and large (triangle marker) periods are highlighted as examples. The valence band edge frequencies are calculated using finite-element simulation, shown as the dashed box in Fig. 3.10(b). The calculation is performed over each of the gratings, and the obtained 1D effective potential is shown as dashed grey lines in Fig. 3.10(c), as the square of the valence band edge frequencies. The envelope function solutions for Eq. (3.21) are plotted in Fig. 3.10(c). The envelopes show good agreement with the fields extracted from the FDFD solver in `EMopt`. Interestingly, the effective potential has three wells in the middle

of the cavity region and a high wall near the right end. Therefore, the inverse-designed cavity can be interpreted as a three-coupled-resonator system between a highly reflective mirror on the right and an output coupler on the left. Compared with a single cavity case, the coupled-resonator configuration provides more degrees of freedom to adjust the optical mode shapes and, thus, a larger nonlinear overlap integral. In addition, our design method allows the device to have a smaller footprint for a given target resonance frequency, which is also advantageous for stronger light confinement.

## Robustness Evaluation

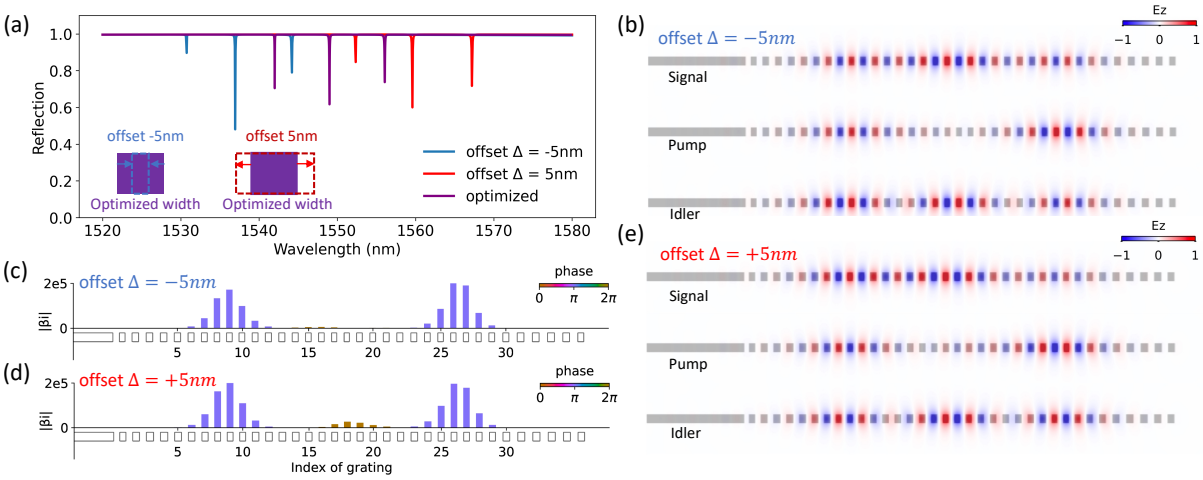


Figure 3.11: **Robustness of the inverse-designed device.** (a) Spectra for optimized structure with uniform dimension offset (over/under etching) +/- 5nm. Inset: illustration of dimension offset. (b) Field profiles for offset = -5nm and (e) offset = 5nm. The field profiles are similar to Fig. 3.5(a). (c,d) Visualization of the phase-matching condition in the cavity with dimension offset.

The robustness of our inverse-designed structure to fabrication imperfection stems from the simplicity of the proposed grating-like structure. Uniform deviation from nominal dimensions by a few nanometers, typically caused by over/under etching, are commonly observed in practice [80]. Here, we show in simulation that uniform dimension offset by +/-5nm, similar to the estimated fabrication error, will only lead to a shift of the spectrum without significantly modifying the field profiles or phase-matching conditions (Fig. 3.11). In Fig. 3.11(a), the reflection spectra with uniform grating width shift of +/-5nm is plotted. The three resonances (pump, signal, idler) remain of high quality factors as can be seen from the reflection spectra despite a shift in wavelength. In Fig. 3.11 (b,e), we observe that the field profiles after dimension offset are also similar to the original fields shown in Fig. 3.5(a). As a consequence, the phase-matching condition inside the cavity across three wavelengths

is also preserved, which is visualized in Fig. 3.11(c,d), where the colors, i.e., phase of the intergrand, are consistent across different gratings. We would like to highlight that the robustness can also be understood based on our interpretation of the structure in Fig. 3.10. The dimension shift changes the effective potential in the Wannier equation by effectively adding a constant potential, but will not change the shape of wavefunction nor the effective phase-match conditions.

## Thermal Tuning Impacts

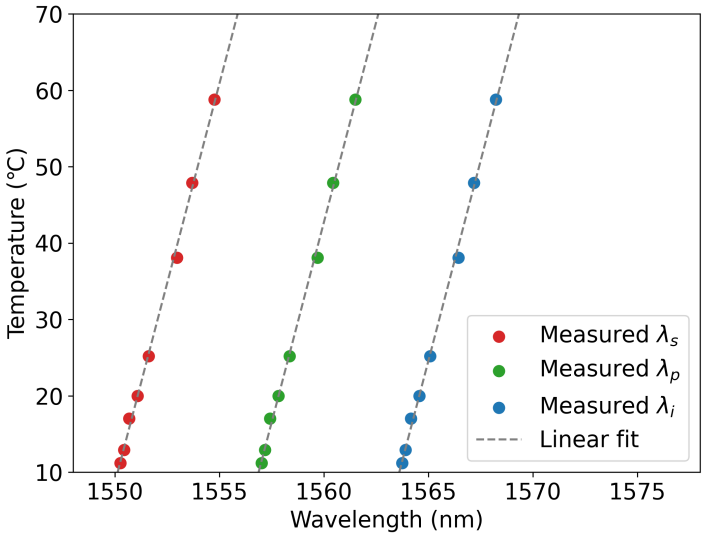


Figure 3.12: **Thermo-tuning of the working wavelength of the device.** The sample is placed on top of a thermo-electric cooling pad with the voltage changed from -1V to 1V. The resonance wavelengths are extracted from the measured reflection spectra.

In practical applications of an entangled quantum light source, it is critical to match specific emission wavelengths for signal and idler photons. In the measurement results (Fig. 3.9(a)), we observe a shift (approximately 9nm) of the resonant wavelengths compared to those in the simulation. The shift can be caused by the fabrication imperfection. As shown in the previous section, we suggest that the observed shift can originate from a uniform dimension offset in the grating widths. To compensate for such wavelength shifts, active tuning mechanisms can be used to achieve the target wavelength. As an example, we demonstrate a thermal tuning method, by placing the chip on top of a thermo-electric cooling pad for temperature control. As shown in Fig. 3.12, with an applied voltage from -1V to 1V, the temperature of the chip varies by around $50°C$, measured by an infrared thermometer with

an accuracy of $\pm 1.5°C$. The resonances are shifted by approximately 4.5nm due to the temperature change. Therefore, by depositing a metallic heater on top of the device, active tuning of the wavelengths of signal and idler photons can be achieved and the target wavelengths can be reached.

## Estimate the on-chip generation rate

The generation rate in the experiment is calculated by fitting the intensity correlation measurement $g^{(2)}$ results as shown in Table 3.2. The "off-chip" generation rate, directly measured, is influenced by losses from the device to the Superconducting Nanowire Single-Photon Detector (SNSPD) and the efficiency of the SNSPD. Such coupling loss and instrument efficiency can be improved and are not fundamental to the device's performance. Hence, calculating the "on-chip" generation rate, which normalizes measured efficiency $\eta$ to account for coupling losses and instrument efficiency, provides a more intrinsic evaluation of the device performance. Given a measured generation rate $R_{measured}$, the on-chip generation rate is

$$R_{on-chip} = R_{measured}/\eta_s\eta_i \tag{3.22}$$

Here, $\eta_s$ and $\eta_i$ are the collection efficiency for signal and idler photons, respectively. In this analysis, it's assumed that the collection efficiencies for signal and idler photons are independent events, i.e., the loss of a signal photon does not influence the loss of an idler photon. Therefore the collection efficiency of the coincident counts is simply a multiplication of $\eta_s$ and $\eta_i$. In certain studies, the on-chip generation rate is expressed as a function of single-channel generation rates for signal and idler photons:

$$R_{on-chip} = R_sR_i/R_{measured} \tag{3.23}$$

where $R_s$ and $R_i$ are single-channel count rates for signal and idler.

## Comparison with Prior Work

We compared our inverse-designed device to previous works with silicon micro-ring resonators in the following aspects:

1. Flexibility: One advantage of our method is that it is highly flexible and customizable. While the ring structure can satisfy the phase-matching condition for four-wave mixing process, our approach can be used for other nonlinear processes, such as second/third harmonic generation, spontaneous parametric down conversion, and non-degenerated four-wave mixing with arbitrary frequency combinations, where micro-ring resonators may not be applicable. Besides, the wavelength difference between the signal and idler frequencies, for example, is also customizable by optimization process. On the contrary, the wavelength difference (Free Spectral Range) is determined by the radius of the micro-ring, hence a decrease in FSR by a factor $1/\alpha$ requires the radius to increase by $\alpha$, and footprint by $\alpha^2$. The inverse-designed device has no such constraints in scaling.

| Year | Ref. | Footprint ($\mu$m$^2$) | PGR (kHz) | Avg pump ($\mu W$) | CAR |
|---|---|---|---|---|---|
| 2009 | Clemmen et al. | 154 | 300 | 400 | 30 |
| 2012 | Azzini et al. | 79 | 200 | 200 | 250 |
| 2013 | Engin et al. | 380 | 132 | 1000 | 37 |
| 2014 | Harris et al. | 707 | 600 | 300 | 50 |
| 2014 | Guo et al. | 1,385 | 14 | 100 | 180 |
| 2015 | Silverstone et al. | 707 | 4,600 | 150 | 10 |
| 2015 | Grassani et al. | 314 | 400 | 250 | 132 |
| 2015 | Wakabayashi et al. | 154 | 21,000 | 410 | 352 |
| 2015 | Gentry et al. | 1,520 | 29 | 50 | 55 |
| 2015 | Steidle et al. | 1,134 | 60 | 200 | 1984 |
| 2016 | Savanier et al. | 314 | 83 | 79 | 65 |
| 2017 | Ma et al. | 314 | 16 | 7.4 | 12000 |
| 2017 | Fujiwara et al. | 314 | 10,000 | 500 | 350 |
| 2023 | **This work** | 100 | 1,100 | 780 | 162 |

Table 3.3: **Previous works on spontaneous four-wave mixing using silicon micro-ring resonator [46].**

2. Footprint: For simplicity in simulation and fabrication, we demonstrated a proof-of-concept device with a footprint of $10.56um$ by $10um$, by choosing the transverse length of each grating to be 10um. Because the length (10um) is much longer than the wavelength, we approximated the 3D grating with a 2D cross-section simulation (assuming length is infinity), which is more computationally efficient. With additional computational resources, we can abandon such approximation and directly perform 3D simulation and optimization. In that case, we estimate that the footprint of inverse-designed cavity can be reduced to 10um×1um, which can be very helpful for large-scale integration of entangled photon pair sources. On the other hand, in previous research, the smallest micro-ring resonator with decent quality factor has a radius of 5um, which leads to a footprint of $\pi r^2 = 79\mu m^2$. This footprint can hardly get improved, because smaller ring radius leads to more loss, which lowers the quality factor and reduces the generation rate. In sum, it is very challenging to further reduce the footprint of the micro-ring structure, while the inverse-designed structure can be order of magnitude smaller with 3D optimization.

3. Generation rate/efficiency: While the demonstrated generation rate and efficiency of the inverse-designed devices is smaller than some state-of-the-art micro-ring structures, we would like to emphasize that majority of the recent publication in micro-ring involves active modulation, while our device is passive and single-etched. The generation rate of the inverse-designed devices can be improved with similar techniques. In addition, with 3D simulation/optimization, higher quality factor can be achieved, which can also improve the

generation rate/efficiency.

Therefore, our proposed method featured high flexibility, small footprint compared to the micro-ring platform. The current generation efficiency can be improved by adopting active tuning methods to compensate the spectra misalignment, and using full 3D optimization.

## 3.6 Conclusion

In summary, we propose an inverse design method with interpretable results to enhance the efficiency of on-chip photon generation rate through nonlinear processes by controlling the effective phase-matching conditions. We fabricate and characterize a compact, inverse-designed device using a silicon-on-insulator platform that allows a spontaneous four-wave mixing process to generate photon pairs at 1.1MHz with a coincidence to accidental ratio of 162. Our design method accounts for fabrication constraints and can be used for scalable quantum light sources in large-scale communication and computing applications.

# Chapter 4

# Increasing bandwidth: mode-division multiplexing for optical computing

## 4.1 Introduction

As conventional electronic computing approaches its performance limits, photonic-based computing emerges as a promising alternative, offering potential reductions in energy consumption, enhanced bandwidth, and decreased latency. Therefore, there has been a lot of effort and interest in developing the next generation of computing platforms based on the photonic computing [81, 82, 83, 84, 85, 86, 87, 88, 89, 90, 91, 92, 93]. A critical concern for any novel computing platform is scalability, encompassing factors like power consumption, operational speed, and signal-to-noise ratio. Two integrated platforms for optical neural networks have caught a lot of attention recently. One is the coherent nanophotonic circuit based on Mach-Zender interferometers [94], and the other is the wavelength-division multiplexing (WDM)-based neural network with micro-ring modulators [95]. Recent work has shown that both platform shares similar scaling law despite the different nature of the systems [96]. While the WDM approach with micro-ring modulators has the potential to enable low-latency optical computing, the integration of multi-wavelength laser sources can be challenging. Although the development of on-chip frequency combs presents a potential solution [97, 98, 99, 100, 88], the total bandwidth is inherently constrained by the number of combs fitting within the micro-ring modulator's free-spectral range. It has been shown that the packing wavelength crossing below 100 GHz can lead to cross-talk [101]. Recently, 32 channels WDM have been implemented [88], however, it is still insufficient for modern neural network architectures. For example, a simple feed-forward neural network for the MNIST dataset (28 by 28 pixels) has an input layer of 784 units [102]. To address the bottleneck of bandwidth issue, an MDM-WDM approach has been demonstrated to be a promising way to increase the bandwidth of optical communication[103, 104, 105]. In this work, we propose and demonstrate the integration of mode-division multiplexing (MDM) as a novel dimension for enhancing optical computing capabilities. We demonstrate a mode-division multiplexing

neural network and validate the signal and crosstalk fabricated by AIM Photonics Multi-Project Wafer (MPW) [106]. We show that such a mechanism can increase the input vector size, and, more importantly, it is compatible with existing wavelength-division multiplexed neural networks for increasing the dimension of matrix multiplication.

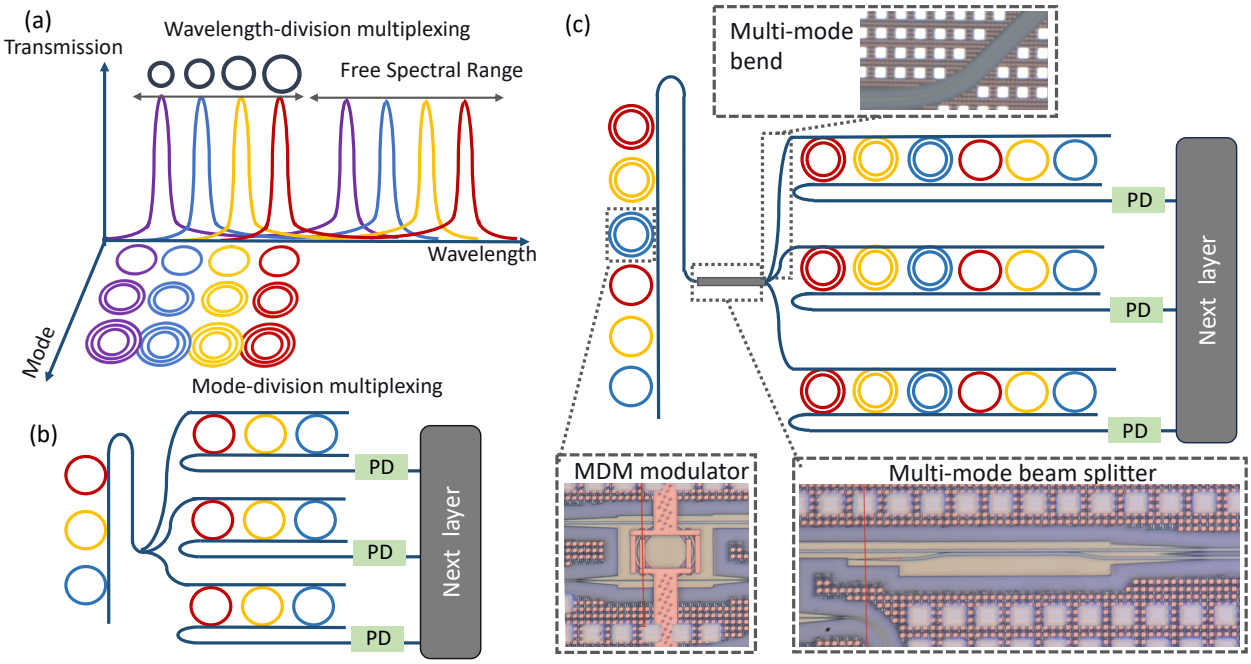


Figure 4.1: **Architecture of MDM-WDM optical neural network.** (a) Schematics of multi-dimensional optical computing using both wavelength-division multiplexing and mode-division multiplexing. The matrix multiplication is limited by the number of wavelengths within one free-spectral range in a conventional WDM-based optical neural network system. (b) WDM-based optical neural network and (c) WDM-MDM-based optical neural network. Concentrical circles indicate micro-ring modulators for high-order modes. Inset: Microscope images of the MDM micro-ring modulator, multi-mode beam splitter, and low-loss multi-mode waveguide bend fabricated in AIM Photonics foundry.

## 4.2 Design architecture

We propose multi-dimensional optical neural network architecture as shown in Fig. 4.1. In traditional optical neural networks utilizing micro-ring modulators, the channel count is constrained by the number of wavelengths that fit within a single free spectral range. In Fig. 4.1(a), MDM introduces an additional degree of freedom, alongside wavelength, to create more orthogonal channels, thereby expanding the capacity for optical computing. The con-

centric rings represent micro-ring modulators for high-order modes. While the conventional neural network allows an optical matrix-vector multiplication for an input vector of dimension $N$, which is encoded in different wavelengths shown in Fig. 4.1(b), MDM-WDM-based neural network enables a much larger matrix operator of dimension $MN$, where $M$ is the number of modes available. The example here has $N = 3$ and $M = 2$. Implementing this high-dimensional optical computing system necessitates the design and optimization of three crucial components: a modulator for high-order modes, a multi-mode beam splitter, and a multi-mode waveguide bend (Fig. 4.1(c)). The multi-mode beam splitter is needed to distribute the intensity of each mode equally into the row of the multiplication matrix, and the multi-mode waveguide is crucial for minimizing the scattering loss, especially for high-order modes. The microscope images for corresponding fabricated components are shown in the zoomed-in views of Fig. 4.1(c).

## 4.3 Component-level: simulation and experimental results

To demonstrate the proposed mode-division multiplexed neural network, we designed and simulated the three key components of a multi-mode system.

### Photoconductive modulator

We start with the simulation and experimental results of the photoconductive modulator for high-order modes. The designed photoconductive micro-ring modulator precisely controls the coupling and conversion from the $TE_{01}$ mode to the $TE_{00}$ mode. As illustrated in Fig. 4.2(a), the designed micro-ring modulator consists of ridge-shaped waveguides to allow the doped section to conduct current for thermal tuning and calibration purposes. In the coupling region, the modulator consists of an asymmetric coupling region ($TE_{01}$ to $TE_{00}$) at the top (red box) and a symmetric coupling region ($TE_{00}$ to $TE_{00}$) at the bottom (green box). The width of the input multi-mode coupler is selected to match the effective index of high-order mode ($TE_{01}$) with the fundamental mode inside the ring, such that the $TE_{01}$ mode couples through. The multi-mode waveguide width used is 1.1 $um$, leading to a coupling efficiency of 24.2% near $1550nm$ wavelength with a coupling length of $1um$ for the straight section. The field profile with $TE_{01}$ mode input is shown in Fig. 4.2(b). We show in simulation results that only the $TE_{01}$ mode is coupled but the fundamental mode propagates through with negligible crosstalk. The symmetric coupler region at the bottom (green box) couples the fundamental mode inside the micro-ring modulator to the single-mode waveguide with a similar coupling efficiency of 23.5%. This is designed for a nearly critically coupled condition such that the input intensity can be fully used in the next stage when on resonance. The interconnect simulation of the modulator shows that an applied voltage of 1.5 $V$ leads to a wavelength shift of 2.8 $nm$, which is enough to modulate the transmission by 16.5dB (Fig. 4.2 (c)). We validate the simulated micro-ring modulator with a testing device consisting of

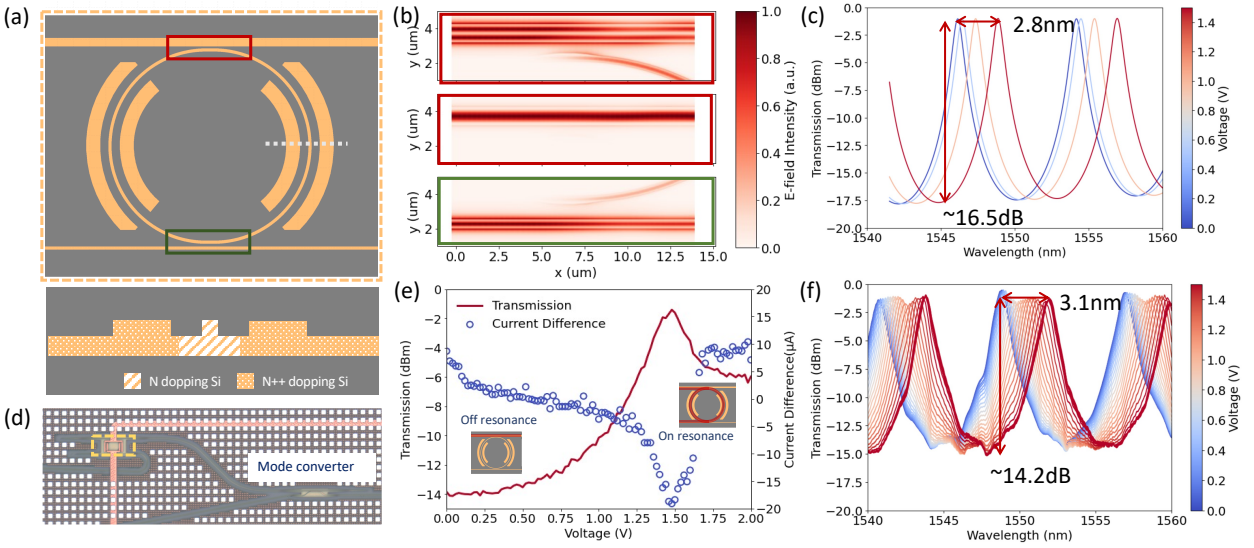


Figure 4.2: **MDM modulator simulation and measurement results.** (a) Layout of the testing structure for MDM modulator and the top view of micro-ring modulator (d), with asymmetric coupler (red box) for the $TE_{01}$-mode, and symmetric coupler (green box) for the fundamental mode. (b) Simulated intensity profiles show that the $TE_{01}$-mode couples into the micro-ring from the asymmetric coupler, while the fundamental modes ($TE_{00}$) go through with negligible coupling. The symmetric coupler has a similar coupling coefficient. (c,f) Simulation and experimental results for the thermal shift of the resonances of the micro-ring modulator. (e) Photo-conductive effect for calibration of the micro-ring modulator. The peak in transmission matches the maximum current difference between the laser on and off.

the mode converter followed by the modulator as shown in Fig. 4.2(d). The mode converter transforms the fundamental mode from the input to $TE_{01}$ at the output, which is sent to the modulator to couple back to the fundamental mode that can be directly probed through the edge coupler. A microscope image of the testing device is shown in Fig. 4.2(a). Experimental results (Fig. 4.2(f)) show an extinction ratio of $-14.2dB$, with a resonance shift of $3.1nm$ at a voltage difference of $1.5V$, which is consistent with the simulation.

One of the major challenges of scalable weight banks with a micro-ring modulator array is its calibration. Such calibration is trivial for a single heater-based resonator if the optical output can be directly measured in a feedback loop. But as the dimension of weight matrices (N) and the number of layers (M) in the neural network increase, the number of modulators increase on the order of $O(N^2M)$, hence addressing the response of each modulator optically becomes challenging. A built-in sensor for calibration with current change due to photoconductive effect was proposed in [107] and then adopted for weight banks in optical neural networks [108, 109, 110]. We introduced the photoconductive effect based calibration in the modulator for high-order modes as shown in the cross-section in Fig. 4.2(a), where the

regions on both sides of the micro-ring are N-doped and the central region of the micro-ring is lightly doped. In Fig. 4.2(e), the transmission at the drop port is maximized near applied voltage $1.5V$, where the micro-ring resonator is on resonance. The coupling of light can be directly probed in the current change by switching the laser on and off. When the laser is on and the micro-ring is on resonance, the photoconductive effect leads to a change in conductance, compared to the case where the laser is off. For verification, in Fig. 4.3, different wavelengths are used for the input laser, and the applied voltages for maximum transmission is shifted accordingly. The alignment between the maximum current difference and highest transmission at the drop port indicates that the calibration of transmission can be achieved without measuring the optical output. Therefore, the system would have a built-in calibration function to compensate the fabrication difference among different micro-ring modulator devices.

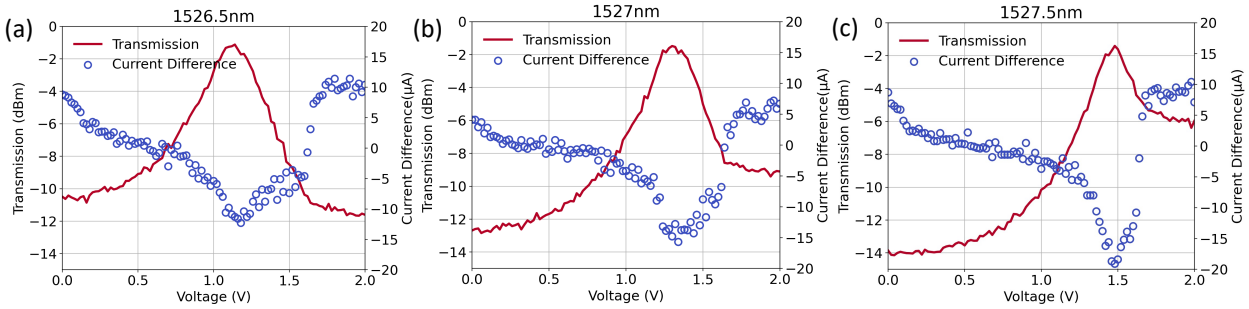


Figure 4.3: **Calibration of micro-ring modulator using photoconductive effect at different input laser wavelengths.** The laser input is (a) 1526.5nm (b) 1527nm and (c) 1527.5nm. The maximum current difference aligns well with the transmission peak.

For the effective functioning of optical neural networks, precise digitalized weight control with a high signal-to-noise ratio is essential. This section demonstrates the method for controlling the output intensity of a $TE_{01}$ micro-ring modulator. In Fig. 4.4(a), the output transmission is measured at different applied voltages, and the relation is fit by a fourth order polynomial as shown in the dashed grey line. For demonstration, a 3-bit control scheme was implemented, resulting in 8 discretized transmission outputs. We show in Fig. 4.4(b) that the corresponding mapping between transmission and applied voltage can be used for weight control. The error bars are obtained from five independent measurements. The observed error bar is much smaller than the transmission difference between the transmission levels, which indicates that the 3-bit control can be easily achieved with high signal to noise ratio. We would like to mention that more bits can be achieved and the current demonstration may be limited by the precision of the power supply used in experiment.

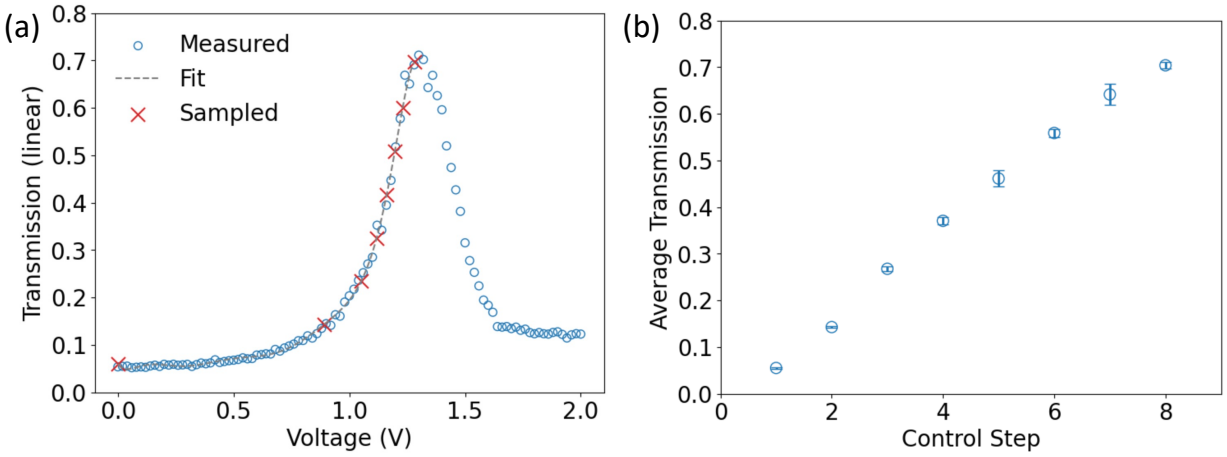


Figure 4.4: **3-bit control of the transmission with voltage applied to the micro-ring modulator.** (a) Transmission verse applied voltage. The data is fit with fourth order polynomial. (b) The digitized transmission is achieved with retrieved applied voltage. The error bar is from five independent measurements.

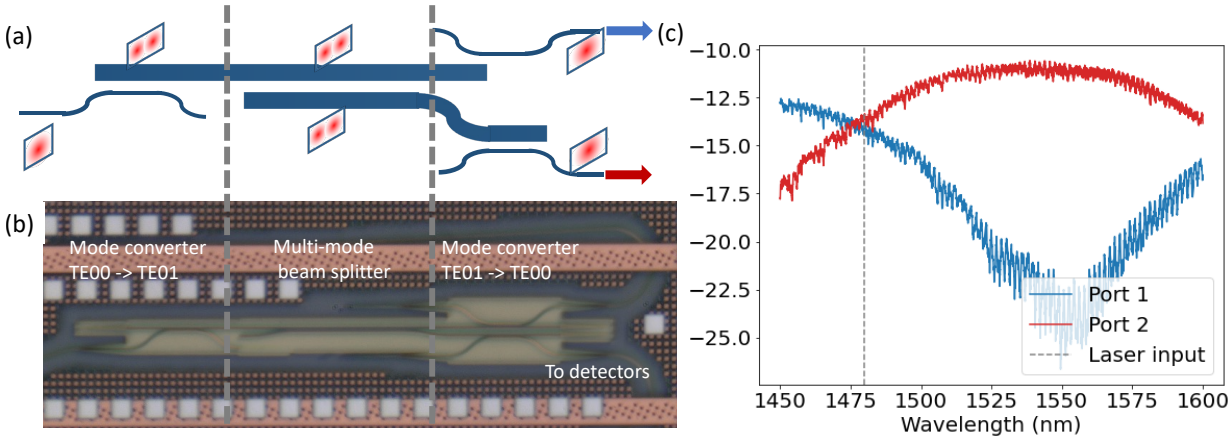


Figure 4.5: **Test device and measurement results for multi-mode beam splitter** (a) Schematics of the testing device for multi-mode directional coupler. (b) Microscope image of the fabricated testing device. (c) Measurement results.

## Multi-mode beam splitter based on directional coupler

A multi-mode beam splitter is crucial in the system to evenly distribute input power across various rows of the multiplication matrix, thus facilitating matrix multiplication. A simple way to implement such multi-mode splitter is based on the directional coupler as shown in

Fig. 4.5(a). The $TE_{00}$ mode is converted to $TE_{01}$ and split by the directional coupler, then converted back to $TE_{00}$ for detection. A microscope image is shown in Fig. 4.5(b). We use the same width of the multi-mode waveguide of 1.1 $um$ as the multi-mode microring modulator. The experimental results are shown in Fig. 4.5(c), which indicates that an equal output intensity at both ports appears near 1480nm.

## Multi-mode waveguide bend

Conventional bend in single-mode waveguide allows redirecting of light within a compact footprint. With a turning radius on the order of 10um, the scattering loss is less than 0.01dB. However, for a multi-mode waveguide, the cross-talk between modes can be significant. In Ref. [111], authors show the multi-mode interference pattern within a waveguide bend of 15$um$, and a radius greater than 200$um$ is needed to minimize unwanted crosstalk. The crosstalk, originates from the mismatch of mode profile between straight and bend region, can be reduced by using special shaped bend. The design adopts an Euler curve with gradually changing curvature to minimize cross-talk in multi-mode waveguide bends. The schematic is shown in Fig. 4.6. We use Euler curve with an ending radius of 20um, which bends the multimode waveguide off by 45 degrees after the multi-mode splitter. The total footprint is approximately 43um by 10um. The 3D FDTD simulation demonstrates an average transission of 96.5% for both $TE_{00}$ and $TE_{01}$ mode, across a broad wavelength range from 1450nm to 1650nm. In the optical multiplication system, two multi-mode waveguide bends are used in each arm after the multi-mode beam splitter to route for multiplication.

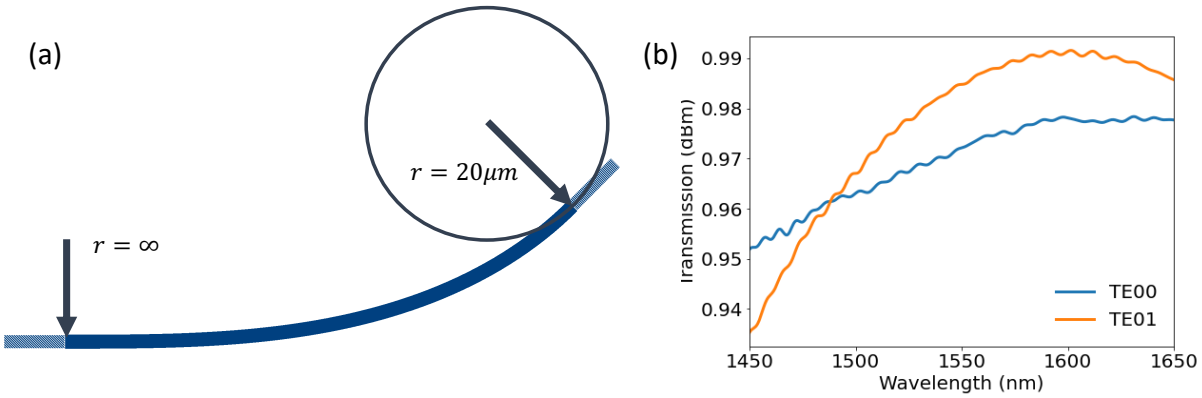


Figure 4.6: **Schematic and simulation of a multi-mode waveguide bend using Euler curve.** (a) Euler bend with ending radius of 20um. (b) 3D FDTD simulation results of $TE_{00}$-$TE_{00}$ and $TE_{01}$-$TE_{01}$ coupling.

## 4.4 System-level: simulation and experimental results

### System architecture

Fig. 4.7 presents a camera image of the fabricated chip, highlighting its various components including testing structures and the multimode matrix multiplication system. The chip consists of testing structures including multimode modulators, a directional coupler-based multimode beam splitter. The system with a multimode matrix multiplication system is on the bottom part, consisting of edge couplers from the left-hand side, and the electrical pad on the right-hand side. The chip is fabricated at AIM Photonics with MPW run [106].

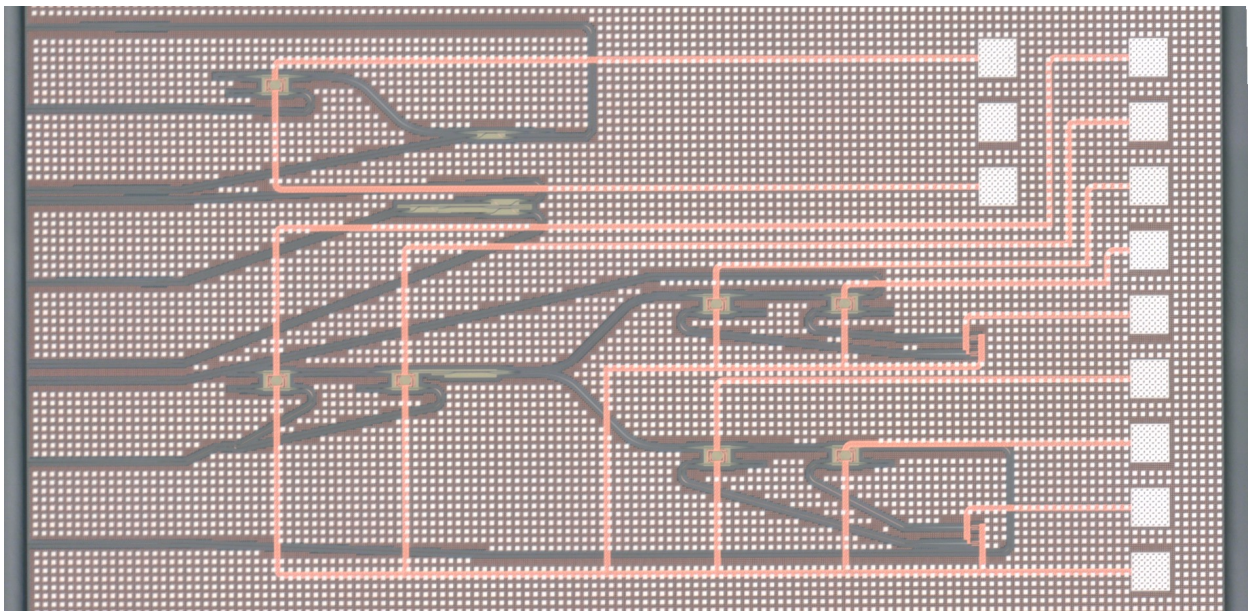

Figure 4.7: **Camera image of the system.**

This section demonstrates a 2x2 matrix multiplication using the mode-division multiplexing scheme, as illustrated in Fig. 4.8(a). The schematic figure of the fabricated layout is shown in Fig. 4.8(a). The laser input is coupled to the bus waveguide as $TE_{00}$ and $TE_{01}$ mode with input modulator $x_1$ and $x_2$, respectively. The bus waveguide is connected to the multi-mode beam splitter, and then to four micro-rings for a matrix multiplication operation. The micro-rings convert the target mode back into the fundamental mode and are measured by the photodetectors. We first show the results for element-wise multiplication (i.e. $a_{11}x_1, a_{12}x_2, a_{21}x_1, a_{22}x_2$). For simplicity, the input modulator is tuned to couple maximum intensity into the bus waveguide in each case. The current measured by the on-chip photo-detector is monitored while modulating the weight rings in the matrix. In Fig. 4.8(b), we demonstrate that the target modes can be coupled correctly into the photodetectors. Crosstalk between different modes is visualized in Fig. 4.8(c), where we estimate an average

signal-to-noise ratio of 5, based on the measurement results. Next, the multiplication and addition results are shown in Fig. 4.8(e-g) with different combinations of the input. For an input vector of $(0, 1)$ where only the $TE_{01}$ mode is coupled into the bus waveguide and distributed through the splitter, the current is determined by the applied voltage on the corresponding modulator $a_{12}$, which is designed to couple the $TE_{01}$. Similarly, the current response is dominated by the voltage applied on modulator $a_{11}$ with an input vector (1,0). For the (1,1) case, the current is summed up as expected, showing a correct multiplication-and-addition behavior.

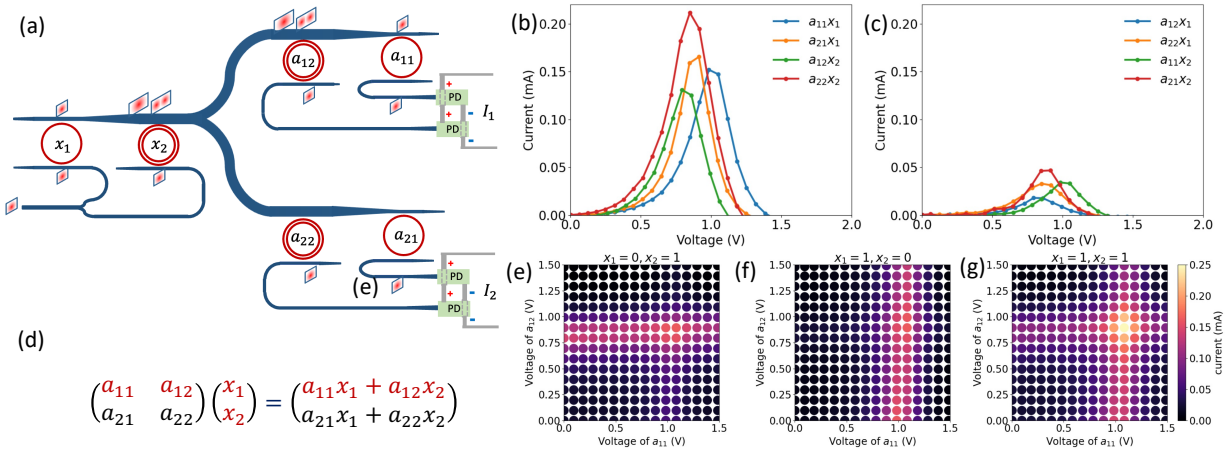


Figure 4.8: **Matrix multiplication with MDM micro-ring modulators.** (a) Schematic figure for the implemented 2 by 2 matrix multiplication with mode-division multiplexing. The fabricated structure consists of 6 micro-rings, two for input weights and four for matrix multiplication. Two photodetectors are connected in parallel for summing up the measured current for each row. (b) Measured photodetector currents for different combinations of input and weight micro-rings, showing the results for element-wise multiplication. (c) Measured cross-talk current for different combinations. (d) Matrix multiplication operation performed by the system. (e-g) Multiplication and addition results for different input combinations (1,0), (0,1), and (1,1).

Next, we show that the proposed MDM scheme is compatible with WDM. We combine two lasers and send them through the input channel. In Fig. 4.9, the output current is shown for different input combinations. When laser 1 is on and laser 2 is off, the fundamental mode at $\lambda_1$ is coupled, leading to the output current modulated by modulator $a_{11}$. If only laser 2 is switched on, the input laser of wavelength $\lambda_2$ is coupled to the second order mode of the bus waveguide and therefore modulated by the $a_{12}$. In Fig.4.9(d), we show that the output current at different wavelengths and modes can be summed up, resulting in the addition

of the current. These results confirm that MDM and WDM can be effectively combined, significantly increasing the number of channels available for matrix multiplication purposes.

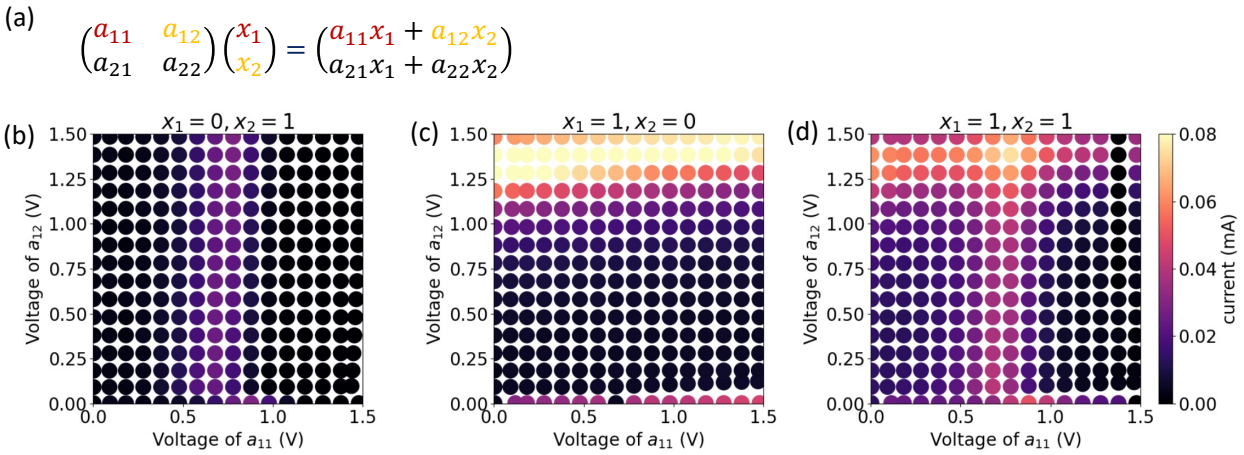


Figure 4.9: **Matrix multiplication with MDM-WDM scheme.** (a) Matrix multiplication operation performed with the system. (b) Multiplication and addition results for different input combinations (1,0), where only the laser 1 is on. (c) Multiplication and addition results with laser 2 on. (d) With both lasers on.

## 4.5 Conclusion

We propose and demonstrate a mode-division multiplexing optical matrix multiplication platform. We design and characterize the necessary components following the foundry fabrication constraints, including photoconductive micro-ring modulators for high-order modes, multi-mode beam splitter, and multi-mode waveguide bend, for a scalable WDM-compatible neural network. We experimentally characterize a matrix multiplication, and demonstrate the element-wise multiplication and row addition. The crosstalk between different modes is characterized and can be further optimized in future iterations. Such mode-division architecture can be used for small-size neural networks like convolutional neural networks for the prepossessing of graphs, which can reduce the complexity of multiple laser/frequency comb integration. For large-scale neural network applications, we also show that the proposed mode-division multiplexing is compatible with wavelength division multiplexing to increase the dimension of channels as well as the matrix. Conclusively, the proposed platform shows promise for developing compact, low-energy, and scalable computing systems, with potential for future optimization and application in large-scale neural networks.

# Chapter 5

# Future Directions

## Nonlinear applications with inverse-design

In practical quantum applications, direct generation of desired entangled high-order quantum state using inverse design can be very useful for quantum applications as proposed in Ref.[112], where the coupled wave equations are solved and the structure optimized for target quantum states at output. While Ref. [112] uses a quantum-optics picture, and optimizes a periodic structure by directly modeling vacuum fluctuation using a Gaussian white noise with variance, our work adopts a classical approach to optimize an aperiodic cavity using adjoint sources to avoid the sampling for vacuum fluctuations. Our inverse-design apporach enhances the generation rate using cavity resonances and reduces the computational cost by avoiding sampling the vacuum fluctuations numerically. An interesting future direction is to combine both works to produce target quantum state with cavity-enhanced generation rate on-chip.

The proposed inverse-design method can also be generalized for other nonlinear photon generation processes, such as on-chip parametric down-conversion, and third harmonic generation to name a few. The flexibility to choose target frequencies of the photon generation process opens opportunities for inverse-designed frequency conversion across different bands. The approach can be extended to multi-physics processes, for example, optimizing an opto-mechanical cavity for enhancing the coupling between optical waves and mechanical waves.

In addition, the perturbation theory shows that the 2D/3D Maxwell's equation can be approximated with 1D Schrodinger equation. The agreement between their solutions, i.e. field distributions and wave functions, indicates that the computational cost can be greatly reduced by replacing the simulation of Maxwell's equations with Schrodinger equations. This can provide a feasible roadmap for designing large-scale photonic crystal structures with an effective potential picture. It is also possible to apply inverse design to the Schrodinger equation to optimize for target effective potential, then replace the potential with the corresponding photonic crystal. This method can potentially greatly reduce the computational cost required for inverse design.

# Appendix A

# Supplementary materials

## A.1 Coupling light from fiber to chip

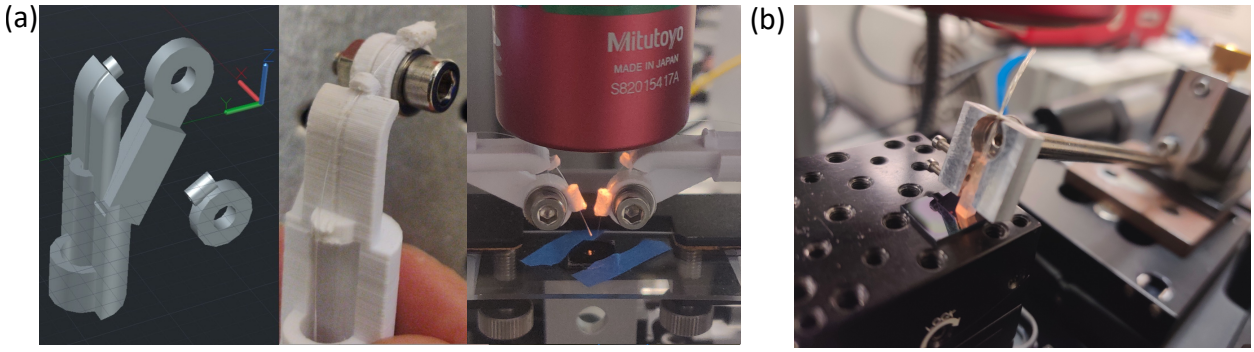


Figure A.1: **Home-made fiber and fiber array coupler.**

In the experiment, we tested different ways to couple light from the optical fiber to the chip. We started with a single fiber and customized the fiber holder with 3D printing as shown in Fig. A.1(a). Our 3D-printed fiber holder, comprising two interconnected parts with a screw connector, allows for precise tuning of the coupling angle, a key factor for optimal coupling efficiency. To allow multiple input/output channels, the fiber is replaced with a fiber array configuration, which is shown in Fig. A.1(b). In this configuration, the coupling angle is fixed but the installation is easier.

## A.2 Intuitive understanding of adjoint method

This section aims to elucidate the adjoint method through an intuitive approach, simplifying the understanding of its results. As shown in Eq. (3.3), the gradient is a multiplication of

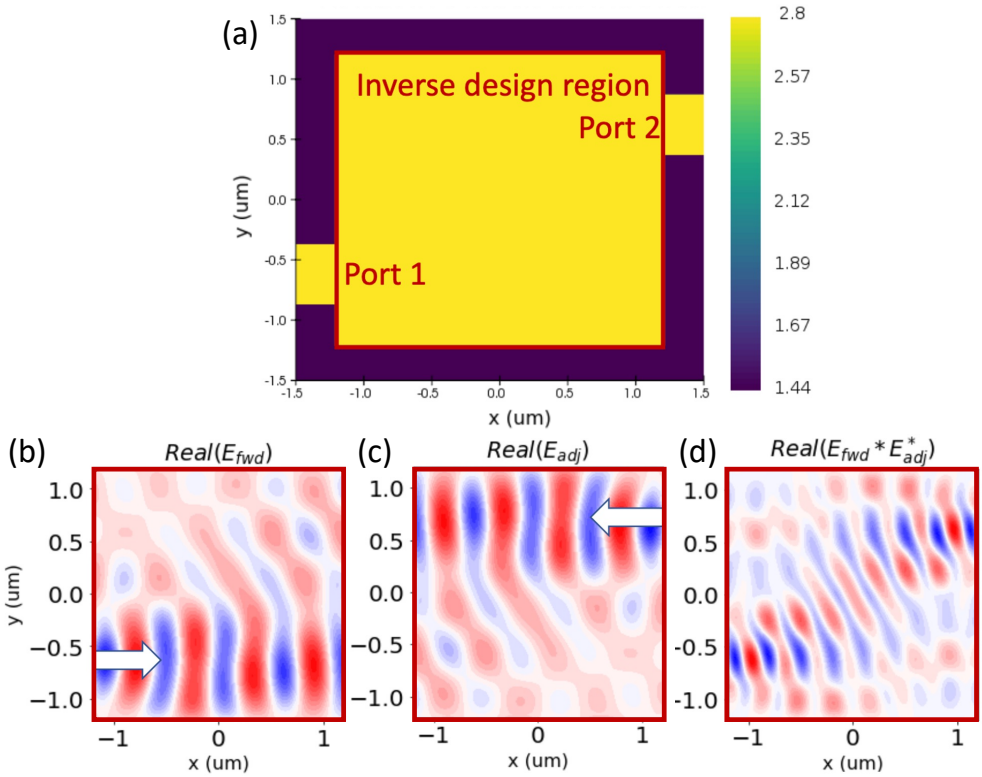


Figure A.2: **Intuitive illustration of adjoint method based on interference.** (a) An example of using inverse design for a waveguide from port 1 to port 2. (b) Field distribution in forward simulation. (c) Field distribution in adjoint simulation. (d) Interference pattern of forward and adjoint field used for gradients calculation.

fields of forward and adjoint simulations. The multiplication can be visualized with the following toy problem. We consider the naive case to design a waveguide from port 1 to port 2 using inverse design. In Fig. A.2(a), the design area is marked with a red box, and the colormap represents the refractive index distribution. The field distribution for forward and adjoint simulations are shown in Fig. A.2(b) and (c), respectively. In this example, the forward simulation corresponds to a guided source sent from port 1 and adjoint simulation is from port 2. In Fig. A.2, we can visualize the multiplication of the forward and adjoint fields, which forms the interference pattern as expected. The expression in Eq. (3.3) can be understood as the interference pattern multiplied with some shape gradients. In other words, the interference pattern provides a intuitive way to modify the permittivity distribution to optimize for the target function, naively reducing the permittivity in the blue region and increasing in the red region. In practice, this is the sensitivity analysis for the initial condition and typically the optimization needs many iterations with sensitivity analysis at

each iteration.

## A.3 Connection between adjoint method and back-propagation

There are a lot of similarities and connections between the adjoint method used in electromagnetic inverse design and back-propagation for training neural networks in machine learning.

1. **Sensitivity analysis in optimization:** Both approaches try to optimize a target function, which is called "figure of merit" in the adjoint method and "loss function" in machine learning by efficiently calculating gradients with respect to the input parameters.
2. **Chain rule:** Both methods use the chain rule in the calculation of the gradient.
3. **Forward and reverse propagation:** Both methods need to perform two runs of the system in forward and reverse directions to calculate the gradients.

In this section, we derive the expression for derivatives in a simple, two-layer neural network, which is then compared with the results of the adjoint method we have seen in the previous chapter. The goal is to develop a better understanding of the way that the two methods are related to one another.

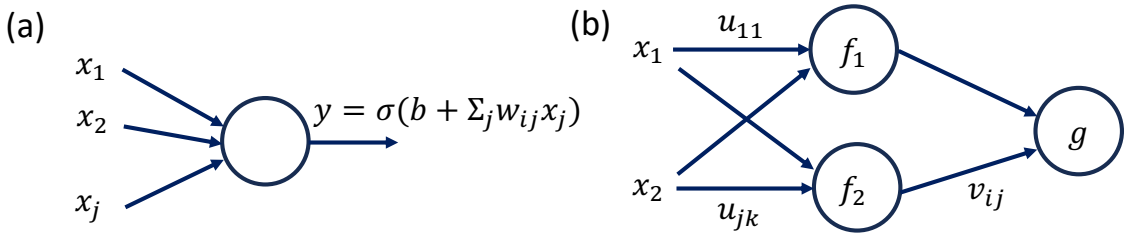


Figure A.3: **Schematics for a two-layer neural network.** (a) The function of a neuron. (b) A simple two-layer neural network.

A neural network consists of a unit called a neuron, or "perceptron", which is an operation that takes linear combinations of the input, and then applies a nonlinear activation function to the sum. The function of the neuron is illustrated in Fig. A.3(a), and is expressed as $y = \sigma(b + \sum_j w_{ij} x_j) = \sigma(\Sigma)$. Here, $x_j$ are the inputs, and $\sigma$ represents the nonlinear activation function. A neural network includes many layers of such neuron operation, and the output of the neurons in the previous layer becomes the input of the next layer. A two-layer neural network with two inputs is shown in Fig. A.3(b). The error function is defined

as the mismatch between the output of the network and the true value. For simplicity, we write the error $E = (g - g_0)^2$. By using the chain rule, we can represent the derivative of the error function with respect to the output of each neuron as:

$$\frac{\partial E}{\partial f_j} = \frac{\partial E}{\partial g}\sigma'(\Sigma)v_{ij} \tag{A.1}$$

The essence of training a neural network is to obtain the derivatives of the error function with respect to parameters ($u_{jk}, v_{ij}$ in this example). We can use the chain rule to find the target derivatives

$$\frac{\partial E}{\partial v_{ij}} = \frac{\partial E}{\partial g}\sigma'(\Sigma)f_j \tag{A.2}$$

$$\frac{\partial E}{\partial u_{jk}} = \frac{\partial E}{\partial f_j}\sigma'(\Sigma)x_k \tag{A.3}$$

In Eq. A.1, we first calculate the derivative of the error with respect to the neuron output. Based on the chain rule, the derivative for the first-layer neuron output $\frac{\partial E}{\partial f_j}$ can be represented in terms of the derivative for the final-layer neuron $\frac{\partial E}{\partial g}$. Therefore, this relation follows the name "back-propagation", where the derivatives are obtained from the final layer to the first layer in the backward direction. Next, the expression for parameters Eq. A.2 and A.3 can be used for derivatives calculation and training. Comparing these equations with the adjoint method (Eq. 3.3), we find that both involve three key components:

1. Forward result: $x, f_j$
2. Backward result: $y, \frac{\partial E}{\partial g}$
3. Local derivative: $\frac{\partial A}{\partial p_i}, \sigma'(\Sigma)$

The sensitivity to parameters (i.e. derivatives) is the product of the three terms. Therefore, we can conclude that not only are the essence of the two methods are same (chain rule), but the final expressions for the adjoint method and back-propagation share a lot of similarities.

# Bibliography


[1] W. Bogaerts et al. "Silicon microring resonators". In: *Laser and Photonics Reviews* 6.1 (2012), pp. 47–73. ISSN: 18638880. DOI: 10.1002/lpor.201100017.

[2] A. H. Clark. "Electrical and Optical Properties of Amorphous Germanium". In: *Physical Review* 154.3 (Feb. 1967), pp. 750–757. ISSN: 0031-899X. DOI: 10.1103/PhysRev.154.750.

[3] Denis Weaire. "Existence of a gap in the electronic density of states of a tetrahedrally bonded solid of arbitrary structure". In: *Physical Review Letters* 26.25 (June 1971), pp. 1541–1543. ISSN: 00319007. DOI: 10.1103/PhysRevLett.26.1541.

[4] D. J. Thouless et al. "Quantized Hall Conductance in a Two-Dimensional Periodic Potential". In: *Physical Review Letters* 49.6 (Aug. 1982), pp. 405–408. ISSN: 0031-9007. DOI: 10.1103/PhysRevLett.49.405.

[5] Lev B. Ioffe et al. "Topologically protected quantum bits using Josephson junction arrays". In: *Nature* 415.6871 (Jan. 2002), pp. 503–506. ISSN: 0028-0836. DOI: 10.1038/415503a.

[6] K. V. Klitzing, G. Dorda, and M. Pepper. "New Method for High-Accuracy Determination of the Fine-Structure Constant Based on Quantized Hall Resistance". In: *Physical Review Letters* 45.6 (Aug. 1980), pp. 494–497. ISSN: 0031-9007. DOI: 10.1103/PhysRevLett.45.494.

[7] Daniel Chee Tsui, Horst Ludwig Stormer, and Arthur Charles Gossard. "Two-Dimensional Magnetotransport in the Extreme Quantum Limit". In: *Physical Review Letters* 48.22 (May 1982), pp. 1559–1562. ISSN: 00319007. DOI: 10.1103/PhysRevLett.48.1559.

[8] Bodo Huckestein. "Scaling theory of the integer quantum Hall effect". In: *Reviews of Modern Physics* 67.2 (Apr. 1995), pp. 357–396. ISSN: 00346861. DOI: 10.1103/RevModPhys.67.357.

[9] Alejandro Cabo Montes de Oca and Danny Martinez-Pedrera. "Role of impurities in stabilizing quantum Hall effect plateaus". In: *Physical Review B* 67.24 (June 2003), p. 245310. ISSN: 0163-1829. DOI: 10.1103/PhysRevB.67.245310.

[10] Joel E. Moore. "The birth of topological insulators". In: *Nature* 464.7286 (Mar. 2010), pp. 194–198. ISSN: 0028-0836. DOI: 10.1038/nature08916.

[11] Qing Lin He et al. "Topological spintronics and magnetoelectronics". In: *Nature Materials* 21.1 (Jan. 2022), pp. 15–23. ISSN: 1476-1122. DOI: 10.1038/s41563-021-01138-5.

[12] Zheng Wang et al. "Reflection-Free One-Way Edge Modes in a Gyromagnetic Photonic Crystal". In: *Physical Review Letters* 100.1 (Jan. 2008), p. 013905. ISSN: 00319007. DOI: 10.1103/PhysRevLett.100.013905.

[13] Mohammad Hafezi et al. "Robust optical delay lines with topological protection". In: *Nature Physics* 7.11 (Nov. 2011), pp. 907–912. ISSN: 1745-2473. DOI: 10.1038/nphys2063.

[14] Sunil Mittal et al. "Topologically robust transport of photons in a synthetic gauge field". In: *Physical Review Letters* 113.8 (Aug. 2014), pp. 1–5. ISSN: 10797114. DOI: 10.1103/PhysRevLett.113.087403.

[15] Philippe St-Jean et al. "Lasing in topological edge states of a one-dimensional lattice". In: *Nature Photonics* 11.10 (Oct. 2017), pp. 651–656. ISSN: 1749-4885. DOI: 10.1038/s41566-017-0006-2.

[16] Babak Bahari et al. "Nonreciprocal lasing in topological cavities of arbitrary geometries". In: *Science* 358.6363 (Nov. 2017), pp. 636–640. ISSN: 0036-8075. DOI: 10.1126/science.aao4551.

[17] Babak Bahari et al. "Photonic quantum Hall effect and multiplexed light sources of large orbital angular momenta". In: *Nature Physics* 17.6 (Feb. 2021), pp. 700–703. ISSN: 17452481. DOI: 10.1038/s41567-021-01165-8.

[18] Han Zhao et al. "Non-Hermitian topological light steering". In: *Science* 365.6458 (Sept. 2019), pp. 1163–1166. ISSN: 0036-8075. DOI: 10.1126/science.aay1064.

[19] Daria Smirnova et al. "Nonlinear topological photonics". In: *Applied Physics Reviews* 7.2 (June 2020), p. 021306. ISSN: 1931-9401. DOI: 10.1063/1.5142397.

[20] Denis Weaire and Michael F. Thorpe. "Electronic properties of an amorphous solid. I. A simple tight-binding theory". In: *Physical Review B* 4.8 (Oct. 1971), pp. 2508–2520. ISSN: 01631829. DOI: 10.1103/PhysRevB.4.2508.

[21] Adhip Agarwala and Vijay B. Shenoy. "Topological Insulators in Amorphous Systems". In: *Physical Review Letters* 118.23 (June 2017), p. 236402. ISSN: 0031-9007. DOI: 10.1103/PhysRevLett.118.236402.

[22] Huaqing Huang and Feng Liu. "Quantum Spin Hall Effect and Spin Bott Index in a Quasicrystal Lattice". In: *Physical Review Letters* 121.12 (Sept. 2018), p. 126401. ISSN: 10797114. DOI: 10.1103/PhysRevLett.121.126401.

[23] Miguel A. Bandres, Mikael C. Rechtsman, and Mordechai Segev. "Topological photonic quasicrystals: Fractal topological spectrum and protected transport". In: *Physical Review X* 6.1 (Feb. 2016), pp. 1–12. ISSN: 21603308. DOI: 10.1103/PhysRevX.6.011016.

[24] Peiheng Zhou et al. "Photonic amorphous topological insulator". In: *Light: Science & Applications* 9.1 (Dec. 2020), p. 133. ISSN: 2047-7538. DOI: 10.1038/s41377-020-00368-7.

[25] Noah P. Mitchell et al. "Amorphous topological insulators constructed from random point sets". In: *Nature Physics* 14.4 (Apr. 2018), pp. 380–385. ISSN: 1745-2473. DOI: 10.1038/s41567-017-0024-5.

[26] Quentin Marsal, Dániel Varjas, and Adolfo G. Grushin. "Topological Weaire–Thorpe models of amorphous matter". In: *Proceedings of the National Academy of Sciences of the United States of America* 117.48 (Dec. 2020), pp. 30260–30265. ISSN: 10916490. DOI: 10.1073/pnas.2007384117.

[27] Alexei Kitaev. "Periodic table for topological insulators and superconductors". In: *AIP Conference Proceedings* 1134 (2009), pp. 22–30. ISSN: 0094243X. DOI: 10.1063/1.3149495.

[28] Alexei Kitaev. "Anyons in an exactly solved model and beyond". In: *Annals of Physics* 321.1 (Jan. 2006), pp. 2–111. ISSN: 00034916. DOI: 10.1016/j.aop.2005.10.005.

[29] Douglas R. Hofstadter. "Energy levels and wave functions of Bloch electrons in rational and irrational magnetic fields". In: *Physical Review B* 14.6 (Sept. 1976), pp. 2239–2249. ISSN: 0556-2805. DOI: 10.1103/PhysRevB.14.2239.

[30] Frederick Duncan Michael Haldane. "Model for a Quantum Hall Effect without Landau Levels: Condensed-Matter Realization of the "Parity Anomaly"". In: *Physical Review Letters* 61.18 (Oct. 1988), pp. 2015–2018. ISSN: 0031-9007. DOI: 10.1103/PhysRevLett.61.2015.

[31] N. F. Mott. "Electrons in disordered structures". In: *Advances in Physics* 16.61 (1967), pp. 49–144. ISSN: 14606976. DOI: 10.1080/00018736700101265.

[32] Sunil Mittal, Elizabeth A. Goldschmidt, and Mohammad Hafezi. "A topological source of quantum light". In: *Nature* 561.7724 (Sept. 2018), pp. 502–506. ISSN: 0028-0836. DOI: 10.1038/s41586-018-0478-3.

[33] Jun Rong Ong and Shayan Mookherjea. "Quantum light generation on a silicon chip using waveguides and resonators". In: *Optics Express* 21.4 (Feb. 2013), p. 5171. ISSN: 1094-4087. DOI: 10.1364/oe.21.005171.

[34] Sunil Mittal et al. "Tunable quantum interference using a topological source of indistinguishable photon pairs". In: *Nature Photonics* 15.7 (July 2021), pp. 542–548. ISSN: 1749-4885. DOI: 10.1038/s41566-021-00810-1.

[35] Ranjeet Kumar et al. "Controlling the spectrum of photons generated on a silicon nanophotonic chip". In: *Nature Communications* 5.1 (Dec. 2014), pp. 1–7. ISSN: 20411723. DOI: 10.1038/ncomms6489.

[36] M. Hafezi et al. "Imaging topological edge states in silicon photonics supplements". In: *Nature Photonics* 7.12 (2013), pp. 1001–1005. ISSN: 17494885. DOI: 10.1038/nphoton.2013.274.

[37] Hiroshi Fukuda et al. "Four-wave mixing in silicon wire waveguides". In: *Optics Express* 13.12 (2005), p. 4629. ISSN: 1094-4087. DOI: 10.1364/opex.13.004629.

[38] Stefano Signorini et al. "Intermodal four-wave mixing in silicon waveguides". In: *Photonics Research* 6.8 (2018), p. 805. ISSN: 2327-9125. DOI: 10.1364/prj.6.000805.

[39] Zin Lin et al. "High-efficiency degenerate four-wave mixing in triply resonant nanobeam cavities". In: *Physical Review A - Atomic, Molecular, and Optical Physics* 89.5 (2014), pp. 1–10. ISSN: 10941622. DOI: 10.1103/PhysRevA.89.053839.

[40] Kevin O'Brien et al. "Predicting nonlinear properties of metamaterials from the linear response". In: *Nature Materials* 14.4 (2015), pp. 379–383. ISSN: 14764660. DOI: 10.1038/nmat4214.

[41] Amy C. Turner et al. "Ultra-low power parametric frequency conversion in a silicon microring resonator". In: *Optics Express* 16.7 (2008), p. 4881. ISSN: 1094-4087. DOI: 10.1364/oe.16.004881.

[42] Stefano Azzini et al. "Ultra-low power generation of twin photons in a compact silicon ring resonator". In: *Optics Express* 20.21 (2012), p. 23100. ISSN: 10944087. DOI: 10.1364/oe.20.023100.

[43] Erman Engin et al. "Photon pair generation in a silicon micro-ring resonator with reverse bias enhancement". In: *Optics Express* 21.23 (2013), p. 27826. ISSN: 10944087. DOI: 10.1364/oe.21.027826.

[44] Davide Grassani et al. "Micrometer-scale integrated silicon source of time-energy entangled photons". In: *Optica* 2.2 (2015), p. 88. ISSN: 23342536. DOI: 10.1364/optica.2.000088.

[45] Stefan F. Preble et al. "On-chip quantum interference from a single silicon ring-resonator source". In: *Physical Review Applied* 4.2 (2015), pp. 1–5. ISSN: 23317019. DOI: 10.1103/PhysRevApplied.4.021001.

[46] Chaoxuan Ma et al. "Silicon photonic entangled photon-pair and heralded single photon generation with CAR ¿ 12,000 and g(2)(0) ¡ 0.006". In: *Optics Express* 25.26 (2017), p. 32995. ISSN: 10944087. DOI: 10.1364/oe.25.032995.

[47] Alexander W. Bruch et al. " On-chip $\chi$ (2) microring optical parametric oscillator ". In: *Optica* 6.10 (2019), p. 1361. ISSN: 23342536. DOI: 10.1364/optica.6.001361.

[48] Melissa A. Guidry et al. "Optical parametric oscillation in silicon carbide nanophotonics". In: *Optica* 7.9 (2020), p. 1139. ISSN: 2334-2536. DOI: 10.1364/optica.394138.

[49] Y. Zhang et al. "Squeezed light from a nanophotonic molecule". In: *Nature Communications* 12.1 (2021), pp. 8–13. ISSN: 20411723. DOI: 10.1038/s41467-021-22540-2.

[50] Anirudh Ramesh et al. "Photon-Pair Generation in a 45 nm CMOS Microring Cavity: Impact of Spontaneous Raman Scattering". In: *Optics InfoBase Conference Papers* c (2022), pp. 3–4. DOI: 10.1364/quantum.2022.qth2b.4.

[51] Jie Zhao et al. "High Quality Entangled Photon Pair Generation in Periodically Poled Thin-Film Lithium Niobate Waveguides". In: *Physical Review Letters* 124.16 (2020), p. 163603. ISSN: 10797114. DOI: 10.1103/PhysRevLett.124.163603.

[52] Juanjuan Lu et al. "Ultralow-threshold thin-film lithium niobate optical parametric oscillator". In: *Optica* 8.4 (2021), p. 539. ISSN: 23342536. DOI: 10.1364/optica.418984.

[53] Gabriel Marty et al. "Photonic crystal optical parametric oscillator". In: *Nature Photonics* 15.1 (2021), pp. 53–58. ISSN: 17494893. DOI: 10.1038/s41566-020-00737-z.

[54] P. I. Borel et al. "Topology optimization and fabrication of photonic crystal structures". In: *Optics Express* 12.9 (2004), p. 1996. ISSN: 10944087. DOI: 10.1364/opex.12.001996.

[55] Martin Burger, Stanley J. Osher, and Eli Yablonovitch. "Inverse Problem Techniques for the Design of Photonic Crystals". In: *IEICE Transactions on Electronics* E87-C.3 (2004), pp. 258–265. ISSN: 09168524.

[56] Stefan Preble, Michal Lipson, and Hod Lipson. "Two-dimensional photonic crystals designed by evolutionary algorithms". In: *Applied Physics Letters* 86.6 (2005), pp. 1–3. ISSN: 00036951. DOI: 10.1063/1.1862783.

[57] Sean Molesky et al. "Inverse design in nanophotonics". In: *Nature Photonics* 12.11 (2018), pp. 659–670. ISSN: 17494893. DOI: 10.1038/s41566-018-0246-9.

[58] Srivatsa Chakravarthi et al. "Inverse-designed photon extractors for optically addressable defect qubits". In: *Optica* 7.12 (2020), p. 1805. ISSN: 23342536. DOI: 10.1364/optica.408611.

[59] Raphaël Pestourie et al. "Efficient Inverse Design of Large-Area Metasurfaces for Incoherent Light". In: *ACS Photonics* (2022). ISSN: 23304022. DOI: 10.1021/acsphotonics.2c01015.

[60] Zhaoyi Li et al. "Empowering Metasurfaces with Inverse Design: Principles and Applications". In: *ACS Photonics* 9.7 (2022), pp. 2178–2192. ISSN: 23304022. DOI: 10.1021/acsphotonics.1c01850.

[61] Jiaqi Jiang, Mingkun Chen, and Jonathan A. Fan. "Deep neural networks for the evaluation and design of photonic devices". In: *Nature Reviews Materials* 6.8 (2021), pp. 679–700. ISSN: 20588437. DOI: 10.1038/s41578-020-00260-1.

[62] Zin Lin et al. "Cavity-enhanced second-harmonic generation via nonlinear-overlap optimization". In: *Optica* 3.3 (2016), p. 233. ISSN: 2334-2536. DOI: 10.1364/optica.3.000233.

[63] Tyler W. Hughes et al. "Adjoint Method and Inverse Design for Nonlinear Nanophotonic Devices". In: *ACS Photonics* 5.12 (2018), pp. 4781–4787. ISSN: 23304022. DOI: 10.1021/acsphotonics.8b01522.

[64] Erfan Khoram et al. "Nanophotonic media for artificial neural inference". In: *Photonics Research* 7.8 (2019), p. 823. ISSN: 2327-9125. DOI: 10.1364/prj.7.000823.

[65] Joshua Yang et al. "Inverse-designed Silicon Carbide Quantum and Nonlinear Photonics". In: *Light: Science & Applications* 12.1 (2023), pp. 1–7. ISSN: 20477538. DOI: 10.1038/s41377-023-01253-9.

[66] Zin Lin et al. "Enhanced Spontaneous Emission at Third-Order Dirac Exceptional Points in Inverse-Designed Photonic Crystals". In: *Physical Review Letters* 117.10 (2016), pp. 1–6. ISSN: 10797114. DOI: 10.1103/PhysRevLett.117.107402.

[67] Andrew Michaels and Eli Yablonovitch. "Leveraging continuous material averaging for inverse electromagnetic design". In: *Optics Express* 26.24 (2018), p. 31717. ISSN: 10944087. DOI: 10.1364/oe.26.031717.

[68] Jiaqi Jiang and Jonathan A. Fan. "Global Optimization of Dielectric Metasurfaces Using a Physics-Driven Neural Network". In: *Nano Letters* 19.8 (2019), pp. 5366–5372. ISSN: 15306992. DOI: 10.1021/acs.nanolett.9b01857.

[69] Sean Hooten, Raymond G. Beausoleil, and Thomas Van Vaerenbergh. "Inverse design of grating couplers using the policy gradient method from reinforcement learning". In: *Nanophotonics* 10.15 (2021), pp. 3843–3856. ISSN: 21928614. DOI: 10.1515/nanoph-2021-0332.

[70] James Bradbury et al. *JAX: composable transformations of Python+NumPy programs*. Version 0.3.13. 2018. URL: http://github.com/google/jax.

[71] Tyler W. Hughes et al. "Forward-Mode Differentiation of Maxwell's Equations". In: *ACS Photonics* 6.11 (2019), pp. 3010–3016. ISSN: 23304022. DOI: 10.1021/acsphotonics.9b01238.

[72] Robert W. Boyd. *Nonlinear Optics*. English. 3rd ed. Academic Press, 2008, p. 613. ISBN: 9780123694706.

[73] A. Agustí et al. "Tripartite Genuine Non-Gaussian Entanglement in Three-Mode Spontaneous Parametric Down-Conversion". In: *Physical Review Letters* 125.2 (2020), p. 20502. ISSN: 10797114. DOI: 10.1103/PhysRevLett.125.020502.

[74] Emanuel Istrate and Edward H. Sargent. "Photonic crystal heterostructures and interfaces". In: *Reviews of Modern Physics* 78.2 (2006), pp. 455–481. ISSN: 00346861. DOI: 10.1103/RevModPhys.78.455.

[75] Oskar Painter, Kartik Srinivasan, and Paul E. Barclay. "Wannier-like equation for the resonant cavity modes of locally perturbed photonic crystals". In: *Physical Review B - Condensed Matter and Materials Physics* 68.3 (2003), pp. 352141–3521413. ISSN: 10980121. DOI: 10.1103/PhysRevB.68.035214.

[76] Andrew Michaels, Ming C. Wu, and Eli Yablonovitch. "Hierarchical Design and Optimization of Silicon Photonics". In: *IEEE Journal of Selected Topics in Quantum Electronics* 26.2 (2020), pp. 1–12. ISSN: 21910359. DOI: 10.1109/JSTQE.2019.2935299.

[77] Ciyou Zhu et al. "Algorithm 778: L-BFGS-B: Fortran Subroutines for Large-Scale Bound-Constrained Optimization". In: *ACM Transactions on Mathematical Software* 23.4 (1997), pp. 550–560. ISSN: 00983500. DOI: 10.1145/279232.279236.

[78] Philip Y. Ma et al. "Photonic independent component analysis using an on-chip microring weight bank". In: *Optics Express* 28.2 (2020), p. 1827. ISSN: 10944087. DOI: 10.1364/oe.383603.

[79] Mathieu Charbonneau-Lefort et al. "Photonic crystal heterostructures: Waveguiding phenomena and methods of solution in an envelope function picture". In: *Physical Review B - Condensed Matter and Materials Physics* 65.12 (2002), pp. 1253181–1253187. ISSN: 01631829. DOI: 10.1103/PhysRevB.65.125318.

[80] Ole Sigmund. "Manufacturing tolerant topology optimization". In: *Acta Mechanica Sinica/Lixue Xuebao* 25.2 (2009), pp. 227–239. ISSN: 05677718. DOI: 10.1007/s10409-009-0240-z.

[81] Chaoran Huang et al. "A silicon photonic–electronic neural network for fibre nonlinearity compensation". In: *Nature Electronics* 4.11 (Nov. 2021), pp. 837–844. ISSN: 2520-1131. DOI: 10.1038/s41928-021-00661-2.

[82] Xingyuan Xu et al. "11 TOPS photonic convolutional accelerator for optical neural networks". In: *Nature* 589.7840 (2021), pp. 44–51. ISSN: 14764687. DOI: 10.1038/s41586-020-03063-0.

[83] J. Feldmann et al. "Parallel convolutional processing using an integrated photonic tensor core". In: *Nature* 589.7840 (2021), pp. 52–58. ISSN: 14764687. DOI: 10.1038/s41586-020-03070-1.

[84] Matthew van Niekerk et al. "Massively scalable wavelength diverse integrated photonic linear neuron". In: *Neuromorphic Computing and Engineering* 2.3 (2022), p. 034012. DOI: 10.1088/2634-4386/ac8ecc.

[85] Logan G. Wright et al. "Deep physical neural networks trained with backpropagation". In: *Nature* 601.7894 (2022), pp. 549–555. ISSN: 14764687. DOI: 10.1038/s41586-021-04223-6.

[86] Hailong Zhou et al. "Photonic matrix multiplication lights up photonic accelerator and beyond". In: *Light: Science and Applications* 11.1 (2022). ISSN: 20477538. DOI: 10.1038/s41377-022-00717-8.

[87] Sunil Pai et al. "Experimentally realized in situ backpropagation for deep learning in photonic neural networks". In: *Science (New York, N.Y.)* 380.6643 (2023), pp. 398–404. ISSN: 10959203. DOI: 10.1126/science.ade8450.

[88] Anthony Rizzo et al. "Massively scalable Kerr comb-driven silicon photonic link". In: *Nature Photonics* (2023). ISSN: 1749-4885. DOI: 10.1038/s41566-023-01244-7.

[89] Shaofu Xu et al. "High-order tensor flow processing using integrated photonic circuits". In: *Nature Communications* 13.1 (2022). ISSN: 20411723. DOI: 10.1038/s41467-022-35723-2.

[90] Matthew J. Filipovich et al. "Silicon photonic architecture for training deep neural networks with direct feedback alignment". In: *Optica* 9.12 (2022), p. 1323. ISSN: 23342536. DOI: 10.1364/optica.475493.

[91] Tianyu Wang et al. "An optical neural network using less than 1 photon per multiplication". In: *Nature Communications* 13.1 (Dec. 2022). ISSN: 20411723. DOI: 10.1038/s41467-021-27774-8.

[92] Enxiao Luan et al. "Towards a high-density photonic tensor core enabled by intensity-modulated microrings and photonic wire bonding". In: *Scientific Reports* 13.1 (2023), pp. 1–17. ISSN: 20452322. DOI: 10.1038/s41598-023-27724-y.

[93] Tianyu Wang et al. "Image sensing with multilayer nonlinear optical neural networks". In: *Nature Photonics* 17.5 (May 2023), pp. 408–415. ISSN: 17494893. DOI: 10.1038/s41566-023-01170-8.

[94] Yichen Shen et al. "Deep learning with coherent nanophotonic circuits". In: *Nature Photonics* 11.7 (2017), pp. 441–446. ISSN: 17494893. DOI: 10.1038/nphoton.2017.93.

[95] Alexander N. Tait et al. "Neuromorphic photonic networks using silicon photonic weight banks". In: *Scientific Reports* 7.1 (2017), pp. 1–10. ISSN: 20452322. DOI: 10.1038/s41598-017-07754-z.

[96] Alexander N. Tait. "Quantifying Power in Silicon Photonic Neural Networks". In: *Physical Review Applied* 17.5 (2022), p. 1. ISSN: 23317019. DOI: 10.1103/PhysRevApplied.17.054029.

[97] Alexander L. Gaeta, Michal Lipson, and Tobias J. Kippenberg. "Photonic-chip-based frequency combs". In: *Nature Photonics* 13.3 (2019), pp. 158–169. ISSN: 17494893. DOI: 10.1038/s41566-019-0358-x.

[98] Lin Chang, Songtao Liu, and John E. Bowers. "Integrated optical frequency comb technologies". In: *Nature Photonics* 16.2 (2022), pp. 95–108. ISSN: 17494893. DOI: 10.1038/s41566-021-00945-1.

[99] Haowen Shu et al. "Microcomb-driven silicon photonic systems". In: *Nature* 605.7910 (2022), pp. 457–463. ISSN: 14764687. DOI: 10.1038/s41586-022-04579-3.

[100] Bowen Bai et al. "Microcomb-based integrated photonic processing unit". In: *Nature Communications* 14.1 (2023). ISSN: 20411723. DOI: 10.1038/s41467-022-35506-9.

[101] Kishore Padmaraju et al. "Intermodulation crosstalk characteristics of WDM silicon microring modulators". In: *IEEE Photonics Technology Letters* 26.14 (2014), pp. 1478–1481. ISSN: 10411135. DOI: 10.1109/LPT.2014.2326621.

[102] Li Deng. "The MNIST database of handwritten digit images for machine learning research". In: *IEEE Signal Processing Magazine* 29.6 (2012), pp. 141–142. ISSN: 10535888. DOI: 10.1109/MSP.2012.2211477.

[103] Lian Wee Luo et al. "WDM-compatible mode-division multiplexing on a silicon chip". In: *Nature Communications* 5 (2014), pp. 1–7. ISSN: 20411723. DOI: 10.1038/ncomms4069.

[104] Xinru Wu et al. "Mode-Division Multiplexing for Silicon Photonic Network-on-Chip". In: *Journal of Lightwave Technology* 35.15 (2017), pp. 3223–3228. ISSN: 07338724. DOI: 10.1109/JLT.2017.2677085.

[105] Ki Youl Yang et al. "Multi-dimensional data transmission using inverse-designed silicon photonics and microcombs". In: *Nature Communications* 13.1 (2022), pp. 1–9. ISSN: 20411723. DOI: 10.1038/s41467-022-35446-4.

[106] Nicholas M. Fahrenkopf et al. "The AIM Photonics MPW: A Highly Accessible Cutting Edge Technology for Rapid Prototyping of Photonic Integrated Circuits". In: *IEEE Journal of Selected Topics in Quantum Electronics* 25.5 (2019), pp. 1–6. ISSN: 21910359. DOI: 10.1109/JSTQE.2019.2935698.

[107] Hasitha Jayatilleka et al. "Wavelength tuning and stabilization of microring-based filters using silicon in-resonator photoconductive heaters". In: *Optics Express* 23.19 (2015), p. 25084. ISSN: 10944087. DOI: 10.1364/oe.23.025084.

[108] Alexander N Tait. "Silicon Photonic Neural Networks". In: *Diss. Princeton University* April (2018).

[109] Chaoran Huang et al. "Demonstration of scalable microring weight bank control for large-scale photonic integrated circuits". In: *APL Photonics* 5.4 (2020). ISSN: 23780967. DOI: 10.1063/1.5144121.

[110] Chaoran Huang et al. "On-Chip Programmable Nonlinear Optical Signal Processor and Its Applications". In: *IEEE Journal of Selected Topics in Quantum Electronics* 27.2 (2021). ISSN: 15584542. DOI: 10.1109/JSTQE.2020.2998073.

[111] Hongnan Xu, Daoxin Dai, and Yaocheng Shi. "Silicon Integrated Nanophotonic Devices for On-Chip Multi-Mode Interconnects". In: *Applied Sciences* 10.18 (Sept. 2020), p. 6365. ISSN: 2076-3417. DOI: 10.3390/app10186365.

[112] Eyal Rozenberg et al. "Inverse design of spontaneous parametric downconversion for generation of high-dimensional qudits". In: *Optica* 9.6 (2022), p. 602. ISSN: 23342536. DOI: 10.1364/optica.451115.